BILINGUAL PUBLISHING CO.
Pioneer of Global Academics Since 1984

01
2021

Journal of Geological Research

Volume 3 | Issue 1 | January 2021 | ISSN 2630-4961 (Online)

ISSN 2630-4961 01
9 772630 496218

BILINGUAL PUBLISHING CO.
Pioneer of Global Academics Since 1984

Editor-in-Chief

Editorial Board Members

Volume 3 Issue 1 • January 2021 • ISSN 2630-4961 (Online)

Journal of Geological Research

BILINGUAL PUBLISHING CO.
Pioneer of Global Academics Since 1984

BILINGUAL PUBLISHING CO.
Pioneer of Global Academics Since 1984

Volume 3 | Issue 1 | January 2021 | Page 1-49
Journal of Geological Research

Contents

ARTICLE

1 **Factor Analysis of the Parameters of Samples of the Steppe Soil and Grass Of Mongolia and Inland Mongolia of China on the Eastern Transsect of the Eurasian Steppe**
Peter M. Mazurkin

11 **Hydrocarbon Play Assessment of "Oswil" Field, Onshore Niger Delta Region**
Osisanya, W.O. Alile, O.M. Eze, S.U. Ibitoye, T.A. Oyanameh, O.E.

22 **Geostatistical Modelling of Reservoir Quality Over "Bright" Field, Niger Delta**
Abe, S.J Olowokere, M. T Enikanselu, P. A

30 **Petrographic Study of Sedimentary Iron Ore in Shendi-Atbara Basin, River Nile State, Sudan**
Abubaker A.M.A. Abasher Sadam H.M.A.Eltayib El Sheikh M. Abdelrahman Mohammed M.A.Amlas

39 **Characterization of the Sulfide Deposits in the Southeastern Nigeria Using VLF Method: Insights from Numerical Modeling and Field Examples**
D. E. Falebita O. Afolabi B. O Soyinka A. A. Adepelumi

BILINGUAL PUBLISHING CO.
Pioneer of Global Academics Since 1984

Journal of Geological Research
https://ojs.bilpublishing.com/index.php/jgr-a

ARTICLE

Factor Analysis of the Parameters of Samples of the Steppe Soil and Grass Of Mongolia and Inland Mongolia of China on the Eastern Transsect of the Eurasian Steppe

Peter M. Mazurkin*

Volga State University of Technology, Yoshkar-Ola, Russia

ARTICLE INFO

Article history
Received: 3 November 2020
Accepted: 30 November 2020
Published Online: 31 January 2021

Keywords:
Mongolia
Steppes
Soil
Grass
Parameters
Relationships
Patterns

ABSTRACT

Regularities of rank distributions and binary relations between nine parameters are given. The most active are the geographical coordinates of 48 test sites. This proves that the geomorphology of the steppes in Mongolia and Inner Mongolia is becoming decisive. Factor analysis showed that the first four places for influencing variables and dependent indicators are the same: in the first place is the northern latitude, the second is the east longitude, the third is the average annual precipitation, and the fourth is the intensity of sheep grazing. The rest of the factors are located in different ways. The density of organic carbon was only in ninth place as an influencing variable, and in seventh place as a dependent indicator. This is based on the fact that organic carbon is an accumulative (cumulative) parameter over many years. The productivity of the biomass of steppe grass as an influencing variable is in sixth place, and as a dependent indicator (criterion) only in ninth place. This parameter is seasonal, therefore, in comparison with organic carbon, it is highly dynamic. The average annual temperature as an influencing variable is in fifth place, but as a dependent indicator only in eighth place. This was influenced by the strong averaging of the parameter (average value for the year). Plants are strongly influenced by the temperature dynamics during the growing season, and even more by the sum of temperatures during the growing season. With the productivity of steppe grass less than 75 g / m^2, the intensity of sheep grazing is zero. According to the second term of the trend, an optimum of 270 g / m^2 appears with the maximum intensity of sheep grazing on average 65 pcs / km^2. The first fluctuation shows that with an increase in grass biomass, there is a loss of stability of the grass cover with an exponential growth of the amplitude. The second oscillation is dangerous in that with an increase in the biomass of the grass, the half-period of the oscillation sharply decreases and this will also lead to the collapse of the steppe grass. From the remnants of the effect of sheep grazing on grass biomass, it can be seen that there are three clusters: (1) from 0 to 30; (2) from 30 to 95; (3) more than 95 pcs / km^2. In this case, the variability of the productivity of the grass decreases.

**Corresponding Author:*
Peter M. Mazurkin,
Volga State University of Technology, Yoshkar-Ola, Russia;
SPIN-code: 4476-9548; Researcher ID: H-7464-2014; ORCID ID: 0000-0003-0177-5521;
Email: kaf_po@mail.ru

 DOI: https://doi.org/10.30564/jgr.v3i1.2520

1. Introduction

At the subregional level, in addition to temperature and precipitation, soil texture plays an important role in soil organic carbon storage. For example, the content of soil clay has a significant positive effect on the accumulation of organic carbon in the soil, and the accumulation of organic carbon in the soil increases with an increase in the pH of the soil. Carbon input is associated with plant productivity, while carbon output mainly depends on the decomposition of microbial organic matter. With an increase in the intensity of sheep grazing, a number of different effects were found [7].

The Mongolian Highlands steppe is located in the eastern part of the Eurasian steppe, which is the largest pasture in the world, stretching more than 8000 km from northeastern China, through Inner Mongolia, Mongolia, Russia and Ukraine, to Hungary. The Mongolian plateau is a region sensitive to climate change.

Purpose of the Study

According to [7] for the steppes of Mongolia and Inner Mongolia of China, to reveal the hierarchy among 48 test plots with rank distributions of nine bioclimatic parameters, after using the factor analysis method [1,5,6] to reveal the regularities of their paired comparisons, and then to reveal the hierarchy between these nine factors.

2. Materials and Methods

Table 1 shows a fragment of the initial data [7].

Table 1 shows the following conventions: β:=β-111, reduced east longitude, ^{0}; α:=α-42, normalized north latitude, ^{0}; P - average annual precipitation, mm; t - average annual temperature, ^{0}C; C - clay content in soil, %; pH - pH value (at less than 7 acidity); G - the intensity of grazing livestock (sheep), units / km^2; B - productivity of biomass of grass cover, g / m^2; S_o - density of organic carbon in soil at a depth of 0-30 cm, kg / m^2.

Oscillations (wavelet signals) are written by the wave formula [1,5,6] of the form

$$y_i = A_i \cos(\pi x / p_i - a_{8i}), A_i = a_{1i} x^{a_{2i}} \exp(-a_{3i} x^{a_{4i}}), p_i = a_{5i} + a_{6i} x^{a_{7i}} \quad (1)$$

Where y - is the indicator (dependent factor), i - is the number of the member of the model (1), m - is the number of members in the model (1), reaching 200 and more, x - is the explanatory variable (influencing factor), $a_1 ... a_8$ - are the parameters of the model (1), taking numerical values in in the course of structural and parametric identification in the CurveExpert-1.40 software environment (URL: http://www.curveexpert.net/), A_i - the wavelet amplitude (half) (axis y), p_i - oscillation half-period (axis x).

In the particular case when $a_{2i=1} = 0$ for the first oscillation, and $a_{5i=1,2} = \infty$ for both waves, model (1) is transformed into a two-term formula of the form

$$y = a \exp\left(-bx^c\right) + dx^e \exp\left(fx^g\right) \quad (2)$$

where y - is an indicator, x - is a variable, a-g - are parameters (2). The first term is a modified law of exponential death, and the second is a biotechnical law [5,6].

3. Object Hierarchy

When synthesizing hierarchies, we adhere to ***Barry Commoner's law*** "Everything is connected with everything" [4], that is, any factor in some quantitative measure (correlation) affects the change in the values of other quantitatively expressed factors.

Hierarchy is a kind of abstraction of the structure of the system, designed to study the functional interactions of its components and their effects on the system as a whole [3, p.12]. The method of analyzing hierarchies is widespread in the world.

In our case, the system (48 sample plots of soil and grass of the steppe) is known, and nine quantitative parameters have been determined for it. Next, the problem arises of synthesizing the hierarchy in the system as of a certain moment in time.

For a known system, the synthesis of the hierarchy is possible in two ways:

(1) first, the ordering of the values of the parameters by the pre-order vector of preference "better $\rightarrow$ worse" by ranks $R = 0,1,2,...$, then the sum of the ranks of the entire

Table 1. Parameters of soil and grass in Mongolia and Inner Mongolia [7]

№	β, ^{0}	α, ^{0}	P, мм	t, ^{0}C	C, %	pH	G, шт./км^2	B, г/м^2	S_o, **кг/м^2**
1	4.94	0	382	2.0	9	7.69	58.30	194.62	55.61
2	5.33	0.05	384	1.7	11	7.53	126.13	361.48	30.22
3	5.74	0.18	404	2.0	49	7.57	127.28	293.24	22.28
…	…	…	…	…	…	…	…	…	…
46	3.19	5.65	153	0.5	64	7.06	4.65	325.42	70.98
47	1.74	5.87	224	0.8	55	6.31	9.25	321.11	51.73
48	2.46	6.08	172	1.1	55	6.35	8.99	138.07	57.29

DOI: https://doi.org/10.30564/jgr.v3i1.2520

list of system parameters; this is how a rating is formed, and the best will be the element with the lowest sum of ranks;

(2) by the method of analysis of hierarchies by T. Saaty [3], a pairwise comparison of all parameters of the system is performed, the identification method reveals the patterns of binary relations, then the correlation coefficients are summed up by rows and columns, then the ratings of the parameters as influencing variables and dependent indicators are identified.

Next, we will consider the first method, which is possible without the use of mathematics. Then we will reveal the regularities of rank distributions. According to the second method, the correlation coefficients of rank distributions are located in the correlation matrix along diagonal cells, which show the quality factor of the system under study for each parameter.

4. Environmental Ranking of Parameters

Each biological object strives for the best in life, therefore, only two variants of vector orientations in behavior are possible [1]: (1) less is better (but better); (2) more is better (and this is a blessing).

Table 2 shows the vector ecological reference points of the parameters from Table 1. Then, after establishing one direction of all the factors taken into account, it will be possible to add the ranks of all parameters.

Table 2. Directionality of parameters (Table 1)

Factor name	Less is better	Bigger is better
Eastern longitude	+	-
Northern latitude	+	-
Average annual precipitation	-	+
Average annual temperature	-	+
Clay, soil content	+	-
Hydrogen exponent pH	+	-
Sheep grazing intensity	+	-
Grass productivity	-	+
Density of organic carbon	-	+

The farther west and south the coordinates of the test site, the better because of the improved climate. And the more precipitation and temperature, the better the growing conditions for steppe grass.

When ranking in the function=RANK (E3;E$3:E$51;0), the following conventions are adopted for the Excel software environment: E - identifier of the ranked column; E3, E$3 - first line; E$51 - last line; $0 \vee 1$ - ranking in descending (0) or ascending (1) values of the ranged parameter.

Table 3 shows the ranking results. By the smallest sum of ranks, the first place was taken by trial site No. 1.

Table 3. Distribution of site parameters for soil and grass samples by ranks

№	R_β	R_α	R_P	R_t	R_C	R_{pH}	R_G	R_B	R_S	$\sum R$	$I_{\sum R}$
1	33	0	2	2	1	25	30	29	14	136	**1**
2	42	1	1	5	8	18	46	2	40	163	6
3	46	2	0	2	37	20	47	10	47	211	23
…	…	…	…	…	…	…	…	…	…	…	…
46	13	45	47	35	44	8	3	6	4	205	18
47	4	46	34	31	41	3	10	7	19	195	10
48	9	47	45	24	41	4	9	39	13	231	41

5. Rank Distribution Patterns

In Table 4 they are arranged (Figure 1) in descending order of the correlation coefficient. It is above the level of

Table 4. Model parameters (2) of rank distributions of soil and grass factors

Vari-able x	Indi-cator y	Trend							Coef. correl. r
		Exponential law			Biotechnical law				
		a	b	c	d	e	f	g	
R_S	S_O	78.7531e8	0.021593	1.02765	-7.11026e-21	12.37493	0	0	0.9982
R_β	β	0.96930	-0.029401	1.04792	0.13092	1.00517	5.76472e-5	2.74255	0.9979
R_α	α	0	0	0	0.073290	1.28536	0.076566	0.51008	0.9978
R_B	B	386.41938	0.0022480	1	-15.00781	0.72468	0	0	0.9964
R_{pH}	pH	5.97998	-6.28704e-5	2.17951	0.11128	1.53014	0.18525	0.81105	0.9963
R_t	t	2.12918	0.041140	0.88802	-2.54973e-12	7.06557	0	0	0.9951
R_G	G	4.74685	-0.0017373	1.95353	2.14050e-6	7.28157	0.32679	0.94126	0.9951
R_C	C	5.52602	-0.33172	0.52594	-1.15934e-75	67.41401	0.22852	1.61426	0.9944
R_P	P	406.47120	0.00030870	1	-15.32082	0.70063	0	0	0.9882
$I_{\sum R}$	$\sum R$	136.32243	-0.012847	1	1.61732	1.67501	0.043098	1.28411	0.9934

 DOI: https://doi.org/10.30564/jgr.v3i1.2520

adequacy 0.95 “super strong connection”.

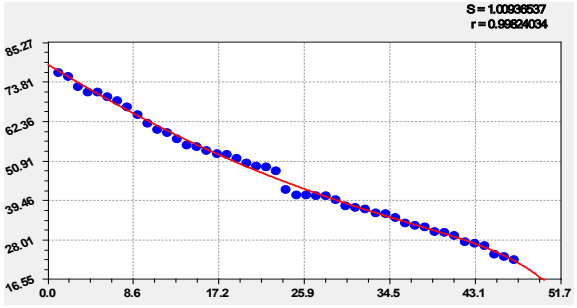

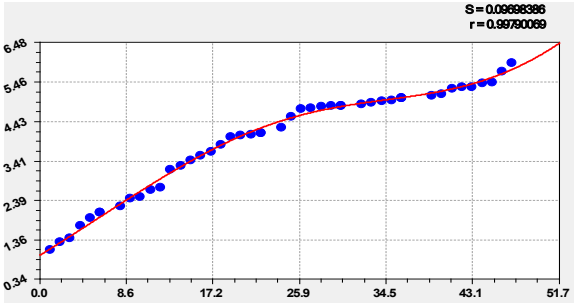

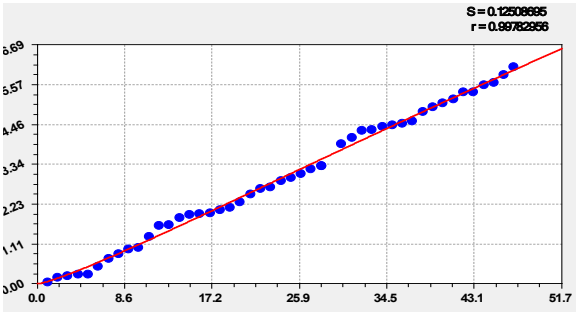

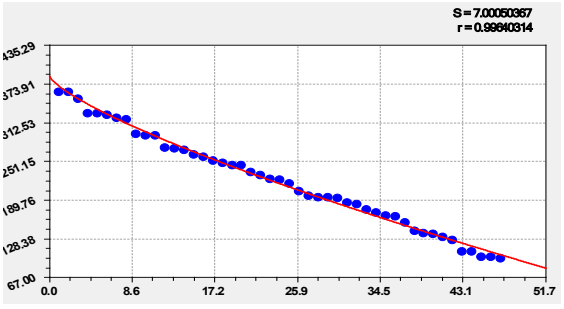

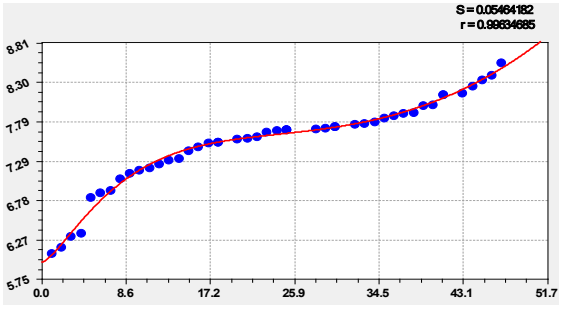

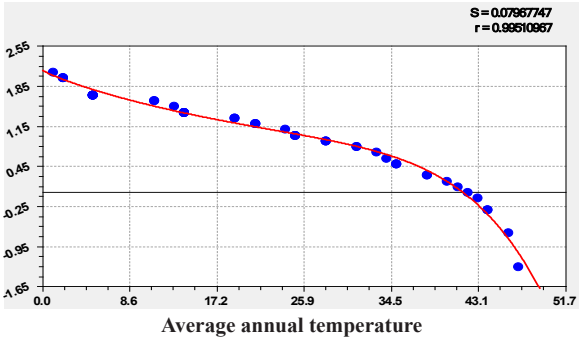

Figure 1. Graphs of rank distributions of parameters of soil and grass samples

Note: In the upper right corner: S - standard deviation; r - correlation coefficient)

All rank distributions have additional asymmetric wavelets (1). This fact shows the difference between bioclimatic parameters (areas for three points of soil and grass of the steppe) from meteorological parameters [5,6], between which there is a high uncertainty of quantization for asymmetric wavelet signals.

As an example, we will show two fluctuations (1) of northern latitude by ranks (Figure 2).

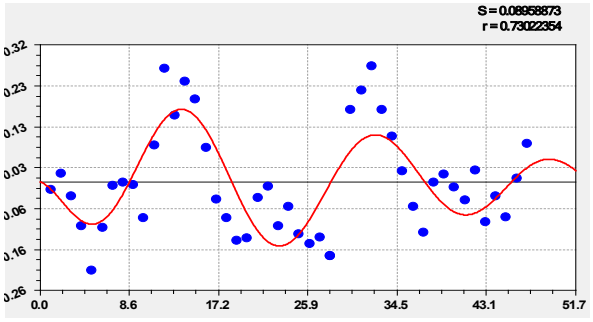

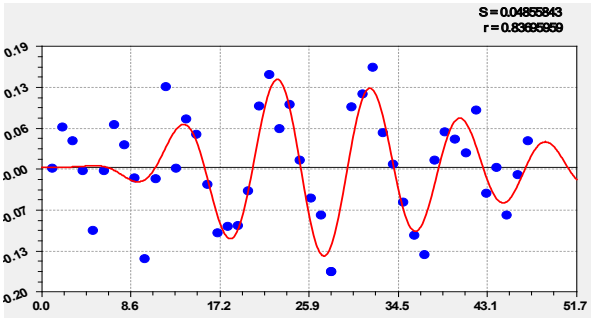

Figure 2. Graphs of oscillatory adaptation of the latitude of the test sites

Then it turns out that the steppe grass for almost 450 million years of its evolution "learned" to oscillate adapt to the terrain and the changing climate, spreading over the land according to wave laws. In the forest-meadow phyto-

DOI: https://doi.org/10.30564/jgr.v3i1.2520

cenosis, the grass is much stronger in comparison with the productivity of trees [2]. Therefore, steppe grass even indirectly affects the change in the geographical parameters of its place of growth.

6. Hierarchy of Factors by Correlation Matrix

Table 5 shows the results of a full factorial analysis of nine adopted parameters for a system of 48 sample plots of soil and grass samples from Mongolia and Inner Mongolia of China.

The first four places for influencing variables and dependent indicators are the same. In the first place is the northern latitude, the second is the eastern longitude, the third is the average annual precipitation, and the fourth is the intensity of sheep grazing. The rest of the factors are located in different ways. For example, the average annual temperature as an influencing variable is in fifth place, and as a dependent indicator in eighth place.

The geodetic coordinates of the test plots are the most significant. Then the disadvantage of the experiments carried out is the lack of measurements of the height above the level of the Baltic Sea. In Mongolia, even a small difference in height above the sea can be decisive.

The coefficient of correlative variation of the properties of a physical object of research in the form of 48 test sites and 9 factors is equal to the ratio of the total sum of the correlation coefficients to the square of the number of factors. According to Table 5, the coefficient of correlative variation will be $43.6648 / 9^2 = 0.5391$. It evaluates the functional connectivity of the system elements. This criterion allows you to compare dissimilar systems with each other.

7. Strong Factor Relationships

From table 5, we exclude diagonal cells and those cells in which the correlation coefficient is less than 0.7 (the level of adequacy "strong connection").

Table 6. Strong relationships $r \geq 0.7$

x	Indicators			
	β	α	P	G
β		0.8829	0.8891	0.8040
α	0.8992		0.9382	0.8347
P	0.7661	0.9109		0.7997
t		0.7348		
C	0.7260			
pH		0.7919		
G	0.8542	0.8958	0.8656	

Among the strong binary relations, four indicators and seven influencing variables remained (parameters, and were added to the main variables pH, t and C). A total of 15 strong pairs formed.

Table 7 shows the parameters of strong trends (Figure 3), containing two terms, and which are arranged in descending order of the values of the correlation coefficient.

In the future, they should be compared with each other weak (the level of adequacy from 0.3 to 0.5 according to the correlation coefficient), medium (from 0.5 to 0.7) and strong (more than 0.7) factorial relationship. Moreover, the analysis of weak ties can lead to the emergence of productive ideas and scientific and technical solutions.

Table 5. Correlation matrix by trends (2) and rating assessment of factors

x	Dependent factors (indicators)									Amount Σr	A place
	β	α	P	t	C	pH	G	B	S_o		
β	0.9979	0.8829	0.8891	0.6702	0.6724	0.6324	0.8040	0.4041	0.4736	5.7942	2
α	0.8992	0.9978	0.9382	0.6603	0.6670	0.6637	0.8347	0.4743	0.6447	6.1162	**1**
P	0.7661	0.9109	0.9882	0.5122	0.6161	0.5266	0.7997	0.3666	0.4056	5.3654	3
t	0.6046	0.7348	0.6983	0.9951	0.3850	0.3198	0.5591	0.1943	0.5942	4.7654	5
C	0.7260	0.5148	0.4298	0.2769	0.9944	0.6236	0.3680	0.2323	0.2402	3.7824	8
pH	0.6984	0.7919	0.4924	0.3482	0.4161	0.9963	0.6446	0.3507	0.4930	4.2353	7
G	0.8542	0.8958	0.8656	0.4672	0.6399	0.5379	0.4951	0.4244	0.5733	5.2155	4
B	0.6537	0.5731	0.5228	0.3300	0.4315	0.3825	0.5842	0.9964	0.5369	4.6286	6
S	0.4458	0.4924	0.3903	0.5437	0.1710	0.4202	0.5069	0.2135	0.9982	3.7618	9
Σr	6.6459	6.7944	6.2147	4.8038	4.9934	5.1030	5.5963	3.6566	4.9597	43.6648	-
	2	**1**	3	8	6	5	4	9	7	-	0.5391

 DOI: https://doi.org/10.30564/jgr.v3i1.2520

Table 7. Parameters of the model (2) of strong binary relations

Vari-able *x*	Indi-cators *y*	Trend							Coef. correl. *r*
		Exponential law			Biotechnical law				
		a	*b*	*c*	*d*	*e*	*f*	*g*	
α	*P*	385.27012	0.11416	1.04779	-0.68619	7.18676	0.082281	3.86027	0.9382
P	*α*	8.75718	4.51102e-5	1.69628	-0.0035065	1.12627	0	0	0.9109
α	*β*	5.20774	0.015651	2.19343	-1.48679e-31	76.70776	3.92152	1.61019	0.8992
G	*α*	4.97550	4.59469e-5	2.39778	-3.17873e-16	13.45200	0.042402	1.56237	0.8958
β	*P*	227.43422	0.081611	3.17747	521.80321	1.94134	2.59545	0.20711	0.8891
β	*α*	4.62951	-0.084064	1.72524	-0.12172	3.04712	0	0	0.8829
G	*P*	179.82970	-0.030662	0.66942	2.83370e-11	9.95352	0.0025368	2.20668	0.8656
G	*β*	5.41800	0.15922	1	2.21819e7	5.28734	21.38249	0.13380	0.8542
α	*G*	90.62763	0.044913	2.38597	0	0	0	0	0.8347
β	*G*	2.19517	-6.48788	0.77000	-1423.2456	0.52794	0	0	0.8040
P	*G*	-22.20055	7.85812e-5	1.44296	2.57436e-8	4.29437	0.0091525	0.91535	0.7997
pH	*α*	0.58173	-1.49638	0.21969	-1.1458e-122	266.9847	34.29715	0.99741	0.7919
P	*β*	2.38333	0	0	2.87128e-41	19.34954	0.047959	1.01997	0.7661
t^1	*α*	2.21930	-0.0079905	3.02811	-1.07756e-6	8.95285	0	0	0.7348
C	*β*	4.71908	4.67296e-5	2.20971	-6.5156e-132	113.8644	2.91223	1.00095	0.7260

Note: $^1\ t := t + 5$.

There are 67 such trends in total in Table 5. The number of medium and strong connections is 43. Above the level of the correlation coefficient of 0.8 there are 10 patterns in the form of two-term trends, and above 0.9 - only two formulas.

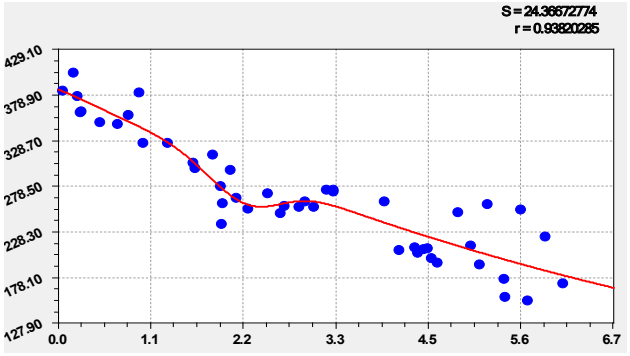

Influence of northern latitude on precipitation

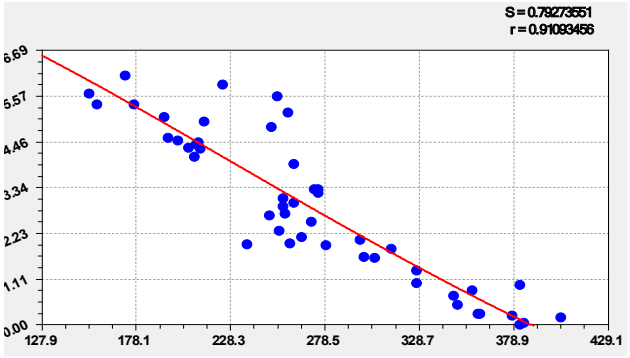

Influence of average annual precipitation on latitude

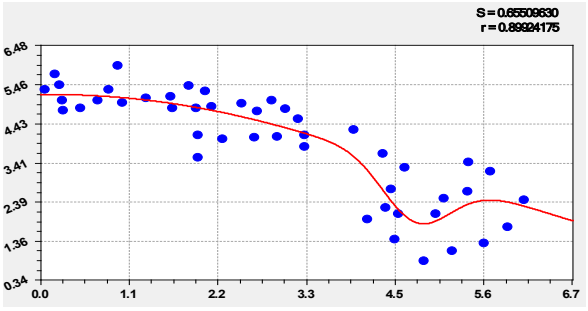

Influence of north latitude on longitude

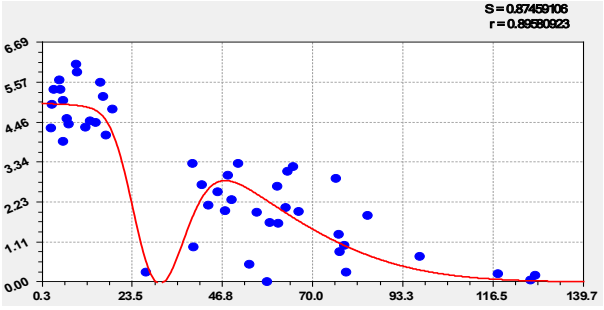

Influence of the intensity of sheep grazing on latitude

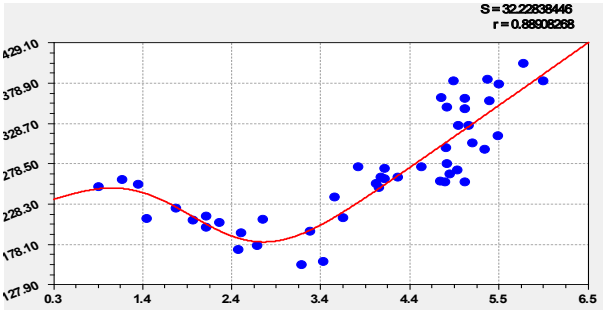

Effect of Longitude on Average Annual Precipitation

DOI: https://doi.org/10.30564/jgr.v3i1.2520

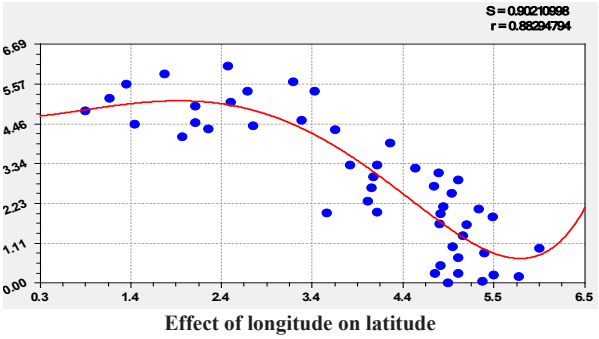

Figure 3. Graphs of strong binary relations

8. The Behavior of the System under Study

Each system under study has its own character that is different from others. It can be identified (Table 8) by increasing the admissible level of the correlation coefficient, in our example from 0 to 0.9382.

Table 8. Correlation coefficient

$[r]$	Number of formulas N	Number of lines $N_{\_}$	Number of columns $N_{\mid}$
0	72	9	9
0.1	72	9	9
0.2	72	9	9
0.3	67	9	9
0.4	57	9	9
0.5	43	9	8
0.6	30	8	8
0.7	15	7	4
0.8	10	4	4
0.9	2	2	2
0.9382	1	1	1

As the correlation coefficient increases, the number of elements in the correlation matrix decreases.

Were identified (Figure 4):

- number of formulas ($r = 0.9992$)

$$N = 72.28562\exp(-4.66149[r]^{3.20637}); \quad (3)$$

- number of lines ($r = 0.9983$)

$$N_{\_} = 9.04746\exp(-3.33716[r]^{6.78032}); \quad (4)$$

- number of columns ($r = 0.9826$)

$$N_{\mid} = 9.10864\exp(-2.69066[r]^{4.56332}). \quad (5)$$

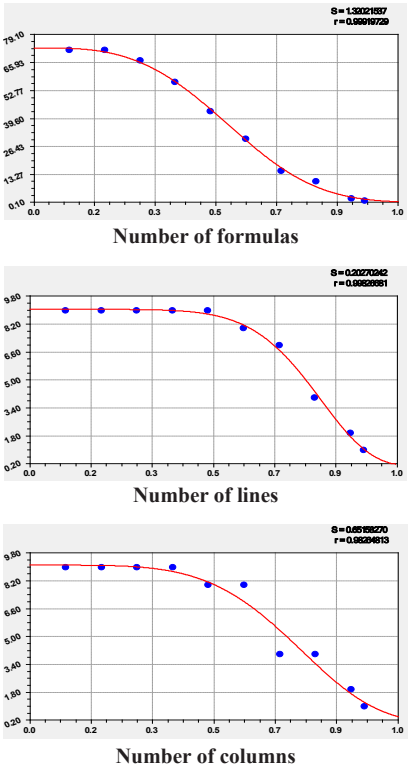

Figure 4. Graphs of the influence of the level of the correlation coefficient on the elements of the matrix

Table 9. Parameters (1) of the effect of grass productivity on the intensity of sheep grazing

i	Asymmetric wavelet $y_i = a_{1i}x^{a_{2i}}\exp(-a_{3i}x^{a_{4i}})\cos(\pi x(a_{5i}+a_{6i}x^{a_{7i}})-a_{8i})$								Coef. correl. r
	Amplitude (half) oscillation				Half-cycle			Shift	
	a_{1i}	a_{2i}	a_{3i}	a_{4i}	a_{5i}	a_{6i}	a_{7i}	a_{8i}	
1	-2.01689e-5	0	-0.036456	1	0	0	0	0	
2	4.42987e-14	7.61296	0.024339	1.02741	0	0	0	0	0.7056
3	1.30194	0	-0.00073656	1.44782	15.42255	0.016374	0.98593	0.98593	
4	-6.53119	0	-0.00031845	1.39411	46.59723	-0.10305	0.96038	-0.23871	0.3622
…	…	…	…	…	…	…	…	…	…
40	5.34235e-39	18.76901	0.051556	1.03614	1.61095	0	0	4.06617	0.4142

 DOI: https://doi.org/10.30564/jgr.v3i1.2520

The quality factor of the initial data in Table 1 is very high.

9. Wavelet Analysis of Bioclimatic Pairs

Many binary relations, in addition to two-term trends, receive additional oscillatory disturbances. For example, several wavelets have pairs α-α (rank distribution), β-α (vibrational geomorphology), P-β (climatic geomorphology), pH-P (soil science). The number of asymmetric wavelets is even greater in pairs P-α (climatic geomorphology) and P-G (sheep breeding).

And, finally, 40 wavelets (Table 9, Figure 5) were found in the pair B-G(grass - sheep).

Taking into account other factors, it is possible to distinguish individual groups in different scientific areas of steppe studies (geography, geomorphology, climatology, sheep breeding, etc.).

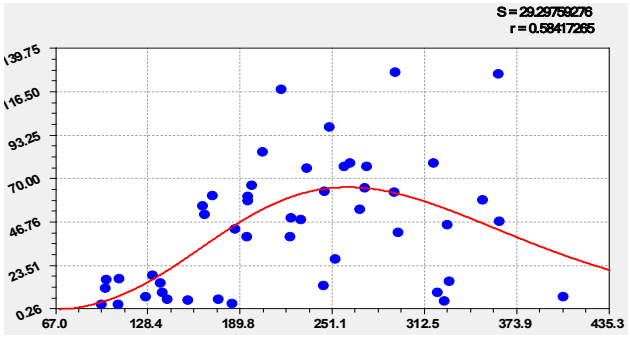

A trend with two components

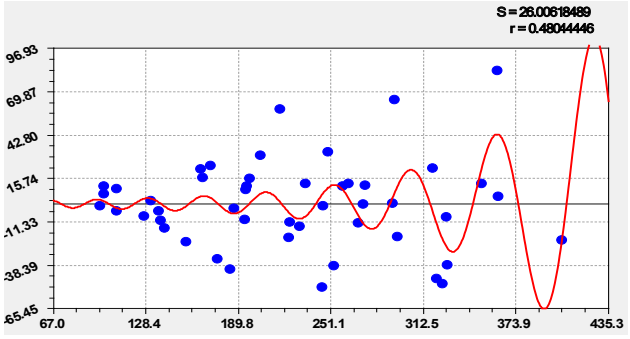

First hesitation

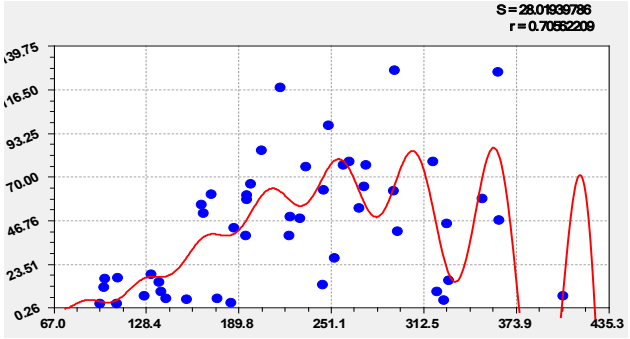

Trend and first vibrational disturbance

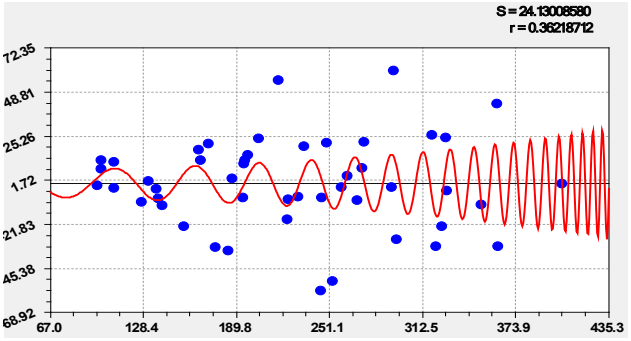

The fourth member of the model (1)

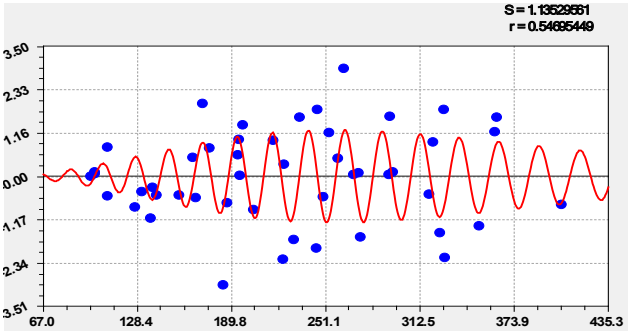

39th asymmetric finite-dimensional wavelet

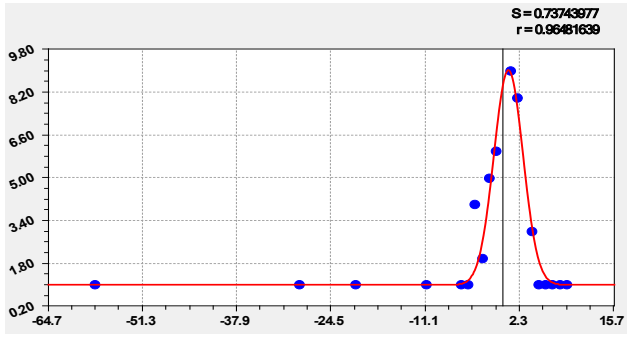

Distribution of error after the 40th term

Figure 5. Graphs of the effect of grass productivity on the intensity of sheep grazing

The first term in the trend with a negative sign shows that when the productivity of steppe grass is less than 75 g/m^2, the intensity of sheep grazing is zero. Then, for the second member, an optimum of 270 g/m^2 occurs, at which a maximum of 65 sheep grazing intensity is possible on average, 65 pcs/km^2. The first fluctuation shows that with an increase in grass biomass, there is a loss of stability of the grass cover with a sharp exponential growth of the amplitude. The second fluctuation is dangerous in that with an increase in the productivity of the grass biomass, the half-period of the fluctuation sharply decreases and this will also lead to the collapse of the steppe grass cover.

After the 40th term, the distribution of the amount n of relative error Δ (Figure 5) changes according to the

DOI: https://doi.org/10.30564/jgr.v3i1.2520

Gauss law (the so-called normal distribution law)

$$n = 1 + 8.02576 \exp(-0.11715(\Delta - 0.66006)^2). \quad (6)$$

Environmental and technological experiences are valid when $[\Delta] = \pm 30\%$. This condition is not satisfied only by one test site No. 44 with a maximum relative error of -57.36%. Then the representativeness of all experiments is 100 (48-1) / 48 = 97.9%.

Of interest is also the reverse effect (Figure 6) of sheep on grass G - B according to the formula

$$B = 1.34422 \cdot 10^{-11} \exp(0.23425 G^{0.99779}) + 142.76037 G^{0.13788} \exp(-1.17222 \cdot 10^{-5} G^{1.93557}) \quad (7)$$

with a correlation coefficient of 0.4204. From the point distribution of residues in Figure 6, it can be seen that there are three clusters in the intervals of sheep grazing intensity: (1) from 0 to 30 pcs / km^2; (2) from 30 to 95 units / km^2; (3) more than 95 pcs / km^2. In this case, the variability of the productivity of the grass decreases.

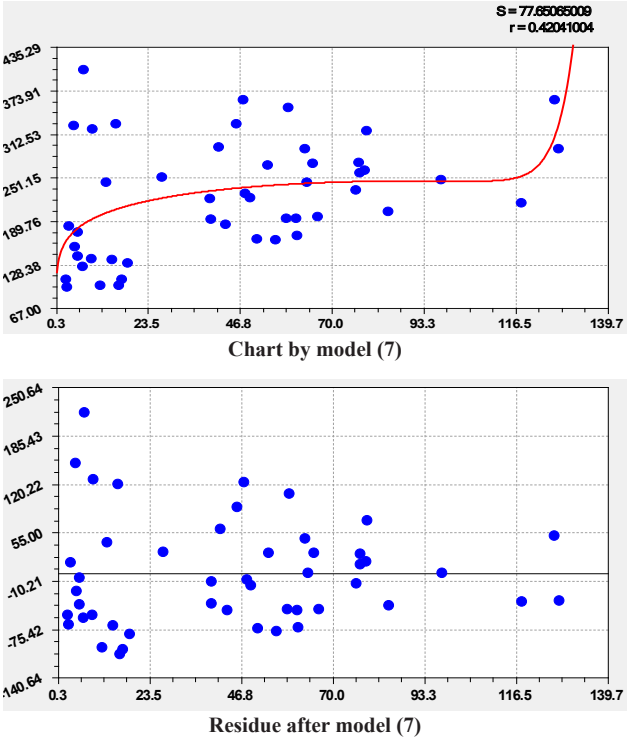

Figure 6. Graphs of the influence of the intensity of sheep grazing on grass productivity

In the first cluster, apparently, the best quality grass grows, and in the third cluster, due to overgrazing of sheep, the species composition and quality of the grass deteriorate. At the same time, according to the first term of formula (7), the biomass of steppe grass increases sharply. It can be seen from the second term that stress excitation of the grass cover occurs as a positive response to an increase in the intensity of sheep grazing. Without sheep, biomass is below 80 g/m^2. With an optimum grazing intensity of 70 pcs/km^2, on average, the productivity of grass biomass increases 2.5 times.

10. Conclusion

Of the nine factors taken into account, the most active are the geographic coordinates of 48 test sites. This circumstance proves that the geomorphology of the steppes on the eastern section of Eurasia in Mongolia and Inner Mongolia of China is becoming decisive in climatic geomorphology and other scientific areas.

Factor analysis showed that the first of the nine four places for influencing variables and dependent indicators are the same: in the first place is the north latitude, the second is the east longitude, the third is the average annual precipitation, and the fourth place is the intensity of sheep grazing. The rest of the factors are located in different ways. For example, the average annual temperature as an influencing variable is in fifth place, but as a dependent indicator only in eighth place.

The density of organic carbon was found to be only in ninth place as an influencing variable, and in seventh place as a dependent indicator. This is based on the fact that organic carbon is an accumulative (cumulative) parameter over many years.

The productivity of the biomass of steppe grass as an influencing variable is in sixth place, and as a dependent indicator (criterion) only in ninth place. This parameter is seasonal, therefore, in comparison with organic carbon, it is highly dynamic.

The average annual temperature as an influencing variable is in fifth place, after the intensity of grazing of sheep, and as a dependent indicator only in eighth place. This was influenced by the strong averaging of the parameter (average value for the year). Plants are strongly influenced by the temperature dynamics during the growing season [6], and even more by the sum of temperatures during the growing season.

When the productivity of steppe grass is less than 75 g/m^2, the intensity of grazing of sheep is zero. According to the second term of the model, an optimum of 270 g/m^2 appears with a maximum of sheep grazing intensity on average 65 pcs/km^2. The first fluctuation shows that with an increase in grass biomass, there is a loss of stability of the grass cover with an exponential increase in the amplitude. The second fluctuation is dangerous because with an increase in the grass biomass, the half-period of the fluctuation sharply decreases and this

 DOI: https://doi.org/10.30564/jgr.v3i1.2520

will also lead to the collapse of the steppe grass cover. From the remnants of the effect of sheep grazing on grass biomass, it can be seen that there are three clusters: (1) from 0 to 30; (2) from 30 to 95; (3) more than 95 pcs/km^2. In this case, the variability of the productivity of the grass decreases.

The reported study was funded by Russian Foundation for Basic Research, Government of Krasnoyarsk Territory, Krasnoyarsk Regional Fund of Science, to the research project: Predictions of the ecological-economic potential for possible "climatic" migrations in the Angara-Yenisei macroregion in a changing climate of the 21st century.

References

[1] Mazurkin P.M. Factor analysis of the subjects of the Russian Federation by shares of land. Scientific and practical journal "Natural resources of the Earth and environmental protection", 2020, 1(6): 14-23. (in Russia)
http://dx.doi.org/10.26787/nydha-2713-203X-2020-1-6-14-23.

[2] Mazurkin P.M., Mikhailova S.I. Distribution of plant mass in forest-meadow phytocenosis. Bulletin of the UMO on education in the field of environmental engineering and water use, 2011, 3: 330-340. (in Russia)

[3] Saati T. Decision-making. Hierarchy analysis method. M.: Radio and communication, 1993: 274. (in Russia)

[4] Torsuev N.P. Popular ecology (useful advice in everyday life). Kazan: Publishing house "Ecocenter", 1997: 236. (in Russia)

[5] Mazurkin P.M., Kudrjashova A.I. Factor analysis of annual global carbon dynamics (according to Global_Carbon_Budget_2017v1.3.xlsx). Materials of the International Conference "Research transfer". Reports in English (part 2), Beijing, PRC., 2018: 192-224.

[6] Mazurkin P.M., Kudryashova A.I. Factor analysis of meteoparameters on the stage of growth of birch leaves. International Journal of Current Research. 11(10): 7774-7779.
DOI: https://doi.org/10.24941/ijcr.36856.10.2019

[7] Zhao Y., Ding Y., Hou X., Li F.Y., Han W., Yun X. Effects of temperature and grazing on soil organic carbon storage in grasslands along the Eurasian steppe eastern transect. PLoS ONE, 2017, 12(10).
DOI: https://doi.org/10.1371/journal.pone.0186980

DOI: https://doi.org/10.30564/jgr.v3i1.2520

BILINGUAL PUBLISHING CO.
Pioneer of Global Academics Since 1984

Journal of Geological Research
https://ojs.bilpublishing.com/index.php/jgr-a

ARTICLE

Hydrocarbon Play Assessment of "Oswil" Field, Onshore Niger Delta Region

Osisanya, W.O.[1*] Alile, O.M.[1] Eze, S.U.[2] Ibitoye, T.A.[3] Oyanameh, O.E.[4]

1. Department of Physics, University of Benin, Benin City, Edo state, Nigeria
2. Department of Marine Geology, Nigeria Maritime University, Okerenkoko, Delta State
3. Department of Petroleum Engineering and Geosciences, Petroleum Training Institute, Effurun, Nigeria
4. Department of Earth Science, Anchor University, Lagos, Nigeria

ARTICLE INFO

Article history
Received: 8 January 2021
Accepted: 21 January 2021
Published Online: 31 January 2021

Keywords:
Seismic
Well logs
Petrophysical parameters
Hydrocarbon play
Structural interpretation
Niger Delta

ABSTRACT

Hydrocarbon play assessment of any field involves the evaluation of the production capacity of hydrocarbon reservoir unit in the field. This involves detail study of the reservoir petrophysical properties and geological interpretation of structures suitable for hydrocarbon accumulation in the field as observed from seismic reflection images. This study details the assessment of hydrocarbon play in OSWIL field onshore in Niger Delta, with the intent of appraising its productivity using a combination of seismic, well logs, petrophysical parameters and volumetric estimation using proven techniques which involves an integrated methodology. Two reservoir windows "R1" and "R2" were defined from five wells OSWIL-02, 04, 06, 07 and 12. The top and base of each reservoir window was delineated from the wells. Structural interpretation for inline 6975 revealed two horizons (X and Y) and eight faults labelled (F1, F2, F6, F8, F10, F16, F17 and F18). Five faults (F1, F6, F10, F17 and F18) were identified as synthetic faults and dip basin wards while three faults (F2, F8 and F16) were identified as antithetic faults and dips landwards. Time-depth structural map at top of reservoirs R1 and R2 revealed structural highs and closures. These observations are characteristics of growth structures (faults) which depicts the tectonic style of the Niger Delta. Results of petrophysical evaluation for reservoirs "R1" and "R2" across the five wells were analysed. For reservoir "R1" effective porosity values of 27%, 26%, 23%, 20% and 22% were obtained for wells OSWIL-04, 12, 07, 06 and 02 respectively with an average of 23.6%, while for reservoir "R2" effective porosity values of 26%, 22%, 21%, 24% and 23% for wells OSWIL-04, 12, 07, 06 and 02 were obtained respectively with an average of 23.2%. This porosity values correspond with the already established porosity range of 28-32% within the Agbada formation of the Niger Delta. Permeability index of the order (K > 100mD) were obtained for both reservoirs across the five wells and is rated very good. Hydrocarbon saturation (Shc) across the five wells averages at 61.6% for reservoir "R1" and 67.4% for reservoir "R2". Result of petrophysical model for porosity, permeability and water saturation reveal that the reservoir system in R1 and R2 is fault assisted and fluid flow within both reservoirs is aided by presence of effective porosity and faulting. Volumetric estimation for both reservoirs showed that reservoir R1 contains an estimate of 455 × 106 STB of hydrocarbon in place, while reservoir R2 contains an estimate of 683 × 106 STB of hydrocarbon in place. These findings impact positively on hydrocarbon production in the field and affirm that the two reservoirs R1 and R2 are highly prospective.

**Corresponding Author:*
Osisanya, W.O.,
Department of Physics, University of Benin, Benin City, Edo state, Nigeria;
ORCID iD: 0000-0003-0953-0609;
Email: uchechukwueze2014@gmail.com

 DOI: https://doi.org/10.30564/jgr.v3i1.2783

1. Introduction

Nigeria oil and gas industries presently are faced with the challenge of meeting up with the national crude oil reserve target of 40 billion barrels due to inadequate exploration and exploitation of the available natural hydrocarbon deposit in the nation. Records show that only one-third of oil in place has been recovered through the conventional method of production [1-4]. The domestic need is bolstered by the current government policy thrust for additional gas turbines for power generation and industrial projects. Therefore, the future reserve/production ratio for oil/gas in Nigeria will be a cause for serious concern based on the present available reserves data, if additional reserves are not discovered. Hence, this necessitates the assessment of hydrocarbon play of the subsurface geology using different proven and cost effective techniques in the exploration of oil and gas within the Niger Delta region in achieving its national demand. A petroleum play, or simply a play, is defined as a group of oil fields or prospects in the same region that are controlled by the same set of geological circumstances [5]. The geological component of consideration in the assessment of hydrocarbon play are migration pathway, reservoir rock, a matured source rock, trap and seal. Nevertheless, an effective play is only made up of a reservoir rock, a trap and its sealing mechanism which are located within a sedimentary terrain [6].

If the various elements that make up a play are identified on a play assessment map, then exploration of the entire prospects in the field is possible not just a single prospect. The geophysical method that provides the most detailed picture of subsurface geology to delineate the various elements that constitutes a hydrocarbon play in an oil field is the seismic methods. The seismic reflection method ever since its discovery in the late 1920s, has and still remains one of the most effective tools in the search for hydrocarbons. Reflections are due to contrast in acoustic impedance in the subsurface caused by difference in physical properties of rocks with different lithologies, which can be density and compressional wave velocity and can be explained in terms of lithology, porosity and porefill [7-10].

The goal of a 3D seismic survey is to delineate subsurface structures, as well as acquire exact definition of rock physical properties which aid in mapping of geological structures suitable for hydrocarbon accumulation [4,11]. Structural traps, made up of the reservoir rock and its sealing mechanism are usually more evident on seismic records, and forms the basis of structural seismic interpretation aided by conventional interpretation platforms [12,13]. With advancement in technology, the use of seismic data has extended to other areas such as hydrocarbon play exploration beneath existing fields and pore-fluid estimation. These applications have led to the discovery of potential oil and gas reserves which have not been exploited. Hydrocarbon play assessment of any hydrocarbon reservoir depends on structural disposition of the reservoir and reservoir properties such as porosity, permeability and water saturation distribution of the reservoir. These petrophysical properties are key contributors to hydrocarbon reservoir characterization. Estimation of the structural and petrophysical evaluation of every reservoir unit require the integration of seismic and well log data, to describe the reservoir properties in terms of its structural disposition as observed from seismic records within a particular field [3]. This study intends to resolve the ambiguities that are associated with hydrocarbon play assessment of "OSWIL" field onshore Niger Delta, through the adoption of an integrated methodology which combines result of structural seismic interpretation and petrophysical analysis to evaluate the production capacity of the reservoirs delineated in the field.

2. Geology of the Study Location

OSWIL Field is basically an onshore field located within the Niger Delta between latitudes 5^0 24'0" N and 5^0 30' 0" N and longitudes 6^0 0' 30" E and 6^0 7' 0" E. The Field has five wells identified as OSWIL-02, 04, 06, 07 and 12 (Figure 1).

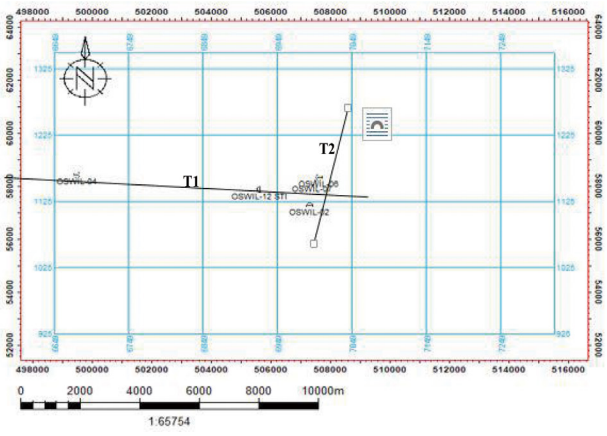

Figure 1. Base map of the study area Oswil Field, showing the grid seismic lines and well locations along traverses T1 and T2

The Niger Delta basin evolved in early Cenozoic times where rapid deposition and subsidence have occurred overtime [14]. Thickness of sediments in the Niger Delta is over 12 km on the basin depocentre [4,15]. The early Niger Delta is interpreted as being a river-dominated delta, how-

DOI: https://doi.org/10.30564/jgr.v3i1.2783

ever the post-Oligocene delta is a typical wave-dominated delta with well-developed shoreface sands, beach ridges, tidal channels, mangrove and freshwater swamps [16,17,18]. Obaje [18], opined that the Niger Delta is one of the world's largest deltas and shows an overall upward transition from marine shales (Akata Formation) through a sand-shale paralic interval (Agbada Formation) to continental sands of the Benin Formation.

Depending on relative sea level changes, local subsidence and sediment supply, the delta experiences episodes of regressions and transgressions [4,19,20]. Tectonics in the Niger delta rifting diminished in the Late Cretaceous. After rifting ceased, gravity tectonics became the primary deformational process. The stratigraphic arrangement of the Niger Delta is made up of three lithostratigraphic units namely; a continental shallow sand unit - the Benin Formation, a coastal marine unit of alternating sands and shales - the Agbada Formation and a basal marine shale unit-the Akata Formation. The Akata Formation consists of clays and shales with minor sand alternations [18]. The sediments were deposited in prodelta environments, with sand percentage less than 30% [4,20]. The Agbada Formation consists of alternating sand and shales representing sediments of the transitional environment comprising the lower delta plain (mangrove swamps, floodplain and marsh) and the coastal barrier and fluvio marine realms. According to Obaje [18], the sand percentage within the Agbada Formation varies from 30 to 70%, which results from the large number of depositional off lap cycles. A full cycle generally consists of thin fossiliferous transgressive marine sand, followed by an offlap sequence which commences with marine shale and continues with laminated fluvio marine sediments followed by barriers and/or fluviatile sediments terminated by another transgression cycle [21,22] as cited in [20]. The Benin Formation is characterized by high sand percentage (70-100%) and forms the top layer of the Niger Delta depositional sequence (Alao et al. 2013). According to Obaje (2009), the massive sands were deposited in continental environment comprising the fluvial realms (braided and meandering systems) of the upper delta plain[23].

3. Methodology

Available data used for this study includes; 3D Seismic data volume (in SEG-Y format), Well logs (Gamma Ray, Resistivity, Neutron and Density logs), Check shot, and Well deviation. The suite of data were obtained from Shell Petroleum Development Company (SPDC). The workflow algorithm adopted for this study is shown below (Figure 2).

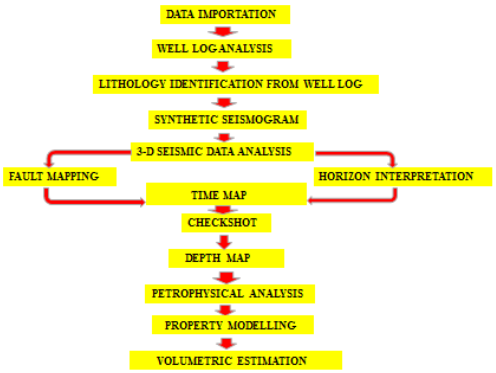

Figure 2. Research Workflow

Lithology identification was done using gamma ray log signature. Two reservoir windows R1 and R2 (sand units) were identified at top and base across the five wells following deflection of the gamma ray and resistivity log signatures. Since shale most times behaves like a radioactive element, the volume of shale (V_{sh}) in the reservoir sand was calculated using gamma ray log. Also gamma ray log was used to discriminate porous from non-porous beds, and to determine bed boundaries within the Formation. From GR log and Neutron-density crossover within porous and permeable Formations, three lithologies were delineated as Sand, Shaly sand and Shale (Figure 4a & b). Litho-stratigraphic correlation which is the determination of the continuity and equivalence of lithologic units, particularly across reservoir sands was carried out across the wells along traverses T1 and T2 shown on the base map (Figure 1). Wells Oswil-04, 12 and 07 along traverse T_1 runs from West-East of the base map, while wells Oswil-02, 07 and 06 along traverse T_2 runs from North-South on the base map (Figure 1). This formed the basis for correlation of the wells along traverses T1 and T2 to determine the lateral extent of the reservoir window across the wells.

Well-to-seismic tie, which seek to import well information into the seismic, was carried out using checkshot data from well Oswil-12. The major reflection lines that represent the tops and bases of reservoirs R1 and R2 identified on wells were mapped on the seismic section as time surfaces, this was thereafter converted to depth maps using lookup function (a relationship between time and depth) generated from the check-shots data. The well was tied to the full stack seismic data. A zero phase wavelet which was flattened with a choice filter (Butterworth wavelet) was used for the convolution of the impedance log (product of sonic velocity and density logs from OSWIL-12 well) with a bulk shit of -15ms to ensure the synthetic ties with the field seismogram. The synthetic seismogram is an artificial seismic section and considered as the convolution

 DOI: https://doi.org/10.30564/jgr.v3i1.2783

of the assumed source function (seismic wavelet) with the reflectivity function [24]. By means of the synthetic seismogram, valuable insights can be obtained about the subsurface geology responsible for a particular seismic event as observed from seismic records.

It represents the acoustic impedance in a layered model. The synthetic seismogram provides a means for well-to-seismic tie which gives a better geologic meaning to the seismic reflection data [25].

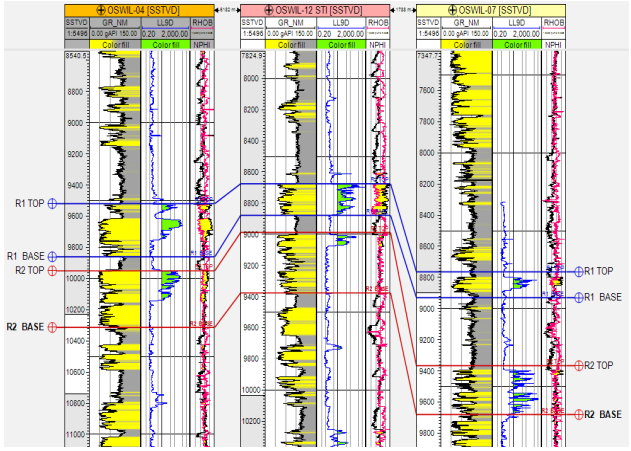

Figure 3a. Litho-Stratigraphic Correlation of the Studied Wells along traverse T_1 Oswil Field Niger Delta

3.1 Reservoir Petrophysical Parameters and Hydrocarbon Volumetric Estimation

Petrophysical estimations were carried out for the five wells that penetrated the two reservoirs (R1 and R2) in the area of study. From wireline logs, empirical expressions were used to determine the following parameters Net-to-Gross (NTG), Volume of shale (V_{sh}), porosity (Φ), permeability (K) and water saturation (S_w).

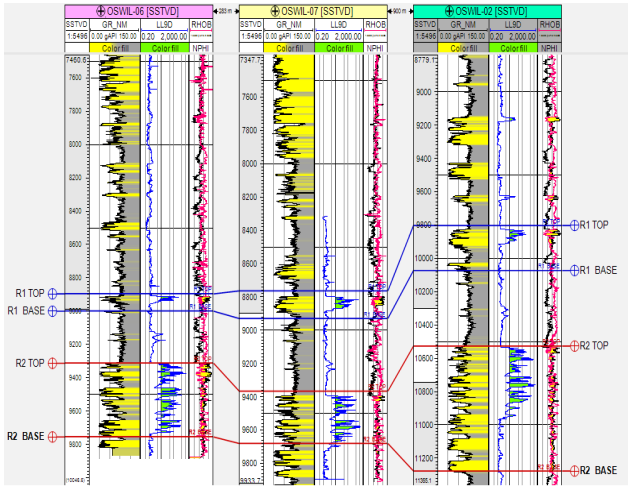

Figure 3b. Litho-Stratigraphic Correlation of the Studied Wells along traverse T_2 Oswil Field Niger Delta

Net-to Gross (NTG) measures the potential productive part of a reservoir either as a percentage or fraction of the producible (Net) reservoir within the entire (Gross) reservoir zone.

Net-to gross was computed as a percentage using the expression [3,26]:

$$NTG = (h/H) \times 100\% \quad (1)$$

where; NTG= Net to Gross, h = Net reservoir thickness and H= Gross reservoir thickness.

The volume of shale (V_{sh}) was calculated from gamma ray log using the linear method of estimation which requires determining the gamma ray response of clean sand associated with no shale (GR_{min}) and a zone of 100% shale (GR_{max}). Presence of shale within a sand unit makes the porosity log record a high porosity value, low hydrocarbon saturation and thus, low resistivity reading. This however, makes it challenging to control productive zones of a reservoir volume of shale in unconsolidated Tertiary Niger Delta basin. The formula we adopted was the linear equation proposed by [27]:

$$GR_{index} = \frac{GRiog - GR\min}{GR\max - GR\min} \quad (2)$$

where; GR_{index} = gamma ray index, GR_{Log} = GR log reading of the formation, GR_{min} = minimum GR log value in clean sand and GR_{max} = maximum GR log value in 100% shale.

Volume of Shale (V_{sh}) was obtained for the two reservoirs R1 and R2 within the five wells using Larionov tertiary rock method [26,28] given as:

$$(V_{sh}) = 0.083(2^{3.7*IGR} - 1) \quad (3)$$

where; V_{sh} = Volume of Shale and IGR = Index gamma ray.

Porosity is described as the percentage of pore spaces to total bulk volume of the rock. Porosity is taken as the measure of the void space relative to the entire reservoir volume and shows the storage strength of the given reservoir to pore fluids.

Porosity was determined from bulk density log using:

$$\phi(Den) = \frac{\rho_{ma} - \rho_b}{\rho_{ma} - \rho_{fl}} \quad (4)$$

Where; f_{Den} = density derived Porosity, r_{ma}= Matrix density usually 2.65 g/cm^3 for sandstones, r_b = bulk density of formation, r_{fl} = Fluid density usually 0.9 g/cm^3.

DOI: https://doi.org/10.30564/jgr.v3i1.2783

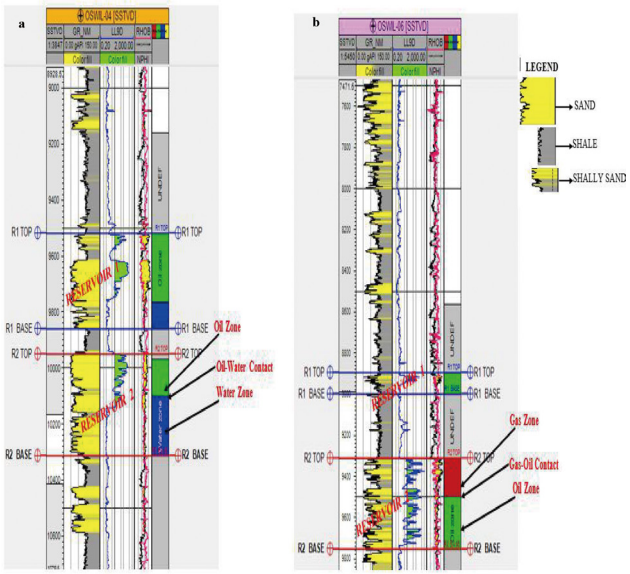

Figure 4 (a). Reservoir window and fluid distribution on OSWIL-04 Well (b). Reservoir window and fluid distribution on OSWIL-06 Well. The top and base of reservoirs R1 and R2 is shown for both wells, and fluid distribution within the reservoir shows Oil-Water contact for OSWIL-04 Well and Gas-Oil contact for OSWIL-06 Well

The porosity value computed above is regarded as total porosity $\{\Phi_{Total}\}$. When the pore spaces are interconnected the porosity is described by the term "effective porosity" and this porosity accounts for the free flowing fluid within the reservoir.

For effective porosity estimation we adopted the expression:

$$(\Phi_{eff}) = (1\text{-}V_{sh})* \Phi_{Total} \quad (5)$$

where; Φ_{eff} = effective porosity, V_{sh} = volume of shale and Φ_{Total} = total porosity.

Permeability which is the degree or measure of the ease of flow through a medium via its interconnected pores, capillaries or fractures. It is expressed in Darcy.

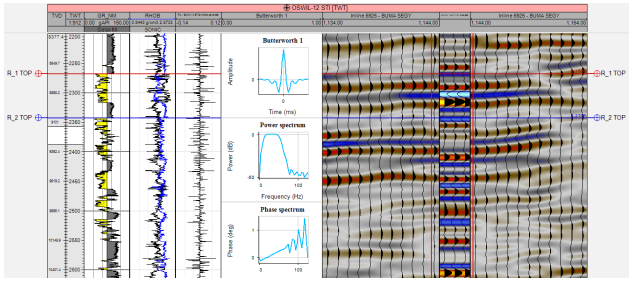

Figure 5. Seismic-to-well Tie for OSWIL-12 Well

Empirically, it is observed that very few rocks have a 1Darcy value of permeability. In practice, permeability computation in static reservoir modelling is done in a given direction in an anisotropic sandstone material, and often in the horizontal direction ($Ki_{(x)}$) along the principal axis of the permeability tensor ellipsoid [29]. Permeability index is usually expressed in millidarcies or as a fraction in 1/1000 of a Darcy.

Usually, increase in porosity could imply an increase in permeability prospect although porosity is not directly related to permeability. Factors such as Pore size, shape and continuity (pore geometry) and porosity influences the permeability of a rock formation.

The Tixier [30] model was used in computing permeability index (k) given as:

$$K = \sqrt{\{250 * \Phi_{eff}^{3}\}} / S_{wirr} \quad (6)$$

where; K = permeability index, Φ_{eff} = effective porosity and S_{wirr} = irreducible water saturation defined by [31] as:

$$S_{wirr} = (F/2000)^{1/2} \quad (7)$$

F is the formation factor (F) given by Archie [32] as:

$$F = a / \phi^{m} \quad (8)$$

where; a = Empirical constant = 0.62, and
m = cementation factor = 2.15.

Water saturation (Sw) was determined using the Archie [32] model (for clean sand formations) [3,33].

$$S_w = \left(\frac{aR_w}{\phi^m R_t}\right)^{1/n} \quad (9)$$

where; S_w = water saturation of un-invaded zone, R_w = Formation water resistivity, R_t = True Formation Resistivity (Un-invaded zone), ϕ = Effective Porosity,
a = Empirical constant defined in Equation (8),
m = Cementation exponent defined in Equation (8),
n = Saturation exponent.

For hydrocarbon saturation (S_h) we adopted the expression;

$$S_h = (1\text{-}S_w) \quad (10)$$

3.2 Fault / Horizon Mapping, Creation of Surface and Depth maps and Petrophysical Models

Fault mapping was done by picking fault segments on vertical seismic sections. Faults were identified on inline 6975 of the seismic section and two horizons (A and B) were picked on inline 6975. Eight faults were mapped on inline 6975. Structural time map and depth map were generated at top of reservoirs R1 and R2. Petrophysical fluid distribution models of porosity, permeability and fluid sat-

DOI: https://doi.org/10.30564/jgr.v3i1.2783

uration were generated as surface maps for reservoirs R1 and R2. These models were generated by distributing the estimated petrophysical properties (porosity, permeability and water saturation) along each well path across the entire reservoir structure using geo-statistical techniques. The geo-statistical algorithm applied in distributing the facies is the Sequential Indicator Simulation (SIS) [34], while the geo-statistical algorithm applied in distributing the petrophysical properties across the wells in the field is the Sequential Gaussian Simulation (SGS) [35].

3.3 Estimation of Stock Tank Oil in Place (STOIIP) within the Reservoir

Attempts were made to estimate the stock tank oil initially in place (STOIIP) for both reservoirs R1 and R2 to appraise the prolific nature of both reservoirs for field development. To determine the Stock Tank Oil Initially in Place (STOIIP), we adopted the expression:

$$STOIIP = 7758*A*h*\Phi*(1-S_w)*1/B_o \quad (11)$$

where; 7758 = Acre-feet conversion for oil, A = Area in acres, h = Net Pay thickness in feet, Φ = Porosity

S_w = Water saturation, $(1-S_w)$ = hydrocarbon saturation,

B_o = Formation volume factor [36].

Table 1. Petrophysical parameters of Reservoir R1

	Parameters	OSWIL-04	OSWIL-12	OSWIL-07	OSWIL-06	OSWIL-02
Reservoir R1	Top(ft)	9520	8660	8660	8900	9800
	Base(ft)	9860	8880	8920	9000	10,180
	Gross Thickness(ft)	340	220	260	100	380
	Net Thickness(ft)	254	186	96	32	148
	Net/Gross	74	84	36	32	38
	V_{sh} (%)	7	12	14	12	11
	Φ_{Eff} (%)	27	26	23	20	22
	F	20.46	26.28	31.87	48.06	36.88
	K (mD)	1164	1440	626	477	727
	S_{wrr} (%)	0.094	0.102	0.11	0.133	0.12
	S_w (%)	43	29	52	32	36
	Sh (%)	57	71	48	68	64

Table 2. Petrophysical parameters of Reservoir R2

	Parameters	OSWIL-04	OSWIL-12	OSWIL-07	OSWIL-06	OSWIL-02
Reservoir R2	Top(ft)	9950	8988	9366	9312	10,527
	Base(ft)	10,313	9376	9680	9754	11,277
	Gross Thickness(ft)	363	388	314	442	750
	Net Thickness(ft)	339	342	212	297	543
	Net/Gross	93	88	68	67	72
	V_{sh} (%)	8	11	15	10	13
	Φ_{Eff} (%)	26	22	21	24	23
	F	18.04	31.19	31.71	24.25	26.49
	K (mD)	827	345	631	774	1078
	S_{wrr} (%)	0.091	0.12	0.11	0.103	0.106
	S_w (%)	45	21	32	23	42
	Sh (%)	55	79	68	77	58

4. Result Presentation and Discussion

The well log and 3D seismic data volume were analysed for hydrocarbon play assessment of the study area by adopting the methodology outlined above. The base map of OSWIL Field showing the grid seismic lines and location of the wells along traverses T1 and T2 is shown in Figure 1. The reservoir windows (R1 and R2) defined from well logs were correlated from top to base across OSWIL-04, 12 and 07 wells along traverse T1 oriented West-East in the field (Figure 3a) and across OSWIL-06, 07 and 02 wells along traverse T2 oriented North-South in the field (Figure 3b) using gamma ray log, resistivity log and neutron-density crossover. Figures 4a and 4b shows the reservoir fluid distribution for OSWIL-04 well (along T1) and OSWIL-06 well (along T2). For OSWIL-04 well, presence of Oil and Water was observed within reservoir windows R1 and R2 based on neutron-density crossover (Figure 4a) while for OSWIL-06 well, presence of Gas and Oil was observed within reservoir R2 (Figure 4b). Reservoir R1 has a thickness of 340 ft (9520-9860 ft) on well OSWIL-04, a thickness of 220 ft (8,660-8,880 ft) on well OSWIL-12 and a thickness of 260 ft (8,660-8,920 ft) on well OSWIL-07 (Figure 3a). This shows that reservoir R1 thins out in the eastward direction from OSWIL-04 to 07 wells. Similarly, reservoir R2 has a thickness of 363ft (9,950-10,313 ft) on well OSWIL-04, a thickness of 388ft (8988-9376ft), on well OSWIL-12 and a thickness of 314ft (9366-9680ft) on well OSWIL-07. Reservoir R-1 has a thickness of 100ft (8900-9000ft) on well OSWIL-06, a thickness of 170ft (8760-8930ft) on well OSWIL-07 and a thickness of 380ft (9800-10,180ft) on well OSWIL-02. Reservoir R1 thickens out southwards direction of the Field, while reservoir R2 has a thickness of 442ft (9312-9754ft) on well OSWIL-06, a thickness of 310ft (9370-9680ft) on well OSWIL-07 and a thickness of 750ft (10,527-11,277ft) on well OSWIL-02.

Petrophysical parameters computed for the two reservoirs "R1" and "R2" within the five wells is shown in Tables 1 and 2. The parameters of interest includes: gross thickness, net thickness, net-to gross, volume of shale, effective porosity, permeability, water saturation and hydrocarbon saturation.

The petrophysical parameters revealed reservoir R1 (Table 1) has an average net to gross of 52.8% and average shale volume of 11.2% across the wells. Effective porosity of R1 ranges from 20 to 27%, permeability index ranges from 477 to 1440 mD and hydrocarbon saturation from 48 to 71% across the wells. Porosity and permeability values obtained for reservoir R1 is rated very good based on Rider [37] criteria. Similarly, reservoir R2 has an

DOI: https://doi.org/10.30564/jgr.v3i1.2783

average net to gross of 77.6% and average shale volume of 11.4%. Effective porosity of R2 ranges from 21 to 26%, permeability index ranges from 345 to 1078 mD and hydrocarbon saturation from 55 to 79% across the wells (Table 2). Similar to reservoir R1, porosity and permeability values obtained for reservoir R2 is also rated very good based on Rider [37] criteria. This imply that the reservoirs are highly connected. The effective porosity values obtained for reservoirs R1 and R2 validates the established porosity range of 28-32% in the Niger Delta.

Structural interpretation of inline 6975 on the seismic section, revealed two horizons "X" and "Y" (Figure 6) and eight faults (F1, F2, F16, F8, F10, F18, F17 and F6) which cut across the horizons (Figure 7). Five faults (FI, F10, F18, F17 and F6) were identified as synthetic faults as they dip basinward.

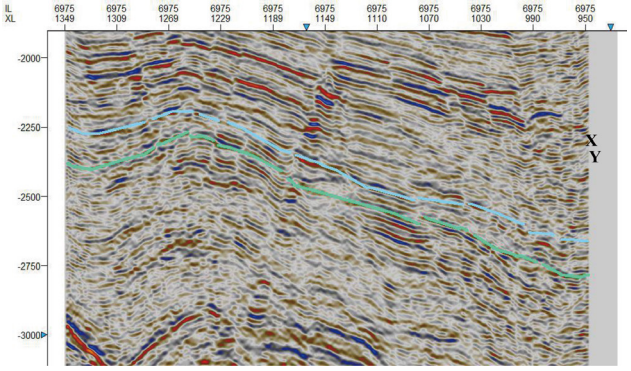

Figure 6. Horizon Mapping on inline 6975

Three faults (F2, F16 and F8) were identified as antithetic faults and dips landward. This observation is characteristic of growth structures (faults) which depicts the tectonic style of the Niger Delta. The geological structure observed (Normal faults) are favourable for hydrocarbon accumulation and will keep it from migrating vertically or laterally [11]. Figures 8a and 8b is the structural time map at top of reservoirs R1 and R2 showing the structural highs and network of faults observed in the field. Figures 9a and 9b is the depth structure map of reservoirs R1 and R2. The depth structure map shows the depth equivalence of the structures observed in the structural time map and was produced using an appropriate velocity model for time-depth conversion. The structures observed on the time-depth maps validates the existence of geological structures suitable for hydrocarbon accumulation in the study area.

Result of petrophysical models for porosity, permeability and water saturation is shown in Figures 10, 11 and 12 for reservoirs R1 and R2 respectively. The models show the distribution of the petrophysical parameters (porosity, permeability and water saturation) along well paths across the reservoir structure for reservoirs R1 and R2.

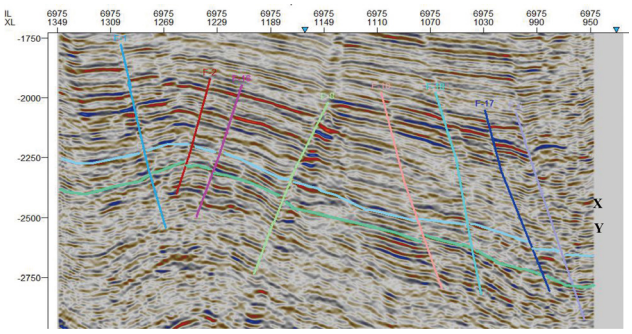

Figure 7. Interpreted Seismic Section of inline 6975

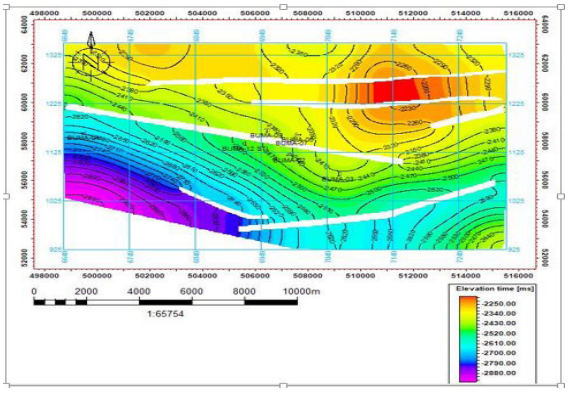

Figure 8a. Time Structure Map for Reservoir R1 Top

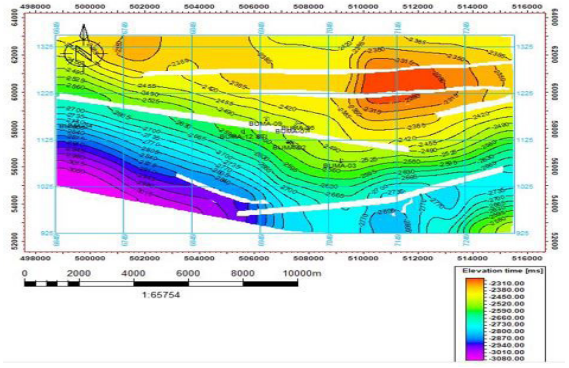

Figure 8b. Time Structure Map for Reservoir R2 Top

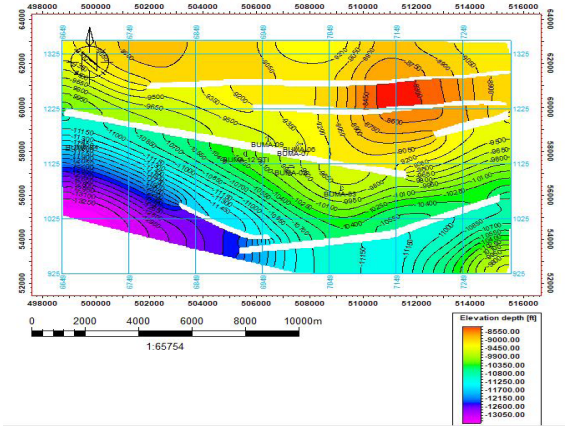

Figure 9a. Depth Structure Map for Reservoir R1 Top

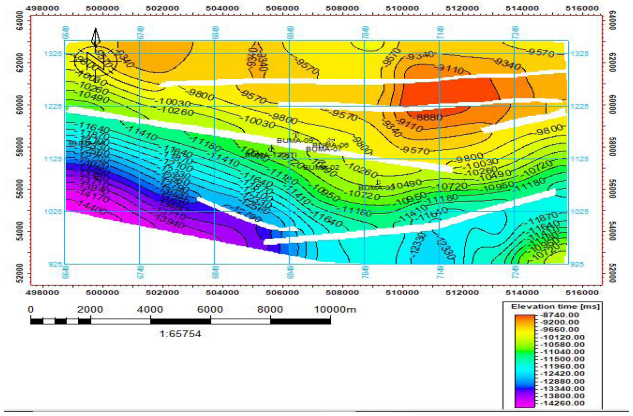

Figure 9b. Depth Structure Map for Reservoir R2 Top

Figures 10a and 10b shows effective porosity model of reservoirs R1 and R2. The model shows porosity distribution across the wells and geological structures (faults) which cuts across the reservoir penetrated by the wells. For reservoir R1, effective porosity values (in fraction porosity unit) of 0.27, 0.26, 0.23, 0.2 and 0.22 were obtained for wells OSWIL-04, 12, 07, 06 and 02 respectively with an average of 0.236 (23.6%). In Figure 10a, it was observed that porosity value of well OSWIL-04 is highest, while for other wells OSWIL-02, 06, 07 and 12, porosity values are compatible with that obtained in the Niger Delta. Figure 10b is the porosity model for reservoir R2 showing the wells penetrating the highly faulted reservoir system.

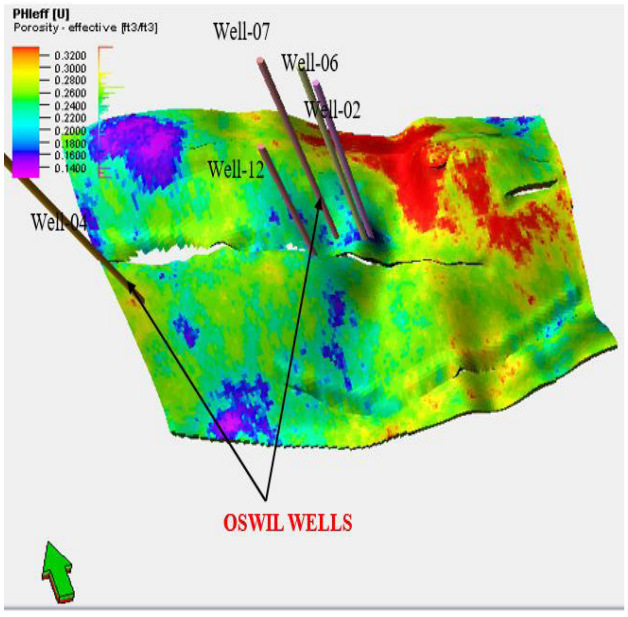

a

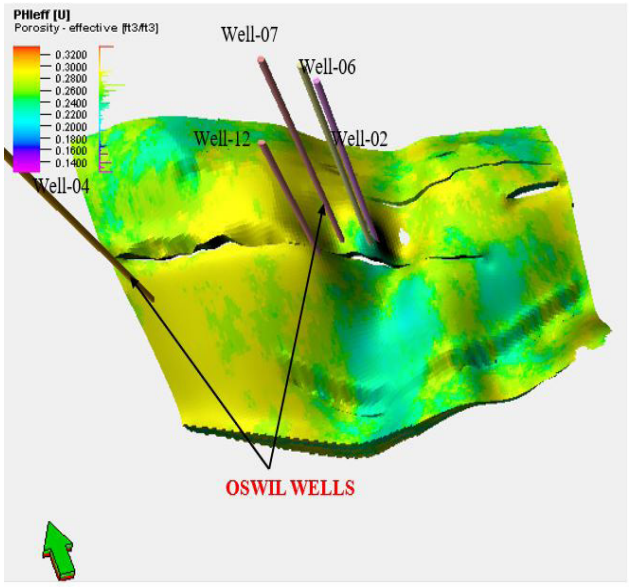

b

Figure 10. (a) Effective Porosity Model of Reservoir R1; (b) Effective Porosity Model of Reservoir R2

For reservoir R2, effective porosity values (in fraction porosity unit) obtained for wells OSWIL-04, 12, 07, 06 and 02 are 0.26, 0.22, 0.21, 0.24 and 0.23 respectively with an average of 0.232 (23.2%). Well OSWIL-04 has the highest value of porosity in reservoir R2 compared with other wells and these porosity values are compatible with that obtained in the Niger Delta. This indicates that the pore spaces within the reservoirs R1 and R2 are interconnected, and reservoir system is fault assisted hence fluid flow within the reservoir system is aided by presence of effective porosity and faulting.

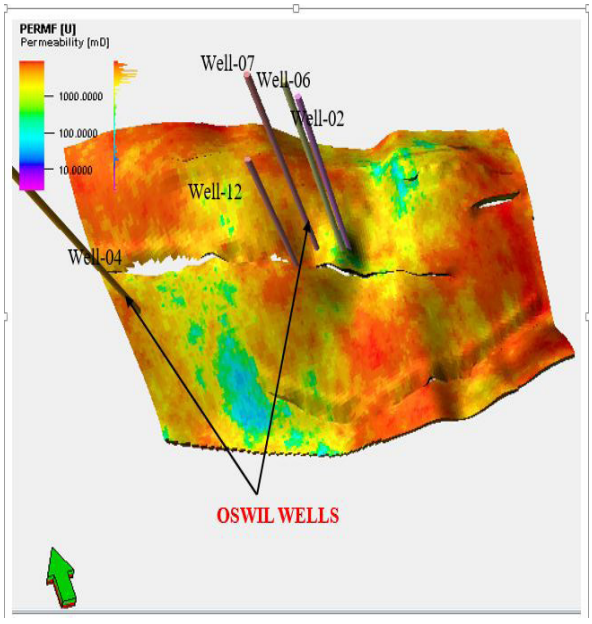

a

DOI: https://doi.org/10.30564/jgr.v3i1.2783

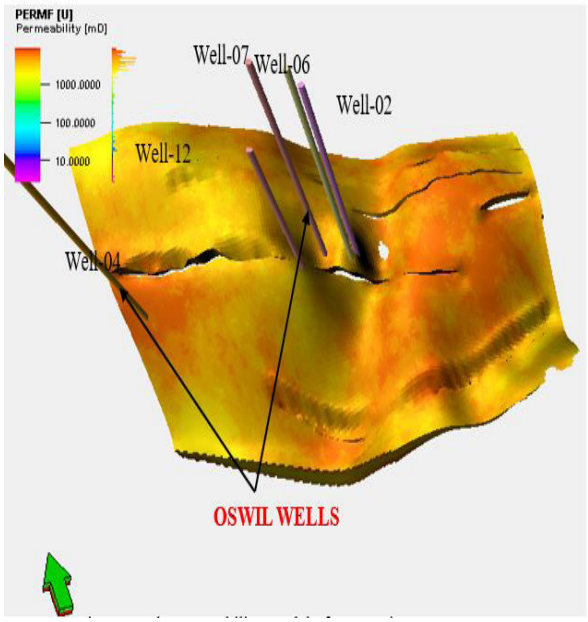

b

Figure 11. (a) Permeability (horizontal permeability) Model of Reservoir R1; (b) Permeability Model of Reservoir R2

Permeability model of reservoirs R1 and R2 is shown in Figures 11a and 11b. The permeability parameter (horizontal permeability) was modelled using the relationship that exists between core porosity and core permeability by populating the permeability logs generated. The model shows permeability in the horizontal direction for an anisotropic reservoir system, which is the direction fluid flow takes place [29]. The model reveal the two reservoirs R1 and R2 have permeability values ranging from hundreds to thousands milliDarcy (K > 100md) across the wells, which is rated very good (Rider [37]). Water saturation model for reservoirs R1 and R2 is shown in Figures 12a and 12b. The water saturation model shows fluid content distribution within the reservoirs for the various wells. The

Model also provides a pictorial view of predicting hydrocarbon saturation within the reservoirs for each well in the field. In Figure 12a, it was observed that the wells are located in areas of low water saturation within reservoir R1 with average water saturation value of 0.384 (38.4%), while in Figure 12b, the wells are also located in regions with low water saturation value which averages at 0.326 (32.6%). This observation implies that hydrocarbon saturation within reservoirs R1 and R2 for the wells averages at 0.616 (61.6%) for R1 and 0.674 (67.4%) for R2. These findings, reveal that the existing wells in the field are located in areas with high hydrocarbon saturation and validates the prolific nature of the wells.

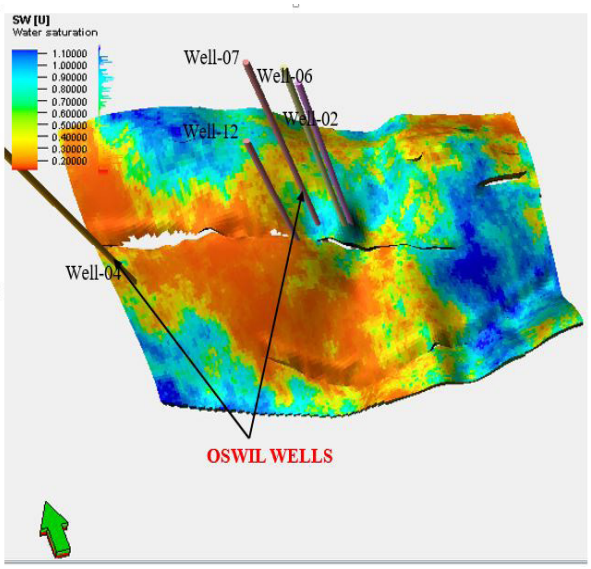

a

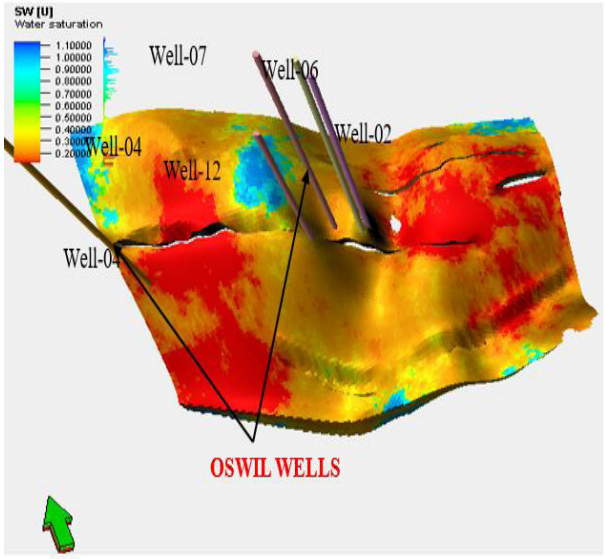

b

Figure 12. (a) Water Saturation Model of Reservoir R1; (b) Water Saturation Model of Reservoir R2

The volume of hydrocarbon in place within the two reservoirs R1 and R2 were estimated and results show that reservoir R1 contains an estimate of 455 × 10^6 STB of hydrocarbon while reservoir R2 contains an estimate 683 × 10^6 STB of hydrocarbon. These findings affirms that the two reservoirs R1 and R2 delineated in OSWIL field are highly prospective.

5. Conclusion

We have employed an integrated methodology which utilizes well log and seismic data to study the structural pattern and petrophysical parameters for hydrocarbon

 DOI: https://doi.org/10.30564/jgr.v3i1.2783

play assessment of OSWIL field. Petrophysical parameters estimated for reservoirs R1 and R2 indicates that the reservoirs have high connectivity and hydrocarbon potential. Time-depth structural maps and petrophysical models produced for reservoirs R1 and R2 indicate a highly faulted reservoir system which aids fluid flow. The structural pattern observed in the field comprises of normal faults which is expected of the Niger Delta Basin. Effective porosity within each well is aided by faulting and this accounts for the high permeability index (K > 100md) observed across the wells in the field. These findings affirm that the two reservoirs R1 and R2 have good hydrocarbon potentials and the trapping mechanism in the field consist of fault assisted closures.

Acknowledgement

We sincerely thank Shell Petroleum Development Company (SPDC) for providing the data used for this study.

Declarations

Funding

No means of financial support was provided for this research from any institution or bank.

Conflicts of interest/Competing interests

We declare that this research work has never been submitted previously by anyone to any journal for peer review and publication, hence it is an original work. All the ethical principles of research in the data collection, preparation, analysis and interpretation were implemented.

Code Availability (Software Used)

PETREL, 2014 Version.

References

[1] Kramers, J.W. Integrated reservoir characterization: from the well to the numerical model. In: proceedings, 14th World Petroleum congress, John Wiley and Sons, 1994.

[2] Nwankwo, C.N., Anyanwu J, Ugwu, S.A. Integration of seismic and well log data for petrophysical modeling of sandstone hydrocarbon reservoir in Niger Delta. Sci Afr, 2014, 13(1): 186-199.

[3] Ibe, A.A., Oyewole, T.E. Hydrocarbon play assessment of X-field in an onshore Niger Delta, Nigeria. Springer Journal of Petroleum Exploration and Production Technology (PEPT), 2018.
DOI: org/10.1007/s13202-018-0497-5

[4] Eze, S.U., Orji, M.O., Nnorom, S.L. Integration of Structural Seismic Interpretation, Stratigraphic and Petrophysical analysis for Hydrocarbon play assessment of "X"-field within the coastal swamp depobelt of Niger Delta: Petroleum Technology Development Journal (PTDJ), 2020, 10(1): 45-67.

[5] Robert S. North Sea petroleum plays. Introduction to Petroleum Exploration for Non geologists. Oxford University Press, 1995: 106.

[6] Schlumberger. Log Interpretation, Principle and application: Schlumberger Wireline and Testing, Houston Texas, 1989: 21-89.

[7] Karbalaali, H, Shadizadeh, S.R., Ali, R. Delineating hydrocarbon bearing zones using Elastic Impedance Inversion. A persian Gulf example. Iranian. J. Oil and Gas science and technology, 2013, 2: 2.

[8] Hansen, T.M., Mosegaard, K, Pedersen, T.R., Uldall, A, Jacobsen, N.L. Attribute guided well-log interpolation applied to low-frequency impedance estimation. Geophysics, 2008: 8-19. R83-R95.10.1190/1.2996302.

[9] Ukaigwe, N.F. A first course in Seismic Exploration, Eddy-Joe publishers. Nigeria Ughelli, Port Harcourt. 2nd ed: 2000: 85-86+367-372.

[10] Eze, S; Orji, OM; Nnorom, SL; Ubogun, K. Model Based Inversion of Acoustic impedance from Seismic trace for Lithofacies Differentiation: An Application in XY Field Offshore Niger Delta. Published in J. of Appl. Sci. Environ. Manage, (JASEM), 2019, 23(9): 1677-1684.

[11] Eshimokhai, S., Akhirevbulu, O.E. Reservoir characterization using seismic and well log data (A case study of Niger Delta). Ethiopian Journal of Environmental Studies and Management (EJESM). 2012, 5(4): 597-773.

[12] Telford, W.M., Geldart, L.P., Sheriff, R. Applied geophysics. Cambridge University press London, 3rd ed, 1990, 1: 769.

[13] Yilmaz, O. Seismic data processing. Society of exploration geophysicists, Tulsa Oklahoma, 2001.

[14] Doust, H., Omatsola E. Niger Delta, in Edwards. J.D, Santogrossi, P.A., eds; Divergent/passive Margin basins; AAPG Memoir, 1990, 45: 239-248.

[15] Reijers, T. Stratigraphy and sedimentology of the Niger Delta. Journal of Geologos, 2011, 17(6):133-162.

[16] Akpoyovbike AA. Tertiary lithostratigraphy of Niger Delta. AAPG Bulletin,1978, 62(2): 295-300.

[17] Orife, J.M., Avbovbo, A.A. Stratigraphic and Unconformity traps in the Niger Delta. 1982.

[18] Obaje, N.G. Geology and Mineral Resources of Nigeria. Lecture Notes in Earth Sciences, Springer-Verlag Berlin Heidelberg, 2009, 120: 109.

DOI: https://doi.org/10.30564/jgr.v3i1.2783

DOI: 10.1007/978-3-540-92685-6

[19] Nadin, P.A., Kusznir, N. J. Palaeocene uplift and Eocene subsidence in the Northern North Sea Basin from 2D forward and reverse stratigraphic modelling. J. of the Geolo. Society, 1995, 152(5): 833-848.

[20] Alao, P.A., Ata, A.I., Nwoke, C.E., Chuo, Y.J., Tzanis, A. Subsurface and Petrophysical studies of Shaly-sand Reservoir targets in Apete field. Niger Delta, Hind. Geophy, 2013, 10: 1155.

[21] Weber, K.J., Daukoru, E.M. Petroleum Geology of the Niger Delta. Proceedings of the 9th World Petroleum Congress, Tokyo. Applied science publishers, Ltd, London, 1975, 2: 202-221.

[22] Ejedawe, J.E. Patterns of incidence of oil reserves in Niger Delta Basin. AAPG Bulletin, 1981, 65: 1574-1585.

[23] Nancy, O.A., Olugbenga, A.E., Dorcas, S.E. Subsurface Mapping and Reservoir Evaluation of Enena Field, Offshore Niger Delta. IOSR Journal of Applied Geology and Geophysics (IOSR-JAGG), 2018, 6(1): 65-73.

[24] Kearey, P., Brooks, M. An Introduction to Geophysical Exploration: Blackwell science Ltd, 2000: 254.

[25] Sheriff, R.E. Limitations on resolution of seismic reflections and geologic detail derivable from them in Seismic Stratigraphy- Applications to Hydrocarbon Exploration (ed. by C. E. Payton). Memoir of the America Association of Petroleum Geologists, Tulsa, 1977, 22.

[26] Sanuade, O.A., Akanji, A.O., Olaojo, A.A., Oyeyemi, K.D. Seismic interpretation and petrophysical evaluation of SH field, Niger Delta. J Petrol Explor Prod Technol 2018, 8,:51-60.

[27] Dresser. A. Log interpretation charts Houston, Texas, Dresser Industries Incorporation, 1979: 107.

[28] Larionov, V.V. Borehole Radiometry: Moscow, U.S.S.R., Nedra, 1969.

[29] Liakopoulos, A.C. Darcy's coefficient of permeability as symmetric tensor of second rank. Hydrological Sciences Journal, 1965, 10(3): 41-48, DOI: 10.1080/02626666509493405

[30] Tixier, M.P. Evaluation of Permeability from Electric log resistivity gradient. Earth Sci. J., 1949, 2: 113.

[31] Xiao, L., Mao, ZhQ, Jin, Y. Calculation of Irreducible Water Saturation (Swirr) from NMR Logs in Tight Gas Sands, Applied Magnetic Resonance, 2012, 42(1):113-125.

[32] Archie, G.E. The electrical resistivity log as an aid in determining some reservoir characteristics. Trans. Am. Inst. Mech. Eng., 1942, 146:54-62.

[33] Okoobo, B. Petrophysical evaluation of Edo field. Unpublished B.Tech project. Federal University of Technology Akure, Ondo State. 2002.

[34] Pyrcz, M.J., Deutsch, C.V. Geostatistical Reservoir Modelling, 2nd ed.. Oxford University Press: Oxford, UK, 2014: 348. ISBN: 9780199731442

[35] Beucher, H., Renard, D. Truncated Gaussian and derived methods. C. R. Geosci., 2016, 348: 510-519.

[36] Amigun, J.O., Odole, O.A. Petrophysical properties evaluation for reservoir characterisation of "SEYI" oil field (Niger-Delta). International Journal of Innovation and Applied Studies, 2003: 756-773.

[37] Rider. The geological interpretation of well logs. 2nd edition, Gulf Publishing Company Houston, 1996: 230.

 DOI: https://doi.org/10.30564/jgr.v3i1.2783

BILINGUAL PUBLISHING CO.
Pioneer of Global Academics Since 1984

Journal of Geological Research
https://ojs.bilpublishing.com/index.php/jgr-a

ARTICLE

Geostatistical Modelling of Reservoir Quality Over "Bright" Field, Niger Delta

Abe, S.J* Olowokere, M. T Enikanselu, P. A

Department of Applied Geophysics, Federal University of Technology, Akure, Nigeria

ARTICLE INFO

Article history
Received: 14 January 2021
Accepted: 26 January 2021
Published Online: 31 January 2021

Keywords:
Probabilistic
Lp norm
Modelling
Gaussian
Stochastic

ABSTRACT

The quality of any hydrocarbon-bearing reservoir is vital for a successful exploitation work.. The reservoir quality is a function of its petrophysical parameters. Hence the need to model these properties geostatistically in order to determine the quality away from well locations.Composite logs for four wells and 3-D seismic data were used for the analysis. A reservoir named Sand X was mapped and correlated across wells 1 through 4. The four reservoir quality indicators - Effective porosity, permeability, volume of shale and net-to-gross- were estimated and modelled across the field. Sequential Gaussian simulation algorithm was employed to distribute these properties stochastically away from well locations and five realizations were generated. The volume of shale varied from 0.025 (Well 1, second realization) to 0.18(Well 2, first realization). The net-to-gross varied from 0.81 to 0.96 in wells 3 and 4 respectively, for the third realization, while the effective porosity varied from 0.125 to 0.295 for the fifth realization in Wells 3 and 4 respectively. The permeability is above 5000mD at all the existing well locations.These realizations were ranked using Lp norm statistical tool to pick the best for further evaluation. The reservoir quality deduced from the analyzed indicators was favourably high across the reservoir.The application of geostatistics has laterally enhanced the log data resolution away from established well locations.

1. Introduction

The quality of a reservoir is defined by its hydrocarbon storage capacity and deliverability. The hydrocarbon storage capacity is characterized by the effective porosity and the geometry of the reservoir, whereas the deliverability is a function of the permeability as well as the effective porosity or the volume percentage of interconnected pores in a rock. The remaining space in the rock is occupied by the framework or matrix of the rock and, if present, unconnected pore space.

Due to limited understanding of the details of many diagenetic processes, there is a lack of new techniques and tools to support reservoir quality predictions. Despite its notable economic importance, relatively few papers illustrate research in reservoir quality prediction. The main difficulty to execute this task is that the creation of models to reservoir quality prediction is highly dependent on quality and availability of calibration datasets [1,2]. Biased datasets will generate poor models. Furthermore, lack of observations combined to a high amount of features describing each observation can become more difficult, or even prohibitive, to fit a multivariate model to forecast

**Corresponding Author:*
Abe, S.J,
Department of Applied Geophysics, Federal University of Technology, Akure, Nigeria;
Email: jsabe@futa.edu.ng

DOI: https://doi.org/10.30564/jgr.v3i1.2805

reservoir quality. This problem is known as curse of dimensionality [3].

Regression analysis is the most commonly used technique to predict reservoir quality [4-6]. However, this technique has limitations and demands intense interaction with domain experts. Moreover, such models are sensitive to the limits imposed by the calibration dataset. Recently, soft computing techniques have been used in reservoir characterization and modeling [7]. Among these techniques, Artificial Neural Networks (ANNs) have been used to identify relationships between permeability, measured logs and core data [8].

In this paper, we propose the use of the stochastic modelling technique to predict reservoir quality indicators at and away from well locations. This enables more precise definition of reservoir geometry, prediction and evaluation of reservoir quality in and away from well locations and the eventual ranking of these realizations.

2. Location and Geology of the Study Area

The field is located within the Niger delta (Figure 1). The base map showed the location of the four wells and the seismic lines.

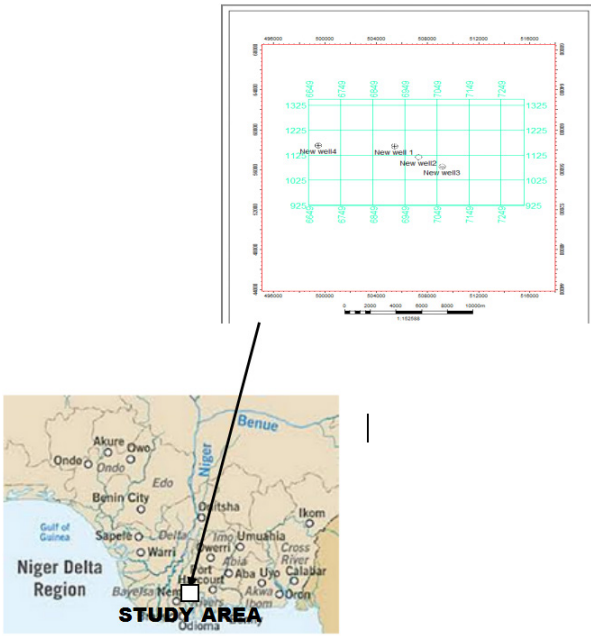

Figure 1. Map of Niger Delta showing the Study Area and Base Map

The Niger Delta basin is located on the continental margin of the Gulf of Guinea in equatorial West Africa and lies between latitudes 4° and 7°N and longitudes 3° E [9]. It ranks among the worlds' most prolific petroleum producing Tertiary deltas that together account for about 5% of the worlds' oil and gas reserves. It is one of the economically prominent sedimentary basins in West Africa and the largest in Africa [10]. Three lithostratigraphic units have been recognized in the subsurface of the Niger Delta [11-13]. These are, from the oldest to the youngest, the Akata, Agbada and Benin Formations. The Akata Formation (Eocene - Recent) is a marine sedimentary succession that is laid in front of the advancing delta and ranges from 1,968ft to 19,680ft (600-6,000m) in thickness. It consists of mainly uniform undercompacted shales with lenses of sandstone of abnormally high pressure at the top [13]. The shales are rich in both planktonic and benthonic foraminifera and were deposited in shallow to deep marine environment[11]. The Agbada Formation (Eocene-Recent) is characterized by paralic interbedded sandstone and shale with a thickness of over 3,049m [10]. The top of Agbada Formation is defined as the first occurrence of shale with marine fauna that coincides with the base of the continental-transitional lithofacies [14]. The base is a significant sandstone body that coincides with the top of the Akata Formation [11]. Some shales of the Agbada Formation were thought to be the source rocks, however; [15] deduced that the main source rocks of the Niger Delta are the shales of the Akata Formation.

The Benin Formation is the youngest lithostratigraphic unit in the Niger Delta. It is Miocene - Recent in age with a minimum thickness of more than 6,000 ft (1,829m) and made up of continental sands and sandstones (>90%) with few shale intercalations. The sands and sandstones are coarse grained, subangular to well rounded and are very poorly sorted.

3. Methodology

The flow chart used for the data analysis is as shown below in Figure 2.

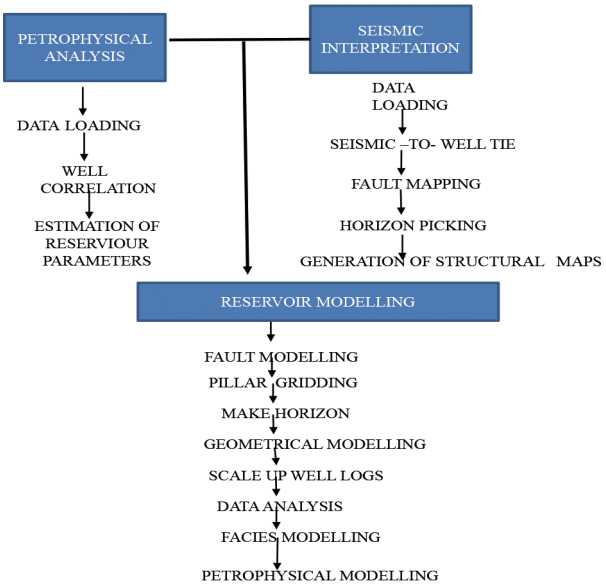

Figure 2. Flow Chart used for Data Analysis

 DOI: https://doi.org/10.30564/jgr.v3i1.2805

Geostatistical Modelling

3.1 Variogram Analysis

A variogram was used as input when discrete property was populated using a stochastic algorithm. The mathematical definition of the variogram is:

$$(h) = \frac{1}{2m}\sum_{i=1}^{m}[(x_i) - Z(x_i + h)]^2 \quad (1)$$

where m is the number of pairs of sample points of observations of the values of attribute Z separated by distance (lag) h.

A normal score (Gaussian) transformation was applied to the upscaled logs to normalise the data prior to variogram analysis. This was done so that the variables will achieve stationarity. This means that statistical properties do not depend on exact positions [18]. Spherical and Gaussian models were applied to the variograms. The variogram analyses were carried out for all the zones in three directions. The major direction is Northwest-Southeast (NW-SE) being the trend of the rollover structure in the study area. The minor direction (Northeast-Southwest, NE-SW) is perpendicular to the major direction while the vertical direction conforms to depth.

Generally the Steps Involved in Populating Data Away from Well Bore Involves:

(1) Carrying out variogram analysis for the 4 wells which involves: calculating experimental variogram (average of the squared difference between nodes (point pairs) to obtain a single value of variance for that specific "lag distance". The plot of the variance and the lag distance produced the experimental variogram

(2) Fitting a curve (Spherical, Exponential, Gaussian) along the experimental variogram to get Model Variogram to obtain the (Nugget, Sill, Range)

(3) Krigging of the available property values to obtain a value for the unknown point

(4) Plotting of cumulative frequency curve (Ogive) where different percentile values will give rise to different realizations (iterations) for the same surface.

3.2 Ranking of Realizations

The five realizations of the properties modelled were ranked in other to choose the realization that is close to the control values using a statistical tool called Lp norm using the second order which is the least square method.

This method averages the deviation from the true value and estimate the error. The realization with the least error is taking as the best which can be used for further analysis. The expression is as stated below.

$$L_p norm = \sum_{n=1}^{\infty}\frac{(d_{true} - d_{realization})^2}{n} \quad (2)$$

4. Results and Discussion

Figure 3 depicts variation in thickness of Sand X across the four wells. Table 1 reveals that it is thickest in Well 4 (73.2 m) and thinnest in Well 1 (13,3 m). Also, the sand body is cleanest in Well 4 (Vsh = 0.09) and dirtiest in well (Vsh = 0.4). These are further supported by the observed relative sand-shaleproportion in these wells. The deep resistivity log readings are high across the wells, indicating that they are all hydrocarbon-bearing. The thick column of shale overlying and underlying the sand, serves as good seal.

The net thickness, which is the amount of sand within Sand 2 ranges from 11.77m to 60.64m while, the net pay thickness has a range of 5.44m to 43.36m and these initial values gave high net to gross range for Sand 2 to be from 0.78 to 0.89.

The porosity and permeability values ranged from 0.20 to 0.32 and 1000mD and 3122mD respectively. Due to the high net- to- gross values, we have corresponding low volume of shale values ranging from 0.09 to 0.40. Sand X is hydrocarbon bearing in all the wells because of the low water saturation and high hydrocarbon saturation values.

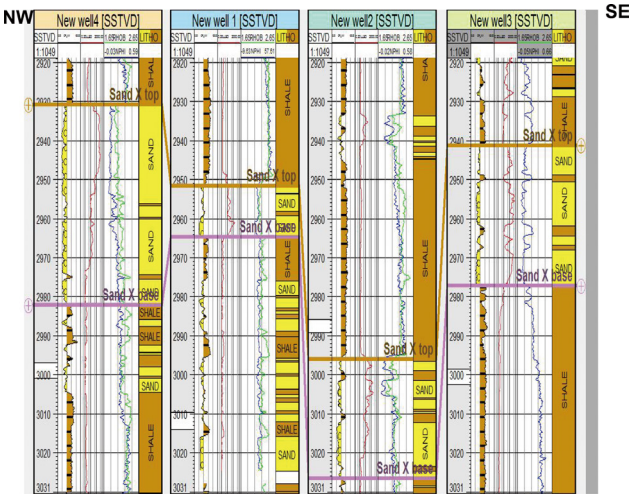

Figure 3. Well Correlation Panel showing the Top and Base of Sand X

Table 1. Petrophysical Parameters for Sand X

SAND 2	Gross (m)	Net (m)	Net Pay (m)	N/G	Ø	K (mD)	V_{sh}	S_w	S_h
WELL 1	13.27	11.77	5.44	0.89	0.23	1452	0.09	0.31	0.69
WELL 2	30.63	23.90	20.59	0.78	0.32	3122	0.15	0.38	0.62
WELL 3	35.81	30.79	30.79	0.86	0.20	1000	0.21	0.43	0.57
WELL 4	73.19	60.64	43.36	0.86	0.25	2883	0.40	0.20	0.80

DOI: https://doi.org/10.30564/jgr.v3i1.2805

4.1 Seismic Interpretation

Seimic data was interpreted in order to unravel the underlying geology that gave rise to observable reflections. Seismic-to-well tie ,Figure 4, was carried out to ensure correct horizon mapping. The time structural map of the top of Sand X, Figure 5, with a TWT range of around 2820ms to 3320ms and a contour interval of 30ms. There is a structural high from the central to the nothern part of the field, and another small closure on it; justifying the probable location of the wells.

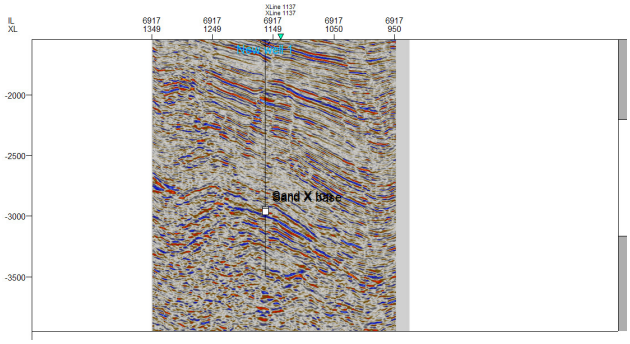

Figure 4. Seismic-to-Well tie shown on inline 6917

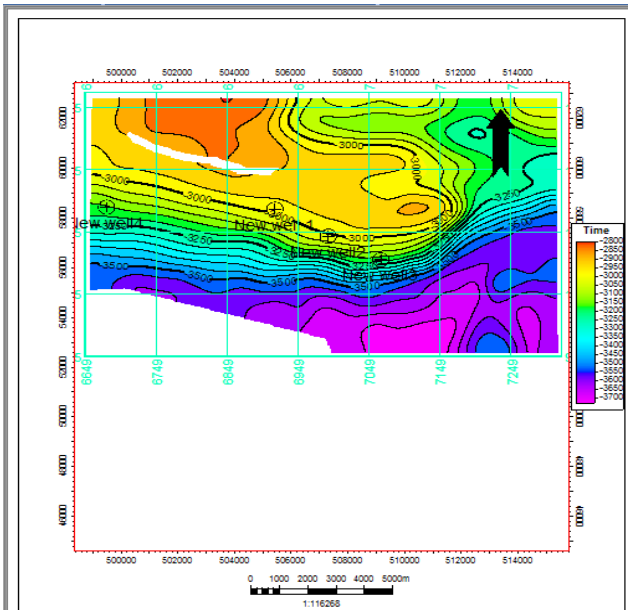

Figure 5. Time Structural Map of Top of Sand X

4.2 Reservoir Modelling

4.2.1 Volume of Shale Model for Sand X

Thus far, reservoir quality information has been very sparse; available only at well locations. The Geostatistical reservoir modelling exercise facilitated wider distribution of the computed reservoir quality indicators away from these well locations. Prior to the modelling, variogram analysis was done and the nugget and sill values were close to 0 and 1 respectively. The first realization of volume of shale model in Sand X (Figure 6) shows the variation of the property across the field. The low volume of shale at and around the well locations lend further credence to the presence hydrocarbon as well as high reservoir quality. The volume of shale values at the location of Wells 4 and 1 are lower than those of the remaining two wells. High volumes of shale values are present at the central, southwestern and southeastern parts of the field.

The second realization in Figure 7 shows a distribution different from the first realization with low volume of shale values at the western, central to the northern parts. A higher volume of shale could be observed around the south-eastern flank of the field. This connotes higher presence of shale anda resultant reduction in reservoir quality. Figure 8 shows the third realization with low volume of shale values at the existing well locations and high volume of shale values scattered around them.

In the fourth realization shown in Figure 9, there is a lit bit high volume of shale value around Well 4 and other well locations, however there are clusters of low volume of shale values around them. In the fifth realization (Figure 10), there are high volume of shale at the edge of the western part and clusters of low volume of shale values at the northeastern and toward the western portion.

Based on the statistical ranking, equation 2, and Table 2, the first realization is adjudged best of the five. It contains the least error and therefore of best reservoir quality.

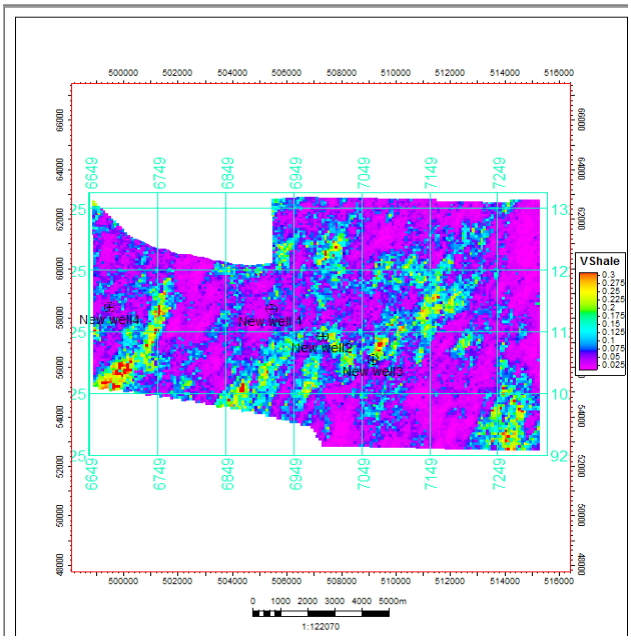

Figure 6. Model of Volume of Shale Distribution in Sand X (1st Realization)

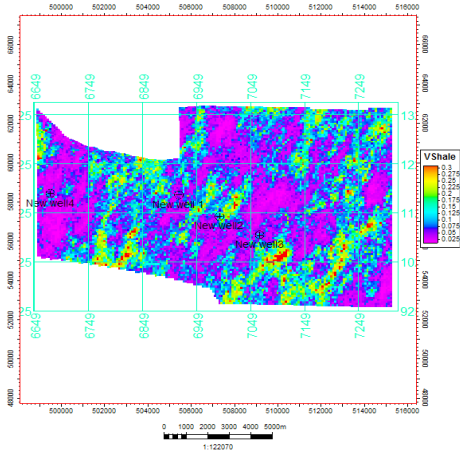

Figure 7. Model of V. Shale distribution in Sand X (2nd Realization)

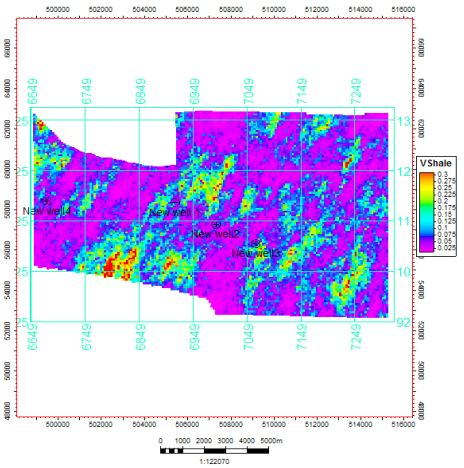

Figure 8. Model of V. Shale distribution in Sand X (3rd Realization)

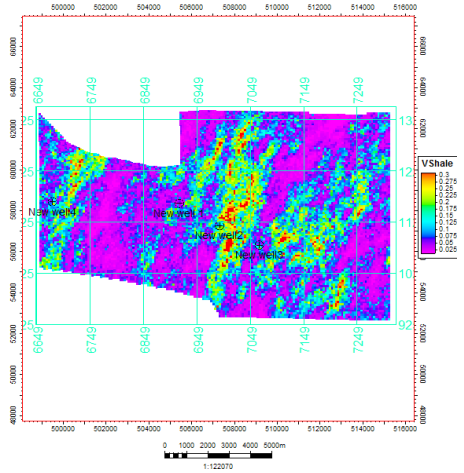

Figure 9. Model of V. Shale distribution in Sand X (4th Realization)

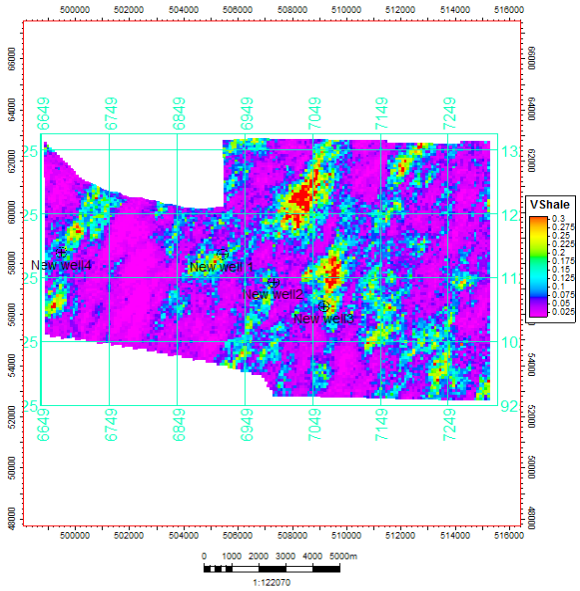

Figure 10. Model of V. Shale distribution in Sand X (5th Realization)

Table 2. Volume of Shale Values at Well Locations for the 5 Realizations and the Control

VSHF2	WELL 1	WELL2	WELL3	WELL4
1st Realization	**0.05**	**0.18**	**0.1**	**0.03**
2nd Realization	0.025	0.075	0.15	0.035
3rdRealization	0.07	0.045	0.12	0.056
4thRealization	0.041	0.12	0.175	0.053
5thRealization	0.05	0.08	0.095	0.057
CONTROL	**0.09**	**0.15**	**0.21**	**0.40**

Similarly, Figures 11 and 12 showed the best of the five realizations for the net-to-gross, effective porosity respectively. The permeability model, Figure 14 was distributed using a crossplot of permeability against porosity Figure 13.

4.2.2 Net to Gross Model for Sand X

The best realization for net-to-gross model was observed at fourth realization. At all the well locations, Figure 10, very high values of net-to-gross were observed.

The model showed the highest net -to -gross value in Well 1 (0.92) and lowest in Well 3 (0.82) with clusters of high net -to- gross values exist toward the western and eastern part of the field, and low net to gross values exist around Wells 1 and 2. These high values depict low level of shale in the reservoir; which favours high reservoir quality.

Table 3 contains the numerical values extracted from

DOI: https://doi.org/10.30564/jgr.v3i1.2805

the well locations for the five realizations and the values are favourably okay for a good reservoir with the fourth realization values close to that of the control.

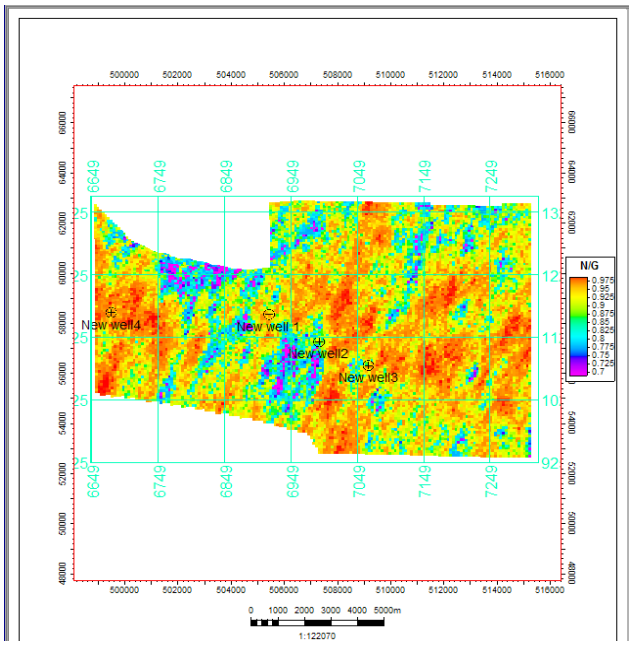

Figure 11. Model of N/G distribution in Sand X (4th Realization)

Table 3. Net to Gross Values at Well Locations for the 5 Realizations and the Control

NTG2	WELL 1	WELL2	WELL3	WELL4
1st Realization	0.92	0.83	0.85	0.95
2nd Realization	0.94	0.87	0.83	0.94
3rdRealization	0.93	0.89	0.81	0.96
4thRealization	**0.92**	**0.86**	**0.82**	**0.89**
5thRealization	0.86	0.84	0.91	0.93
CONTROL	**0.89**	**0.78**	**0.86**	**0.86**

4.2.3 Effective Porosity Model for Sand X

The best realization of effective porosity model is shown in Figure 12. The effective porosity values varied from Well 4 (29%) to 15% in Well 3. There are packets of low effective porosity values at the northern part and around Wells 1 which spreads to Well 3 location. The Western and South-eastern flanks of the reservoir exhibit high effective porosity , which supports the net-to-gross revelations. Again, the reservoir quality is adjudged reasonably acceptable across the reservoir. The numerical values extracted from the well locations for the five realizations are shown in Table 4 and the first realization with a range of 0.14 to 0.29 is close to the control values. High effective porosity values are expected for a good hydrocarbon bearing reservoir.

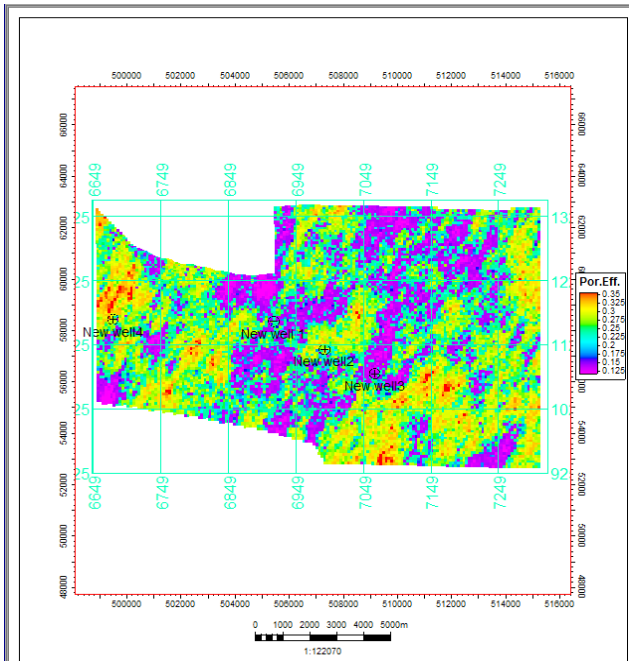

Figure 12. Model of PHIE Distribution in Sand X (1st Realization)

Table 4. Effective Porosity Values at Well Locations for the 5 Realizations and the Control

Eff. Por.2	WELL 1	WELL2	WELL3	WELL4
1st Realization	**0.25**	**0.27**	**0.14**	**0.29**
2nd Realization	0.23	0.26	0.15	0.32
3rdRealization	0.275	0.27	0.12	0.33
4thRealization	0.26	0.22	0.13	0.28
5thRealization	0.25	0.26	0.125	0.295
CONTROL	**0.23**	**0.32**	**0.20**	**0.25**

4.2.4 Permeability Model for Sand X

There exist strong relationship between permeability and porosity[17,18] . Consequently a crossplot of permeability and porosity, Figure 13, was generated values to deduce this relationship for Sand X. The relationship is as shown in equation 3

$$K = 57821.9 * Ø - 9990.7 \quad (3)$$

Where K is the permeability and **Ø** is the porosity, an increase in porosity produces a corresponding increase in permeability.

This equation was then used with the initial porosity model, Figure 12, to generate the permeability model in Figure 14. It shows the variation in permeability across the field. Expectedly, high permeability values were ob-

DOI: https://doi.org/10.30564/jgr.v3i1.2805

served in and around Wells 4, 1 and 2, while a relatively low was observed around Well 3. This reasonably reflects the findings of the effective porosity model affirming high quality of the reservoirThere are clusters of high permeability values at the western, central and southern parts of the model.

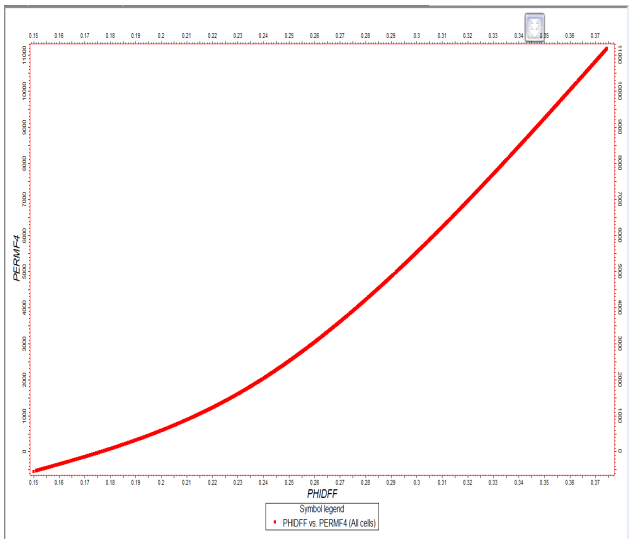

Figure 13. Crossplot of Permeability and Total Porosity

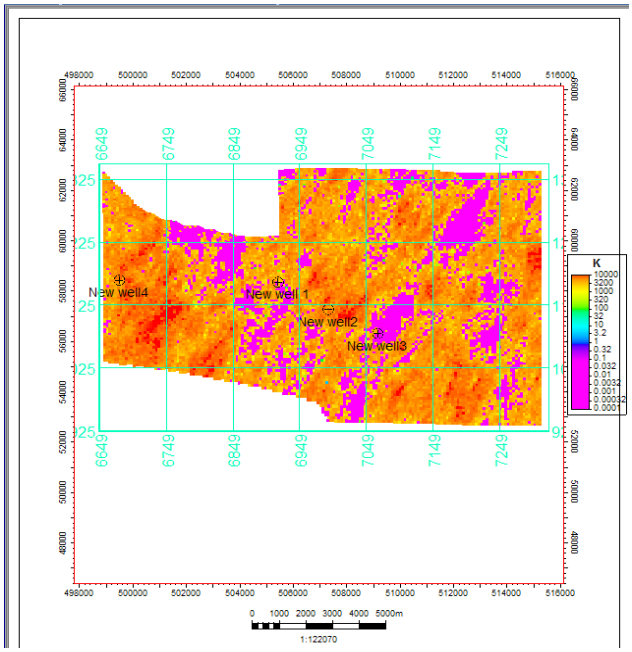

Figure 14. Model of Permeability distribution in Sand X

5. Conclusion

The study has employed surface seismic and well data to determine the reservoir quality at the well locations and geostatistically away from them.The reservoir quality indicators that were modelled stochastically showed variation in the distribution of volume of shale, effective porosity, net to gross and permeability within the field. At the existing well locations the reservoir quality were good based on the values. Away from well bore, for some realizations, the reservoir quality improves while it decreased in others. Regions beyond the existing well locations with good property values are good targets for hydrocarbon exploitation. The one realization for the permeability model also displayed variation in permeability across the field. Areas with high effective porosity, low volume of shale, high net to gross and high permeability are deemed to be of good quality which could further be explored.

References

[1] Kupecz, J.; Gluyas J., Block, S. Reservoir quality prediction in sandstones and carbonates: An Overview. In: Kupecz J., GluyasJ. and Block S. (Eds). Reservoir quality prediction in sandstones and carbonates, AAPG Memoir 69, 1997.

[2] Fanchi, J. R. Principles of Applied Reservoir Simulation. 2nd ed., MA, USA, Elsevier Burlington, 2001.

[3] Bellman, R., Dreyfuss, S. Applied Dynamic Programming. Princeton, USA, Princeton University Press, 1962.

[4] International energy agency. World energy outlook, 2007

[5] Love, K. M., Strohmenger, C., Woronow, A., Rockenbauch, K. Predicting Reservoir Quality Using Linear Regression Models and Neural Networks. 1997.

[6] Bloch, S. Empirical predictions of porosity and permeability in sandstones. AAPG Bulletin, 1991, 75: 1145-1160.

[7] Nikravesh, M., Aminzadeh, F., Zadeh, L. A. Soft computing and intelligent data analysis in oil exploration. Ney York, USA, Elsevier, 2003.

[8] Ligtenbert, J. H., Wansink, A. G. Neural Network Prediction of permeability in the El Garia Formation, Ashtart Oilfield, Offshore Tunisia. In: Nikravesh M., Aminzadeh F., Zadeh, L.A (Eds). Developments in Petroleum Science, 2003, 51: 397-411.

[9] Whiteman, A. Nigeria: Its petroleum geology, resources and potential: London. Graham and Trotman,1982; 381 .

[10] Reijers TJF. Selected Chapters on Geology, SPDC of Nigeria, Corporate Reprographic Services, Warri., 1996, 197.

[11] Short KC, Stauble, J. Outline geology of the Niger Delta. AAPG. 1967, Bull 5: 761-779

[12] Frankl, E.J., Cordy, E.A. The Niger Delta Oil Province Recent Development Onshore and Offshore, 7thWorld Petroleum Congress Proceedings, Mexico

DOI: https://doi.org/10.30564/jgr.v3i1.2805

City, IB, 1967: 195-209.

[13] Avbovbo, A. A., Tertiary lithostratigraphy of Niger Delta: American Association of Petroleum Geologists Bulletin, 1978, 62: 295-300.

[14] Adesida A, Ehirim, BO. Cenozoic Niger Delta: A guide to its lithosedimentary analysis. SPDC Exploration note 88.002 (Ref: on-shore wells), 1988, 1-10.

[15] Ejedawe, J.E., S.J.L.Coker, D.O. Lambert-Aikhionbare, K.B. Alofe, F.O. Adoh. Evolution of Oil Generating Window and Gas Occurrence in Tertiary Niger Delta Basin. AAPG Bull, 1984, 68: 1744-1751.

[16] Deutsch, C.V. Geostatistical Reservoir Modeling. Oxford University Press, 2002: 376.

[17] Etu-Efeotor, J.O. Fundamentals of petroleum geology. Paragraphic publications, Port Harcourt, Nigeria, 1997, 135.

[18] Adeoti, L., Njoku, O., Olawale, O., Fatoba, J., Musa, B. Static Reservoir Modelling using Well Log and 3-D Seismic Data in a KN Field, Offshore Niger Delta, Nigeria. International Journal of Geoscience, 2014, 5: 99-106.

 DOI: https://doi.org/10.30564/jgr.v3i1.2805

BILINGUAL PUBLISHING CO.
Pioneer of Global Academics Since 1984

Journal of Geological Research
https://ojs.bilpublishing.com/index.php/jgr-a

ARTICLE

Petrographic Study of Sedimentary Iron Ore in Shendi-Atbara Basin, River Nile State, Sudan

Abubaker A.M.A. Abasher[1] Sadam H.M.A.Eltayib[1*] El Sheikh M. Abdelrahman[2] Mohammed M.A.Amlas[1]

1.Intrenational University of Africa, Department of Economic Geology Faculty of Minerals and Petroleum-Khartoum, Sudan.
2.Al Neelain University Department of Mineral Resources, Faculty of Petroleum and Minerals, Khartoum, Sudan.

ARTICLE INFO

Article history
Received: 18 January 2021
Accepted: 24 February 2021
Published Online: 31 March 2021

Keywords:
Petrographic
Iron ore
Shendi formation
Conformable
Textures

ABSTRACT

This paper presents the results of petrographic study of sedimentary iron ore from surface strata of the Shendi-Atbara Basin, River Nile State, Sudan. The aims of this study are to investigate the geological behavior and geological conditions affecting precipitation of sedimentary iron ore. The methodologies have been used to realize the objectives of this study include field work, office work and laboratory work including thin sections and polished sections analysis. According to field observation sedimentary iron ore can broadly be considered as occurring in three major classes: Ferribands iron, ferricrete iron and oolitic iron ores. The modes of occurrence of iron ore were described at the outcrops and vertical sedimentary profiles revealed that the iron occurred in the study area at different types in stratigraphic sequence such as cap, bedded and interbedded conformable with Shendi Formation. Petrographic study of iron ore in collected samples using polarized microscope and ore microscope includes study of the textures and structures of ores to obtain ore history. The main types of textures and structures in studied samples are oolitic, granular, lamellar and bands. According to these results the origin of iron ore is formed by chemical precipitation during chemical weathering of surrounding areas in continental lacustrine environment. The iron ore in study area is potential for future mining works and steel industry.

1. Introduction

The study area is located in the eastern part of the River Nile State of northern Sudan between Latitudes 17°20'0" and 16°40'0" N and longitudes 33°30'0" and 34°10'0"E (Figure 1). The distance from Khartoum to the study area is about 180 Km, and can be reached by a paved road, passing through Shendi, to Atbara, following the River Nile on the eastern bank. The study area is characterized by physiographic features varying from hilly terrains as in Al Musawarat, Umm Ali and Al Bagraweya areas. In between there are lots of areas crossed by valleys such as Wadi Al Sawad, Wadi Al Hawad and Wadi Al Awatib, all of which are seasonal streams. The area is characterized by generally low relief topography with scattered stratified flat topped hills.

**Corresponding Author:*
Sadam H.M.A.Eltayib,
Intrenational University of Africa, Department of Economic Geology Faculty of Minerals and Petroleum-Khartoum, Sudan;
Email: sadam_h3@yahoo.com

DOI: https://doi.org/10.30564/jgr.v3i1.2814

There is negative relief (valleys) caused by differential erosion. The area is dominated by arid climate conditions with a hot summer season extending from March to August with temperature reaching above 45°C during the day. The average temperature is about 35°C. The rainy season is extending from July to September with less than 200 mm per year rainfall. The winter season is from November to February and the temperature drops to less than 20°C. The area is poor in vegetation, which includes Acacia trees and short grasses along the seasonal valleys. There are date palm trees along the River Nile in addition to some other crops in the terraces of the River Nile. The area is dominated by parallel to dendritic seasonal streams flow in sedimentary rocks and seems to be structurally controlled. The main direction of these streams is to the W and NW, towards the river Nile [1]. Iron is estimated to make up 32.07% of the Earth's mass and its elemental abundance varies between about 5% of the Earth's crust and as much as 80% of the planet's core. It is therefore not surprising that there are a number of commonly occurring iron minerals and many iron ore deposits found at the surface of the earth. Suggested that just one of the iron-enrichment deposits types alone, derived from iron formations, represents the largest and most concentrated accumulation of any single metalliferous element in the Earth's crust. The term "iron ore" is used here as an economic term to refer to iron-bearing deposits and products that have been, are being, or could be expected to be exploited economically for their iron content. Any uneconomic iron accumulations are simply referred to as iron mineralization. The sedimentary iron ore is one of the largest deposit in the Sudan, and its reserve is estimated at 1351 million cubic meters at 30%Fe average grade. It is found in many occurrence modes; multiple layering in plateau and mesas, due to repeated sedimentary cycles, ore and sediments intercalated allochthons at meanderings, inselbergs, compacted boulders and massive biogenic ooze.

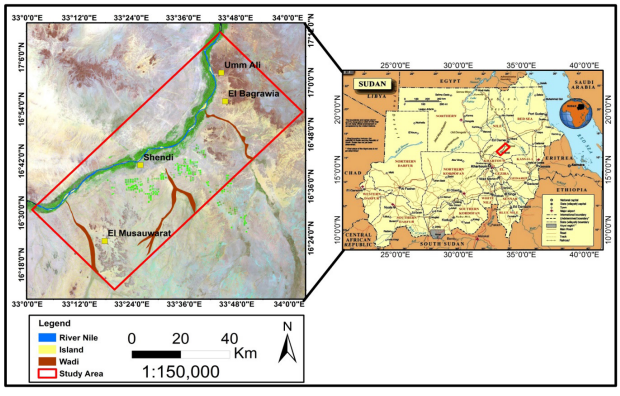

Figure 1. Location map of the study area

2. Geology of the Study Area

The main geological units are composed of Basement Complex (Pre-Cambrian), Upper Cretaceous Sedimentary Formation (Nubian sandstone), Hudi Chert (Oligocene) and Quaternary superficial deposit (Figure 2) in ascending chronological order [2].The stratigraphic sequence has been established as follows:

2.1 Basement Complex

Basement complex includes Igneous, Metamorphic & Metasedimentary rocks that overlain by Palaeozoic or Mesozoic sedimentary or igneous rock and they are mainly of Pre-Cambrian age [2, 3]. A good example is the Sabaloka Ring Complex that appeared to be of Cambrian age according to [4] the oldest rocks exposed in the central Sudan include an ancient group of crystalline gneiss and schist, metamorphic rocks and granites [5]. Representatives of this unit crop out in four places namely, in the sabaloka inlier north of the capital, west of the White Nile between Omdurman and Ed Dueim, east of the blue Nile in the parts of the Butana plains and south of the Gezira between Sennar and Kosti, elsewhere younger deposits cover them (Figure 2).

2.2 Shendi Formation (Upper Cretaceous Sandstone)

Kheiralla, M. K.[6] introduces the name quartzose sandstone to describe siliciclastic sedimentary rocks cropping out in Shendi area. These are well bedded, non-pebbly, clean, well sorted sandstone which contain ripple marks, rib and furrow structures. The sandstone contains mainly of quartz coated with iron oxide with interstices filled with ferruginous matter. A formal lithostratigraphic nomenclature of the units was given by [2] who proposed the name Shendi formation whose type locality is represented by outcrops north east of kabushiya village, River Nile state. The lithological evidence, from shallow borehole and the kandaka-1 well permits a downward extension of Shendi formation to include the mud-dominated lithofacies mainly identified. Consequently, the Shendi formation has been formally subdivided into two members: the umm Ali member and the Kabushiya member. The former, was mainly identified from boreholes with its type section located approximately 100m south of Umm Ali village. The type section previously selected to describe Shendi Formation [2] has been retained for the Kabushiya member. Lacustrine to fluvial-lacustrine condition could have prevailed during deposition of the Umm Ali member, while fluvial-dominated setting characterizes the Kabushiya member. Ter-

DOI: https://doi.org/10.30564/jgr.v3i1.2814

restrial palynomorph of Campanian - maastrichian age were reported with the subsurface part of unit represented by Kabushiya member and the upper most part of the Umm Ali Member (Figure 2).

2.3 Hudi Chert (Tertiary Sediments)

The represents in hudi chert which composed of sub-rounded boulders, yellowish brown in color, which range in size from 5 to 20 cm. The rocks are very hard and fossiliferous with Gastropods fossils. The hudi chert was first identified by [7] from hudi railway station about 40 km NE of Atbara and later studied by [8, 9, 2]. The hudi chert rocks were regarded as lacustrine chalky deposits that have been silicified into chert [8]. The source of silica was probably from silica flow from the young volcanic activity of Jebel Umm-Marafieb of NW Berber. [7] Reported that the hudi chert is an upper Eocene/lower Oligocene Formation, which contains some types of fossils such as Gastropods and plant fossils. The sediments of Jebel Nakhara Formation represent part of the Nubian Sandstone Formation Hills from Shendi-Atbara region [6]. These rocks of Jebel Nakhara Formation are exposed west of the River Nile between the Cenozoic volcanic and the Nile. The Jebel Nakhara Formation mainly comprises sandstones with varying grain size, siltstones, mudstones and conglomerates. They overlie the basement discordantly and in turn covered uncomformably by Cenozoic volcanic. They are poorly sorted, coarse to medium-grained in texture and mainly consist of quartz and some clay minerals as the main components. Trough cross bedding, tabular cross bedding and graded bedding structures are common sedimentary structures. There is a general agreement that these sediments have been deposited mainly in Tertiary time [6] while [2] suggested a Cretaceous age to the same sediments (Figure 2).

2.4 Cenozoic Volcanic

First descriptions of these volcanic were given by [9, 10] described them in more detail and related them to Tertiary-Quaternary volcanic activity[11, 12] suggested a late Pliocene to Recent ages for the younger Bayuda volcanic rocks based on the slight degree of erosion. In Bayuda the lava flows cover both the Precambrian basement and the Tertiary Sandstone Formation. The outcrop is faulted in the eastern side of Jebel Nakhara, thus showing the unconformity relationship with the underlying sandstone. Their extrusion is connected with post-Nubian N-S and E-W striking faults [13]. They are assumed to be NW extensions of the great East African Rift System (Figure 2).

2.5 Superficial Deposits

The superficial deposits include wadies and galley deposits which course the Jebels. Recent fan deposits that emerged from the out crops and consist of poorly sorted sediments redeposit from pre-existing sedimentary boulders, fragments and leached coarse and fine sediments. North to Shendi area numerous mobile sediments consist of well sorted medium to fine sand, are covering the underlying Shendi formation and extend to the east and north east to the river Atbara boundary. The superficial deposits in Buttana include the clayey soil covering the flat plains, in addition to the valley fill and the deltaic deposits which are seasonally transported by the ephemeral streams during the rainy season. The valley deposits cover the drainage beds and are mainly composed of sands and pebbles. The superficial deposits in Bayuda include gravels, sands, clays, sandy clays and silt. The alluvial deposits are very thick around the River banks consisting mainly of dark clays and clayey silt with fined-grained sands used for Cultivation. The Wadi alluvial consists of fined to medium-grained sands, which form the middle and lower courses of the Wadis, while the upper parts are covered with unconsolidated coarse sand and fine gravels. Superficial deposits in Sabaloka include Nile silts, alluvial fans, Aeolian sands and lag gravels, sandy residual soils [14] (Figure 2).

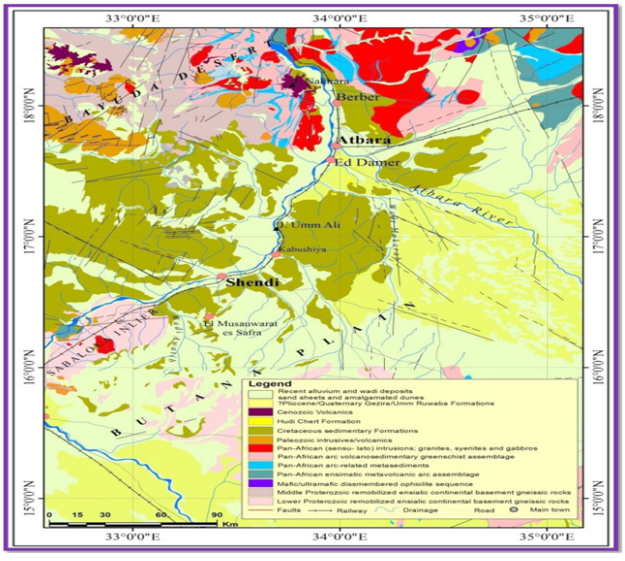

Figure 2. Geological map of the study area

3. Objectives of This Study

The main objectives of this study are:

•Investigate the geological behavior of the iron ore in the study area.

•Investigate the modes of occurrence of iron ore in the

DOI: https://doi.org/10.30564/jgr.v3i1.2814

out crops.

•To study the Textures and structures of ore deposits to obtain ore's history.

•Determine the origin and gneiss of iron ore in the study area.

•Determine the potentiality of iron ore to industrial uses.

4. Methodology

Eleven representive samples were taken during field work from the surface strata of the Shendi -Atbara Basin have been analyzed in this study. Occurrence of iron ore was described at the outcrops and representative rock samples were collected from each of the 12 localities. Thin sections from various samples were prepared, partly at the laboratories of Al Neelain University and partly at Central Petroleum Laboratories (CPL) in Khartoum. They have been studied under the polarized microscope to determine the mineralogical composition, textural and microstructural characteristics. Similarly, polished sections from iron ore deposit were made and examined using ore microscope. The mineral paragenesis, textures and structures of the ores have been studied at the laboratories of Khartoum University.

5. Results and Discussion

The geological and structural setting of the iron ores bearing areas evaluation of the available information. In study area, several types of iron accumulations occur in a widespread distribution within and on top of the sediments of the Nubian formation in an area of approximately 50km in diameter between the cities of Shandi, Kabushia and Atbara. The iron stone beds attain a maximum thickness of approximately one meter (Figure 3). They occur within fluvial sediments on the Shandi formation. The Shandi-Kabushia region lies within the Atbara rift system, an asymmetric half-garben structure which is characterized by locally high subsidence rate as indicated by the maximum depth of the basin of approximately 3100m. The structural control of sedimentation is indicated by the lateral facies association. The outcropping sediments seem to be deposited in the sag-phase of the graben development. The fining upwards sequences begin with the erosional surfaces pass upwards into trough and tabular cross-bedded sandstone and finally into ripple cross-bedded or laminated fine grained sand. Deposits of oolitic ironstones occur mostly on top of bioturbated fine grained sediments. Within this meandering river environment also extensive flood plain sediments occur with this meandering river environment also extensive flood plain sediments occur which yield lens-shaped deposits of kaolin (Figure 3). The (Nubian strata) belong to the upper-most cretaceous to tertiary cycle of a sequence of three mega-cycle. Most of the strata studied consist of clastics deposited mainly in alluvial environment. Facies and thickness of the sediments strongly depend on the structural evolution which is late-Jurassic to early cretaceous time (Figure 3, 4, 5, 6).

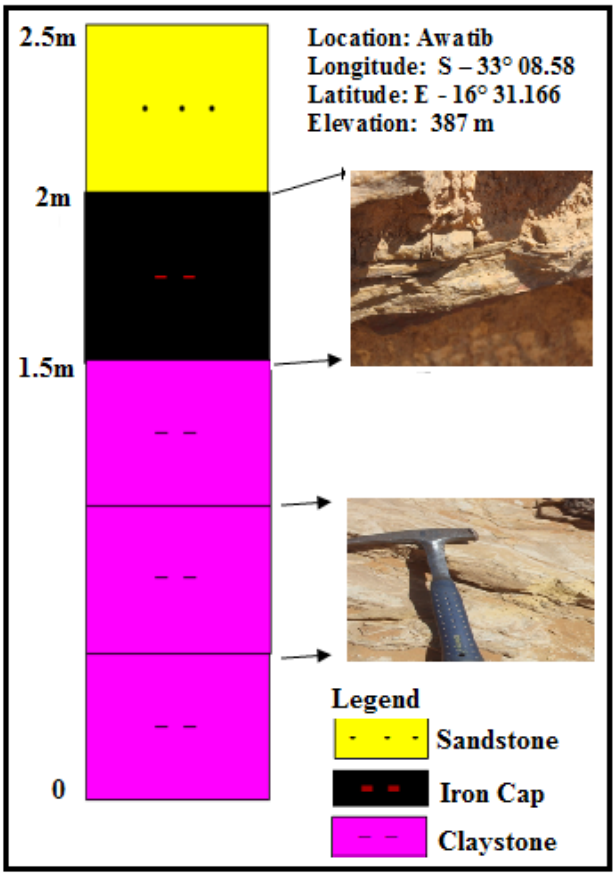

Figure 3. Vertical sedimentary profile showing iron ore capping clay stone in the sequence of Awatib area

5.1 The Iron Ores

Deposits of the ferruginous sediments are very abundant within and on top of the cretaceous and tertiary sediments of the Shendi-Atbara Basin. Three genetic groups can be distinguished in this study they are:

•Thin bands of ferruginous sediments (ferribands).

•Ferricrete capping on hills.

•Beds of fluviatile oolitic ironstones.

Two phases of ferricrete formation can tentatively be distinguished. Ferricrete sandstone on an early tertiary erosion surface is abundant around Shendi and Atbara. Oolitic ironstone within fluviatile sediments of the mid cretaceous Shendi formation has been discovered in locally widespread distribution. Stemming from the close sim-

 DOI: https://doi.org/10.30564/jgr.v3i1.2814

ilarities of continental and marine iron oolites, a common origin in made probable. As iron ooliths have been detected also being formal in-situ within ferricrete it appears to be possible to interpret marine and alluvial oolitic ironstone as being derived from ooliths formed in ferricrete, thus representing (a lateritic derived facies).

5.1.2. The Ferribands

Thin bands of less than 50cm in thickness occur within the sedimentary strata (Figure4). They are very common at the contact of different lithology especially when there is an abrupt change in grain sizes on both sides of permeability boundary (Plate 7 B). The fine grained as well as the coarse grained sediments are ferruginized by secondary impregnation of iron oxides and o hydroxides. Iron enrichment also occurs along bedding plane. Iron impregnated clay and siltstones are oftenly finally laminated (Plates 1, 2, 3). Mineralogical associations and textures characterized by banding resulting from the interlayering of oxides and silica , both on a coarse and a fine scale; the units may be lenses rather than layers, giving a "wavy“ appearance to the stratification (Plates 1, 2, 3).

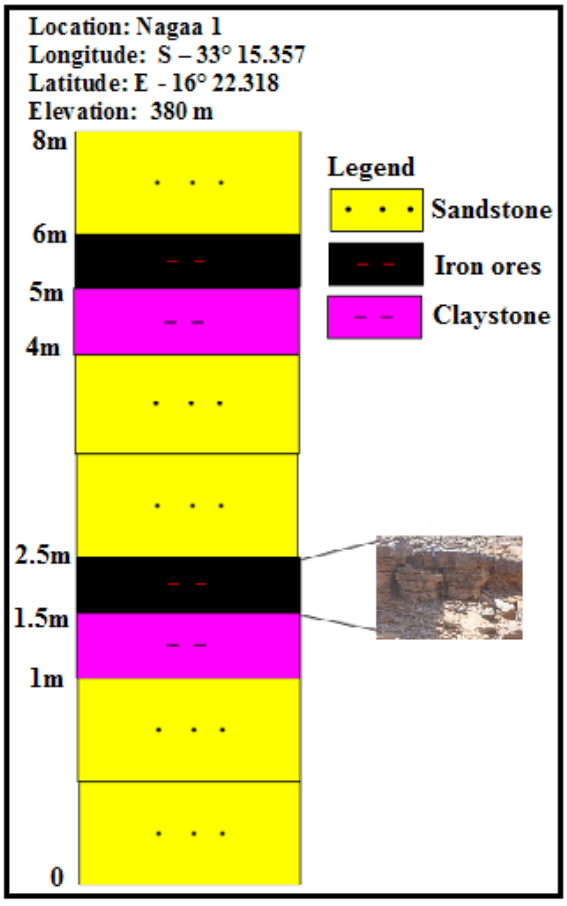

Figure 4. Vertical sedimentary profile showing two beds of iron ore in the sequence Alnagaa1 area

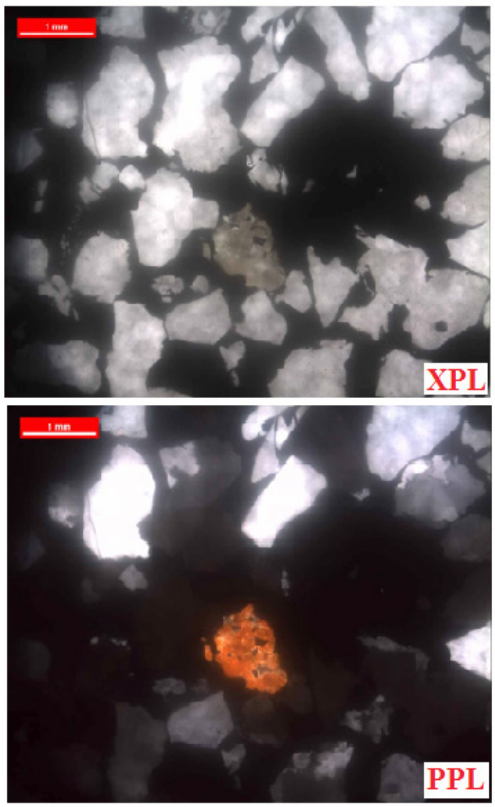

Plate 1. Photomicrograph showing the Iron oxide cement medium to coarse sub round quartz grain, Rock fragment - Alnagaa1 area

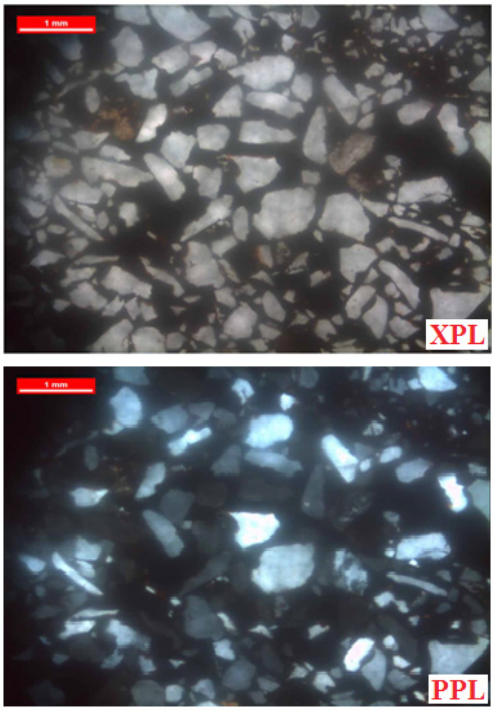

Plate 2. Photomicrograph showing light color (brownish), granular texture, angular to sub angular grains (mainly quartz); iron ore matrix fine grain - Alkarbican area

DOI: https://doi.org/10.30564/jgr.v3i1.2814

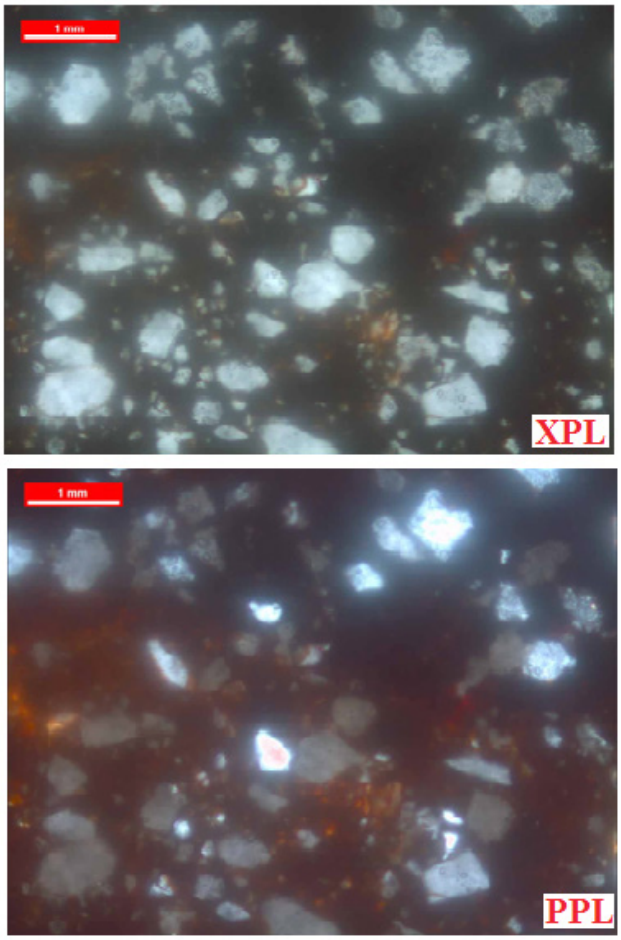

Plate 3. Photomicrograph showing the light color (brownish), granular texture, showing manganese (black) and iron (red) cements surrounding quartz - Musawarat 3 area.

5.1.2. Ferricretes

They may attain a thickness of several meters and occur mainly on flat top or mesas (Figure 5). They are massive to vesicular pisolitic, nodular or vermiform in characters (Plate 4, 5, 6). Rocks consisting of nearly pure iron oxides and oxihydroxides occur as well as kaolinitic or quartz rich ironstones forming granular textures (Plate 7 A, B, C, D). Ferricrete are considered to be the residual products of lateritic weathering processes and thus form the top horizon of a deep weathering profile. In Goz Alhaj area microscopically the slab composed mainly of iron oxides cemented by silicates minerals and carbonates (Plate 10 B). The iron oxides mainly hematite, goethite and limonite appear as oolitic to pisolitic and sometimes peletal grains that partially replaced by interlayered limonite and hematite some of oolith and peletal have formed around sand grains. Minor pyrite is also detected. The sample is sand facies iron ores (Plate 4, 5, 6).

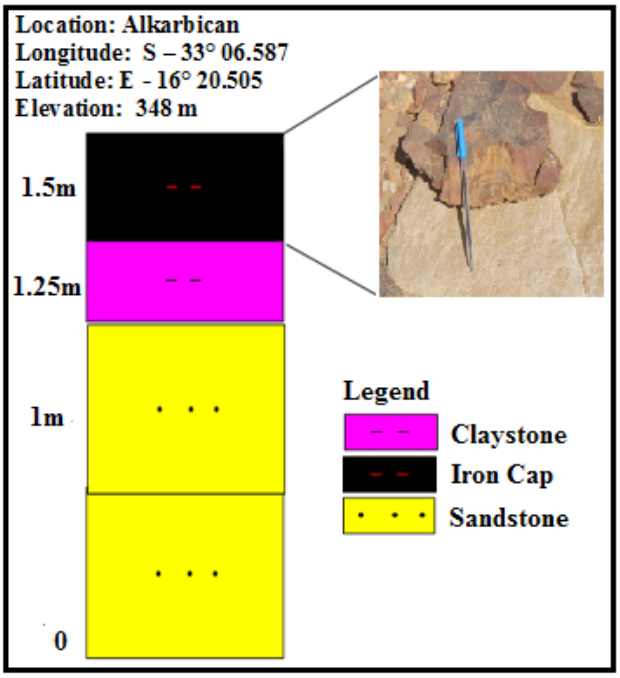

Figure 5. Vertical sedimentary profile showing iron cap in the sequence of Alkarbikan area.

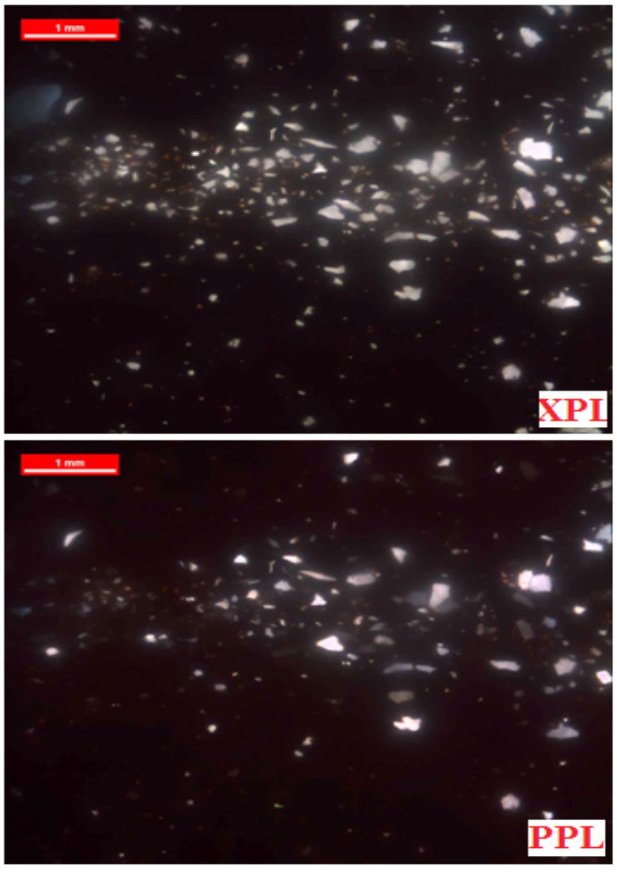

Plate 4. Photomicrograph showing interlayering of oxides and silica Typical banded iron formation assemblages and textures, Layered subhedral - Awatib area.

DOI: https://doi.org/10.30564/jgr.v3i1.2814

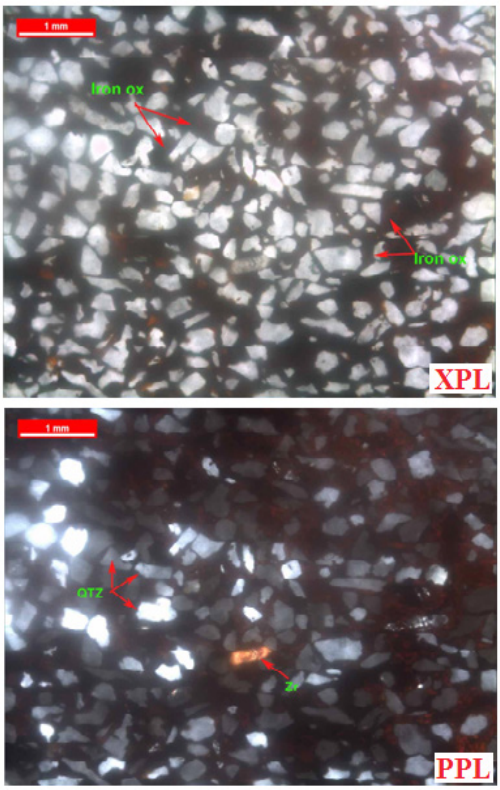

Plate 5. Photomicrograph showing light color (brownish), granular texture, angular to sub angular grains (mainly quartz); iron ore matrix fine grain - Awatib area.

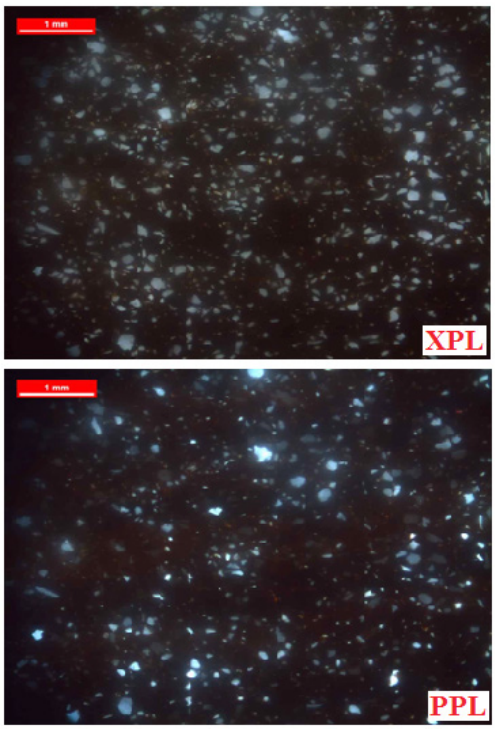

Plate 6. Photomicrograph showing light color (brownish), shows the typical rounded to subrounded quartz grains - Bigrawiah area.

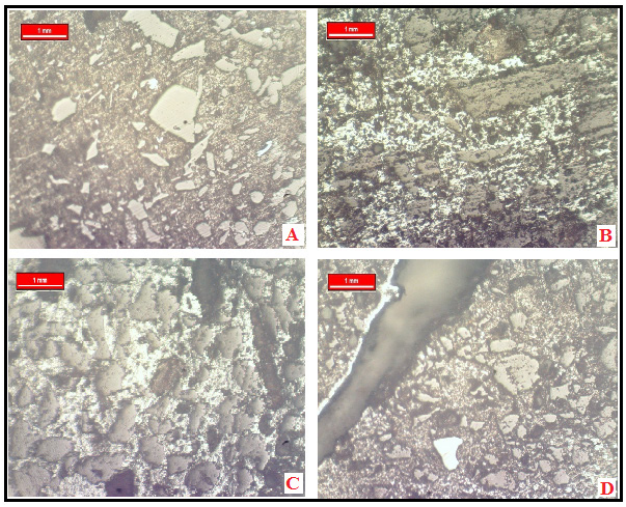

Plate 7. Showing: (A) Photomicrograph of the Magnetite is detected as euhedral crystals cubic to tabular - Alkarbican area. (B) Photomicrograph of the layering of iron oxides and silicates in banded iron formation - Awatib area. (C) Photomicrograph of the Iron oxide cementing the silicates minerals - Bigrawiah area. (D) Photomicrograph of the Iron oxide magnetite detected as a vein together with silicates - Bigrawiah area.

5.1.3 Oolitic Ironstone

Oolitic ironstones are found in many localities within the area extending between Shendi, kabushia and Eldamer, The ironstone beds attain a maximum thickness of approximately one meter (Fig 6). They occur within alluvial sediments on Shendi Formation. They occupy the top of bioturbated fine grained sediments. The iron oolities are mostly moderately to well sorting. The in- situ fragmentation of ooliths along desiccation cracks can be traced from complete ooliths to single fragments. Plastically deformed ooliths and spatolihs are missing in oolitic ironstones of fluvial environments. In some cases oolite outcrops occur on the Shendi Togni erosion surface. These oolites might be related to ferricrete formation of Tertiary age. In contrast to the intra sedimentary Cretaceous oolitic ironstones they abundantly consist of aggregates of ooliths which are surrounded by secondary cortex of goethite. Such pisolith like structure occurs within a reworking horizon above oolites. In Umm Ali area, oolitic ironstones were found at the upper most strata of the succession (Plate 8). This directly relates to the Phanerozoic ironstones because many such types of ironstone are oolitic and ooids can be composed of hematite (red), berthierine-chamosite (green), goethite (brown) and, rarely, magnetite (black) (Plate 9). Phanerozoic ironstones are mostly thin successions of limited areal extent, interdigitating with normal-marine sediments. They commonly weather to a rusty yellow or brown color at outcrop. Some ironstone feels heavy relative to other sedi-

DOI: https://doi.org/10.30564/jgr.v3i1.2814

ments. The texture is similar to oolitic ironstones. Most of the biogenic structural forms are rounded, tabular or concretions as most forms of oolites. They all follow the same systematic sequence of burial depth and organic matter existence at the oxidation zone (Plate 10 A, B). In Um Ali area the ore composed mainly of oolitic and peletal iron oxides cemented by silicates and carbonates (Plate 8). The oolith contained chamosite, hematite, and lemoite together with goethite. Minor magnetite, pyrite are also detected. Iron minerals occur dominantly as concentric quartz grain coatings and intestinal filling (Plate 10 C, D).

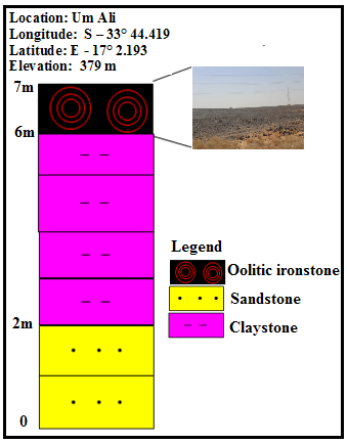

Figure 6. Vertical sedimentary profile showingoolitic ironstone in top sequence of Um Ali area.

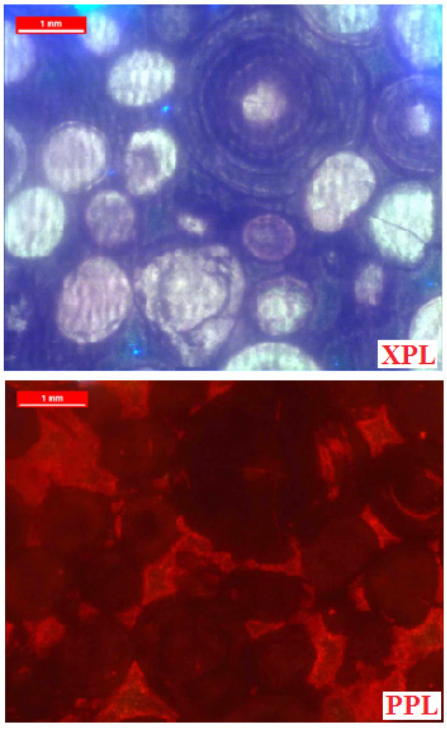

Plate 8. Photomicrograph showing the zonation of the iron (oolites), Textures observed in typical oolitic ironstones-Um Ali area.

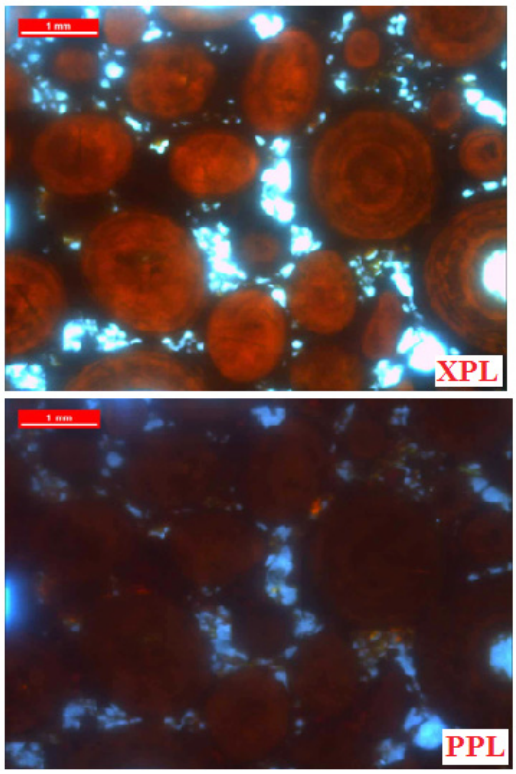

Plate 9. Photomicrograph showing the zonation of the iron, Textures observed in typical oolitic ironstones. Distorted ooliths comprised of fine-grained chamosite, Hematite and goethite - Goz Alhaj area.

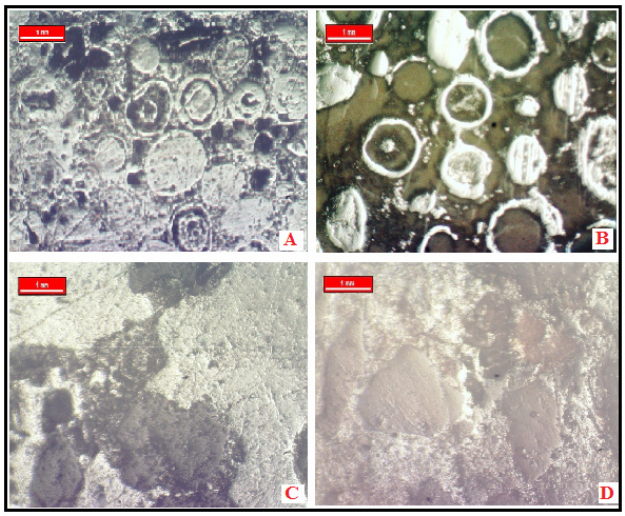

Plate 10. Showing: (A) Photomicrograph of the Oolitic and peletal iron oxides cemented by silicates and carbonates -Um Ali area. (B) Photomicrograph of the slab composed mainly of iron oxides cemented by silicates mineral and carbonates - Goz Alhaj area. (C) Photomicrograph of the very clear tabular euhedral iron oxide surrounding by manganese and silicates minerals - Nagaa 1 area. (D) Photomicrograph of the iron oxides is mainly magnetite and hematite together with goethite - Nagaa 2area.

 DOI: https://doi.org/10.30564/jgr.v3i1.2814

6. Conclusions

The present work has been carried out according to a plan including office work, field work, laboratory work. Eleven representive samples were taken during field work from the surface strata of the Shendi -Atbara Basin has been analyzed. Occurrence of iron ore was described at the outcrops and representative rock samples were collected from the 12 localities covering an area under study. Samples have been studied under the polarized microscope to determine the mineralogical composition, textural and microstructural characteristics. Similarly, polished sections from iron ore deposit were made and examined using ore microscope. Sedimentary iron ore can broadly be considered as occurring in three major classes: Ferribands iron, ferricrete iron and oolitic iron ores. Vertical sedimentary profiles revealed that the iron ores in the study area are different types in stratigraphic sequence such as cap, bedded and interbeded. Petrographic study of iron ore in collected indicates that the main types of textures and structures in studied samples are oolitic, granular, lamellar and banded. According to field observation, Vertical sedimentary profiles and petrographic study the origin of iron ore was formed by chemical precipitation during chemical weathering of surrounding areas in continental lacustrine environment.

Acknowledgement

Authors were indebted to GRAS (Geological Research Authority of Sudan) laboratory staff for their assistance with the preparation of the thin section and polished section analysis; and also thanks to the CPL (Central Petroleum Laboratories) staff for providing most of analysis and also thanks to the International University of Africa (IUA) for direct support during field work in the study area and for generous support which helped to improve the manuscript.

References

[1] Abubaker, A. M. A. Abasher (2020), Sedimentary iron Ore Deposits and Associated Manganese in Shendi-Atbara Basin, River Nile State, Sudan M. Sc. thesis, International University of Africa., Sudan.

[2] Whiteman, A. J. (1971), The geology of the Sudan Republic. London Clarendon Press: Oxford, 290 pp.

[3] Vail, J. R. (1983), Pan-African crustal accretion in north-east Africa. - J. Afi-. Earth Sci., 1 (3-4), 285-294, Oxford.

[4] Delany, F.M. (1955), Ring structures in the northern Sudan. Eclogae Geologicae Helvetiae, 48, 133-148.

[5] Vail, J.R., (1990), Geochronology of the Sudan. Overseas Geol. Miner. Resources 66, 58.Vermeersch, P.M., 2001. 'Out of Africa' from an Egyptian point of view. Quaternary Int. 75, 1030- 1112.

[6] Kheiralla, M. K. (1966), A study of the Nubian sandstone formation of the Nile Valley between 12°N and 17°42'N with reference to the groundwater geology. M.Sc. Thesis. Khartoum, Sudan: University of Khartoum. [7] Cox, L.R, (1932), On fossiliferous siliceous boulders from the Anglo-Egyption Sudan abstract. Proc. Geol. Soc. Lond., No.1254, pp.17-18.

[8] Andrew, G. And karkains, G. Y. (1945), stratigraphical notes, Anglo-Egyptian sudan. Sudan notes REC.26-157-66.

[9] Anderw, G (1948), The geology of the sudan.PP84-128 in agriculture in the Sudan. Tothill, J.D. (Editor). (London: Oxford University).

[10] Vail, J. R. (1971), Geological reconnaissance in part of Berber District, Northern Province, Sudan. - Bull. Geol. Survey Sudan, 18, 76 pp., Khartoum.

[11] Almond, D.C, (1969), Structure and metamorphism of the basement complex of NE Uganda. Overseas Geol. Miner. Resources 10, 146-163.

[12] Almond, D.C. (1977), The sabaloka igneous complex, sudan. Trnasaction of royal society in London. B., 287. No. 1348, P.595-633.

[13] Vail, J.R., (1978), Outline of the geology and mineral deposits of the Democratic Republic of the Sudan and adjacent areas. Overseas Geol. Miner. Resources 49, 67.

[14] Abdirasak A.H. (2019), Application of resistivity and remote sensing techniques for the groundwater investigation in the sabaloka complex – river Nile state, Sudan, M. Sc thesis, pp 12.

DOI: https://doi.org/10.30564/jgr.v3i1.2814

BILINGUAL PUBLISHING CO.
Pioneer of Global Academics Since 1984

Journal of Geological Research
https://ojs.bilpublishing.com/index.php/jgr-a

ARTICLE

Characterization of the Sulfide Deposits in the Southeastern Nigeria Using VLF Method: Insights from Numerical Modeling and Field Examples

D. E. Falebita[1] O. Afolabi[1] B. O Soyinka[2] A. A. Adepelumi[1*]

1.Department of Geology, Obafemi Awolowo University, Ile-Ife, Nigeria
2.Terracon, Seattle, Washington DC, USA.

ARTICLE INFO

Article history
Received: 15 January 2021
Accepted: 24 February 2021
Published Online: 31 March 2021

Keywords:
Sulfide
Conductor
VLF
Overburden thickness
Polarization parameters
Nigeria

ABSTRACT

A priori geologic and geophysical information has been used to construct conceptual VLF experiments on conductively and inductively coupled overburden geological models of the lead-zinc (Pb-Zn) mineralization zone found in southeastern Nigeria. This is based on the finite element approach to (1) simulate different geologic situations of overburden occurrence, (2) examine the roles played by overburden in modifying and masking VLF responses of a buried conductor target, and (3) confirm the effectiveness of VLF method in mapping lead-zinc lodes found in sedimentary terrains. The computed theoretical model curves and field examples are expected to serve as guide for VLF anomaly pattern recognition due to overburden thickness, resistivity and width of conductor in similar terrain as the study area.

1. Introduction

Mining of the sulfide minerals in Abakaliki area of southeastern Nigeria started in the early nineteenth century culminating a total of 9000 tons of lead ore and 1000 tons of zinc ore mined during the peak periods between 1946 and 1974. Various geophysical and geochemical methods have been used in prospecting for economic sulfide lodes in the area. However, very low frequency (VLF) geophysical method was only recently used [1, 2]. The VLF method is a classic electromagnetic method that has been used worldwide for decades as a geophysical prospecting tool [3, 4, 5, 6, 7, 8, 9, 10, 11, 12, 13]. Electrically conductive mineralized zones are generally more conductive than the host rocks in which they are emplaced, so ore targets can be delineated with ease using the VLF method [3, 5, 14]. The method is attractive to mineral explorationists because of its cost-effectiveness, speed of operation and portability of the equipment [15, 16, 1, 17, 18].

One of the up-hill tasks usually encountered while interpreting acquired VLF data is differentiating between anomalies caused by the ore bodies and conductively coupled overburden EM anomalies that are usually regarded as geological noise. On the other hand, EM signatures of promising anomalous zones are often masked by inductively coupled overburden leading to quantify such zones

**Corresponding Author:*
A. A. Adepelumi,
Department of Geology, Obafemi Awolowo University, Ile-Ife, Nigeria;
Email: adepelumi@gmail.com

 DOI: https://doi.org/10.30564/jgr.v3i1.2809

as non-promising and/or non-economic. For example, [1] reported lack of continuity of VLF response along some of their profiles despite the fact that the area is known to be highly mineralized. So, we deem it necessary to conduct numerical VLF model studies in order to investigate the roles played by overburden in masking and/or modifying the VLF response of a buried mineralized target and the effect of ore size to VLF signatures. Although several authors in the past have studied the effect of a uniform overburden on EM responses of a basement conductor [19, 20, 21, 22], no one has investigated VLF responses of conductors found in sedimentary terrain having similar geology to our research site in Nigeria. We hope that the geometry of the synthetic models will simulate the exploration target and serve as a guide in identifying such anomalous bodies in field situations specific to the study area in the southeastern Nigeria.

2. Geological Settings

The Abakaliki sulfide mineralization is found within the Cretaceous shales of the Asu River Group in the lower part of the Benue trough of Nigeria [23]. The Asu River Group represents the earliest sediments (shale and sandy-shale) that were deposited unconformably on the subsiding basement topographical depressions during the first marine transgressions into the trough [23, 24]. The emplacement of the mineralization is thought to be tectonically controlled [25]. The primary minerals constituting the lode are galena and sphalerite while the secondary minerals include pyrite, siderite, marcasite, limonite and quartz [1]. Formation temperature of the mineralization has been estimated to be about 140 ^{o}C while its origin is hydrothermal. Source of the lead mineralization is the detrital alkali feldspars which were eroded from the Precambrian basement and re-concentrated [26]. The age of the mineralization is generally agreed to take place at the end of the Santonian [27, 28, 29, 23]. According to [23], the formation of the mineralization took place in three distinct stages: (1) pre-ore fracturing and brecciation of Albian shales accompanied by the precipitation of framboidal and colloform aggregates of pyrite, siderite and quartz; (2) ore stage formation of sphalerite, galena, copper bearing minerals; and (3) final deposition of octahedral galena, sphalerite, bravoite and marcasite in the hanging wall of the veins.

3. The VLF-EM Overview

The VLF-EM principle is based on receiving and interpreting transmitted long distance electromagnetic signals from mainly military and navigation radio transmitters around the world. The frequency ranges can be very low, 3-30 kHz and low, 30-300 kHz [30]. The remote transmitter radiates two-component primary EM field - a vertical electric field component and a horizontal magnetic field component each perpendicular to the direction of propagation. These fields induce electric currents in conductive bodies lying below earth's surface to produce secondary magnetic fields that can be detected at the surface through deviation of the normal radiated field by the VLF receiver [31]. One part of the secondary field oscillates in-phase (real component) and the other part oscillates out-of-phase (imaginary) with respect to the primary field [32, 33, 13]. The oscillation traces an elliptic polarization of the primary field whose penetration depth depends on the transmitter frequency and the electric resistivity of the ground governed by skin depth relation:

$$\delta = 503\left(\frac{\rho}{f}\right)^{1/2}, \tag{1}$$

where ρ is the electrical resistivity in Ωm, f is the frequency in Hz and δ is the skin depth in meters [34, 9].

4. Numerical Modelling of VLF Data

We evaluate, through numerical modeling experiments, the VLF responses due to moderate overburden layer of uniform thickness, moderate conductivity, and finite lateral extent which is in galvanic contact (Model 1), and non-galvanic contact (Model 2), with a vertical planar conductor (ore-body) lying below it. This is because electromagnetic conductors of interest may be overlain by a partially conducting overburden layer which maybe or not in galvanic contact [21] with the underlying mineralized lead-zinc ore-body. The modeling is carried out with the sole aim of obtaining better insight into characteristics of the VLF responses that will help in explaining the possible role played by overburden in masking VLF responses when the overburden is conductively, and inductively coupled to the underlying ore body target. The working assumption is that the VLF signal of frequency 16 kHz from the transmission station at Great Britain is detectable in the study area [1]. The first set of VLF responses of interest is (1) the tilt angle (θ), which is the inclination of the major axis of the polarization ellipse, and (2) ellipticity (e) known as the ratio of the minor to the major axis of the ellipse [35] using relations proposed by [36].

$$\tan 2\theta = \pm \frac{2\left(H_z/H_x\right)\cos\Delta\phi,}{1-\left(H_z/H_x\right)^2} \tag{2}$$

DOI: https://doi.org/10.30564/jgr.v3i1.2809

$$e = \frac{H_z H_x \sin \Delta\phi}{H_1^2}, \quad (3)$$

where H_z and H_x are the amplitudes, the phase difference $\Delta\varphi = \varphi_z - \varphi_x$, in which φ_z is the phase of H_z and φ_x is the phase of H_x and $H_1 = \left| H_z e^{i\Delta\varphi} \sin\theta + H_x \cos\theta \right|$ [37]. Interpretation is based on [38] that showed that the inflection point of the tilt-angle and ellipticity signature will centre right on top of the conductor and the separation of the peak-peak amplitude of the response is an indirect indicator of the depth of burial of the conductor. The second set of VLF responses is the apparent resistivity (ρ_a) and the corresponding phase angle (φ) [39] using the relations proposed by [40, 41]:

$$\rho_a = \frac{1}{\omega\mu}\left|\frac{E_y}{H_x}\right|^2, \quad (4)$$

$$\varphi = \arctan\left[\frac{\mathrm{Im}\left(E_y / H_x\right)}{\mathrm{Re}\left(E_y / H_x\right)}\right], \quad (5)$$

where ω the angular frequency of the VLF primary is field and μ is the magnetic permeability of the subsurface [37]. Low resistivity zones are interpreted as possible fracture zones. The third set is the computation of equivalent current density (equation 6) for the conductive and inductive overburden models by linear filtering [42] of the real component of the secondary field. The filtering was by using the program developed by KIGAM [43, 44] to show the distribution of current with depth and the effect of overburden variation on the detectability of the conductor. This process leads to enhancement of anomalous signature, provides indication of current concentrations and spatial distribution that approximately reflect the depth and location of subsurface conductor [42, 43, 45].

$$I_a(0) = \frac{2\pi\left(-0.102 \cdot H_{-3} + 0.059 \cdot H_{-2} - 0.561 \cdot H_{-1} + 0.561 \cdot H_1 - 0.059 \cdot H_2 + 0.102 \cdot H_3\right)}{z} \quad (6)$$

where I_a is the equivalent current at a specific position and depth z; H_{-3} through H_3 are the originally computed synthetic VLF data.

The models used in the study closely approximate the electric structure beneath the survey lines used by [1] where the ore-body is either 10 m or 20 m wide [27, 23] and has 30 m length (Figure 2). A resistivity value of 0.01 Ωm was assigned to the lead-zinc lode based on the conductivity of the lode obtained by [27, 23]. The ore is considered to have a dip angle of 90° [1, 29] and embedded in a half-space of resistivity 40 Ωm overlain by an overburden of changing resistivity values between 50 and 500 Ωm [26] . A 200 m long survey line was considered and all responses of the mineralized zone are computed at a fixed frequency of 16 kHz every 2 m using a 100-mesh in x-direction and 30-mesh in y-direction making a total of 3000 elements.

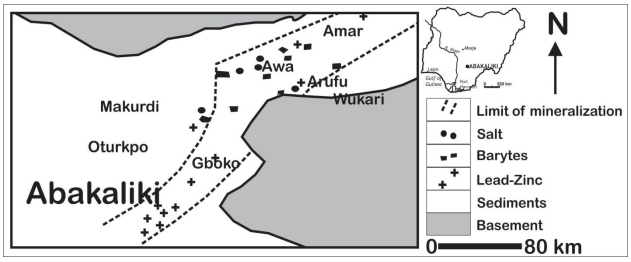

Figure 1. An illustrative description of the Lead-Zinc mineralization of the southeastern Nigeria (modified after Cratchley and Jones, 1965).

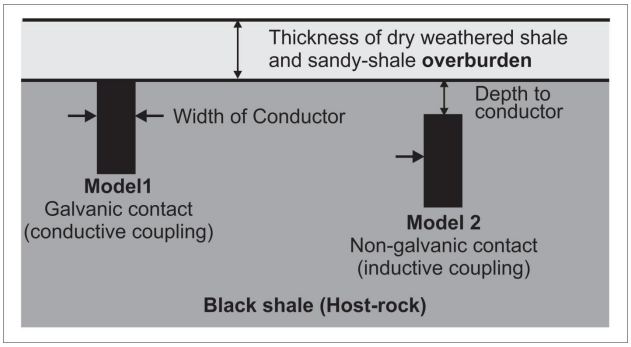

Figure 2. Description of the model configuration. A finitely conducting ore-body overlain by (1) conductively coupled and (2), inductively coupled uniform overburden layer.

4.1 Model 1 – Conductively Coupled

The ore-body with resistivity of 0.01 Ωm was allowed to have galvanic contact (*conductively coupled*) with the overburden of 10 m, 20 m and 30 m thickness and a host rock resistivity of 40 Ωm while the polarization parameters (apparent resistivity, phase, tilt and ellipticity) were computed for changes in overburden resistivity at 50, 100, 200 and 500 Ωm respectively.

4.2 Model 2 – Inductively Coupled

The ore-body was fixed at a depth of 4 m *inductively coupled* with overburden layer of 50 Ωm resistivity and changing thickness of 10 m, 20 m and 30 m. The resistivity values of the host rock and the ore body are the same as in model 1. These resistivity values correspond to those

 DOI: https://doi.org/10.30564/jgr.v3i1.2809

of the weathered shale and sandy-shale found in Abakaliki area. While keeping these parameters constant, the polarization parameters were computed for ore-body width of 10 m and 20 m respectively.

5. Results and Discussion

5.1 The VLF Synthetic Polarization Responses

Figure 3 and 4 show the various curves of the VLF synthetic polarization responses for models 1 and 2. For model 1 (Figs. 3a, b, c and d), the conductor is conductively coupled with overburden (galvanic contact), where the resistivity of the overburden varies as 50 Ωm, 100 Ωm, 200 Ωm and 500 Ωm respectively. For model 2 (Figs. 4a and 4b), the conductor is inductively coupled with the overburden (non-galvanic contact). All the polarization parameters, that is, apparent resistivity (expressed in Ωm), phase (expressed in degrees), tilt angle and ellipticity (expressed in percentages) have distinct and diagnostic characteristics of the buried conductor at different resistivity values and thicknesses of the overburden. Tables 1 and 2 summarize the polarization parameters for models 1 and 2 respectively.

5.1.1 Model 1 - Overburden Resistivity of 50 Ωm

Figure 3a shows the curves of the polarization parameters for overburden resistivity of 50 Ωm. At 10 m of overburden, the resistivity values across the buried conductor vary between 17.68 and 48.79 Ωm with an amplitude difference of about 31.12 Ωm. The lowest value is centered on the conductor and the highest values are representative of the host rock. The phase values vary between 46.94 and 77.96 degrees with amplitude of about 31.03 degrees. The peak of the curve is centered on the conductor. The tilt values vary between -8.49% and 8.54% with a difference of about 17.03%. The crossover point from the positive peak to negative peak is centered on the conductor. The ellipticity values vary between -0.18% and 0.18% with a difference of 0.36%. Similar to the tilt, the crossover point from the positive peak to negative peak is centered on the conductor. At 20 m of overburden, resistivity values vary between 49.16 and 54.33 Ωm with a reduced interval (about 5.16 Ωm) compared to 10 m overburden thickness. Similarly, the phase values vary between 46.31 and 61.48 degrees with a reduced interval of 15.17 degrees. The tilt varies between -1.59% and 1.59% with an interval of 3.17% while the ellipticity varies between -0.08% and 0.08% with an interval of 0.15%. At 30 m of overburden, the resistivity varies between 50.72 Ωm and 57.99 Ωm with an interval 7.27 Ωm. The resistivity distribution at this depth is different from those at 10 and 20 m overburden in that the peak of the curve is centered on the conductor indicating that the resistivity of the conductor is completely masked at greater depth. The phase varies between 45.31 and 50.22 degrees with a reduced interval of 4.92 degrees. The tilt varies between -1.31% and 1.32% with an interval of 2.63% and the ellipticity varies between -0.02% and 0.02% at an interval of 0.04%. The crossover points between the positive peaks and negative peaks are centered on the conductor. The tilt curve at this depth shows reverse shape compared to shallower depths. The reduction in the range (interval) of values of the polarization parameters at 20 m and 30 m is an indication of VLF attenuation/masking/screening at greater depths.

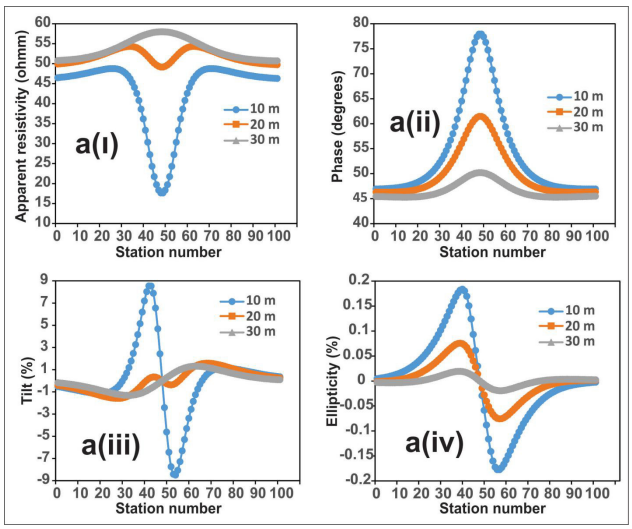

Figure 3a. Computed polarization parameters for a buried conductor model 1 for overburden resistivity of 50 ohm-m, and overburden thicknesses of 10, 20 and 30 m. The upper left panel show resistivity a(i), upper right panel show phase a(ii), lower left panel show the tilt angle a(iii) while the lower right panel show the ellipticity a(iv).

5.1.2 Model 1 - Overburden Resistivity of 100 Ωm

Figure 3b shows the polarization parameters for overburden resistivity of 100 Ωm. The resistivity across the buried conductor varies between 18.64 and 64.58 Ωm with amplitude of about 45.94 Ωm at 10 m. It varies between 65.41 and 88.18 Ωm with a difference of 22.79 Ωm at 20 m; and varies between 99.50 and 105.95 Ωm with a difference of 6.44 Ωm at 30 m. Clearly amplitude of the resistivity is decreasing with increasing depth. The phase varies between 52.60 and 81.60 degrees with a difference of 29.01 degrees at 10 m. It varies between 52.93 and 70.77 degrees with a difference of 17.83 degrees at 20 m and varies between 50.60 and 59.94 degrees with a difference of 9.34 degrees at 30 m. The peaks of the curves are

DOI: https://doi.org/10.30564/jgr.v3i1.2809

centered on the conductor. The tilt varies between -10.68 and 10.95% with a difference of 21.63% at 10 m. It varies between -2.38 and 2.35 with amplitude difference of 4.73% at 20 m and varies between -1.16 and 1.16% with amplitude difference of 2.33% at 30 m. The crossover points from the positive peak to negative peak are centered on the conductor. Apart from reduction in amplitude at greater depths, the tilt curve at 30 m is reversed possibly due to masking by the overburden. The ellipticity varies between -0.17 and 0.18% with amplitude difference of 0.36 at 10 m. It varies between -0.10 and 0.10 with a difference of 0.20 at 20 m and varies between -0.05 and 0.05 with difference of 0.09 at 30 m. Similar to the tilt, the crossover points between the positive and negative peaks are centered on the conductor.

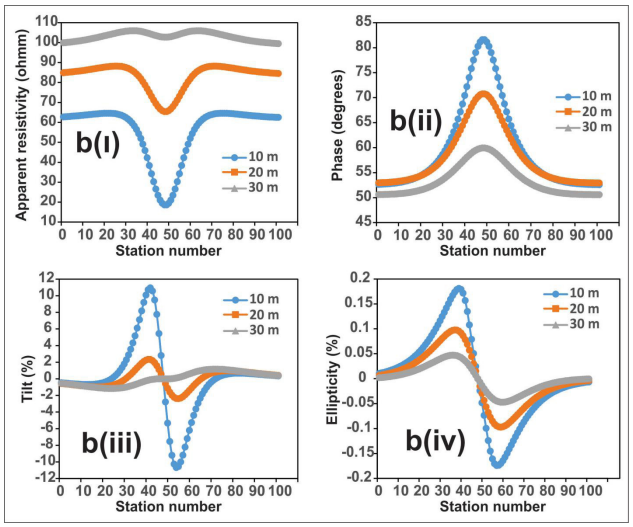

Figure 3b. Computed polarization parameters for a buried conductor model 1 for overburden resistivity of 100 ohm-m, and overburden thicknesses of 10, 20 and 30 m. The upper left panel show resistivity b(i), upper right panel show phase b(ii), lower left panel show the tilt angle b(iii) while the lower right panel show the ellipticity b(iv).

5.1.3 Model 1 - Overburden Resistivity of 200 Ωm

Figure 3c shows the polarization parameters for overburden resistivity of 200 Ωm. The resistivity across the buried conductor varies between 19.07 and 74.70 Ωm with a difference of about 55.63 Ωm at 10 m. It varies between 74.03 and 117.18 Ωm with a difference of 43.15 Ωm at 20 m; and varies between 139.84 and 160.93Ωm with a difference of 21.09 Ωm at 30 m. Again, the amplitude of the resistivity is decreasing with increasing depth. The phase varies between 56.39 and 83.56 degrees with a difference of 27.17 degrees at 10 m. It varies between 59.34 and 77.07 degrees with a difference of 17.74 degrees at 20 m and varies between 58.30 and 69.62 degrees with a difference of 11.32 degrees at 30 m. The peaks of the curves are centered on the conductor. The tilt varies between -11.79 and 12.12% with a difference of 23.90% at 10 m. It varies between -4.10 and 4.09% with amplitude difference of 8.189% at 20 m and varies between -1.09 and 1.07% with amplitude difference of 2.15% at 30 m. The crossover points from the positive peak to negative peak are centered on the conductor. There is no reversal of the tilt curve at 30 m compared to previous one. The ellipticity varies between -0.17 and 0.17% with amplitude difference of 0.34% at 10 m. It varies between -0.10 and 0.10% with a difference of 0.20% at 20 m and varies between -0.06 and 0.06% with a difference of 0.13 at 30 m. The crossover points between the positive and negative peaks are centered on the conductor.

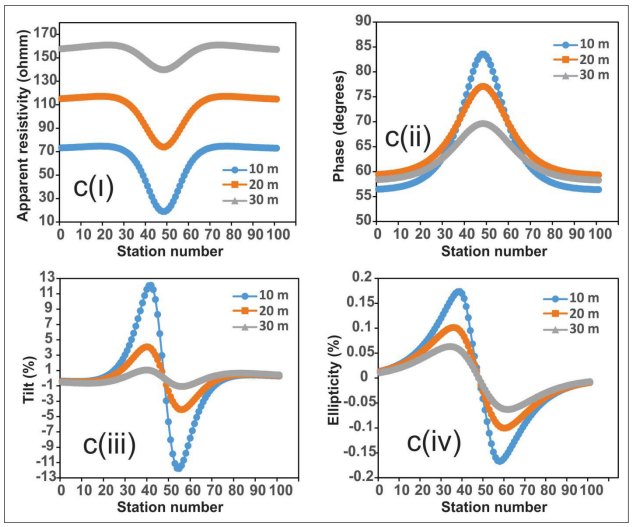

Figure 3c. Computed polarization parameters for a buried conductor model 1 for overburden resistivity of 200 ohm-m, and overburden thicknesses of 10, 20 and 30 m. The upper left panel show resistivity c(i), upper right panel show phase c(ii), lower left panel show the tilt angle c(iii) while the lower right panel show the ellipticity c(iv).

5.1.4 Model 1 - Overburden Resistivity of 500 Ωm

Figure 3d shows the polarization parameters for overburden resistivity of 500 Ωm. The resistivity across the buried conductor varies between 19.29 and 81.50 Ωm with a difference of about 62.21 Ωm at 10 m. It varies between 78.54 and 139.41 Ωm with a difference of 60.87 Ωm at 20 m; and varies between 163.31 and 211.47 Ωm with a difference of 48.16 Ωm at 30 m. The amplitude of the resistivity is decreasing with increasing depth. The phase varies between 59.04 and 84.78

DOI: https://doi.org/10.30564/jgr.v3i1.2809

degrees with a difference of 25.74 degrees at 10 m. It varies between 64.74 and 81.43 degrees with a difference of 16.69 degrees at 20 m and varies between 66.45 and 77.77 degrees with a difference of 11.32 degrees at 30 m. The peaks of the curves are centered on the conductor. The tilt varies between -12.45 and 12.83% with a difference of 25.28% at 10 m. It varies between -5.28 and 5.31% with amplitude difference of 10.59% at 20 m and varies between -2.38 and 2.38% with amplitude difference of 4.76% at 30 m. The crossover points from the positive peak to negative peak are centered on the conductor. There is no reversal of the tilt curve at 30 m compared to previous one. The ellipticity varies between -0.16 and 0.17% with amplitude difference of 0.33% at 10 m. It varies between -0.10 and 0.10% with a difference of 0.19% at 20 m and varies between -0.07 and 0.07% with a difference of 0.13 at 30 m. The crossover points between the positive and negative peaks are centered on the conductor.

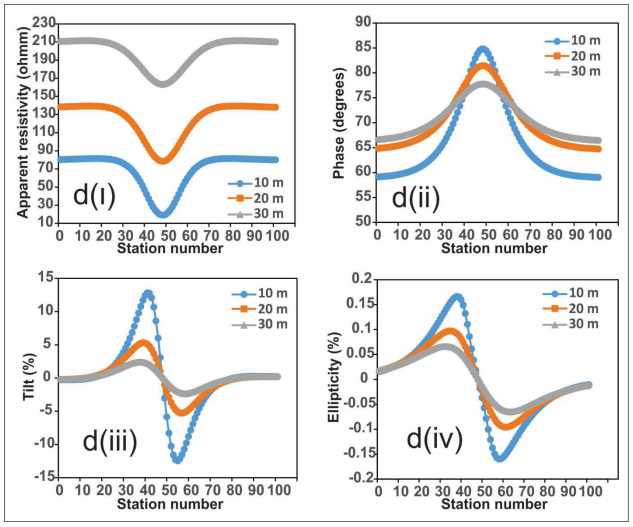

Figure 3d. Computed polarization parameters for a buried conductor model 1 for overburden resistivity of 500 ohm-m, and overburden thicknesses of 10, 20 and 30 m. The upper left panel show resistivity d(i), upper right panel show phase d(ii), lower left panel show the tilt angle d(iii) while the lower right panel show the ellipticity d(iv).

5.2 Model 2 - Overburden Resistivity of 50 Ωm

Figures 4a and 4b show the polarization curves for the inductively coupled model of overburden resistivity 50 Ωm with a conductor buried at 4 m below the overburden. Figure 4a is specifically for conductor width of 10 m while Figure 4b is for conductor width of 20 m. Similar anomaly patterns and shapes are observed over the buried ore-body as in conductive model at the same overburden resistivity of 50 Ωm (Fig. 3a) except for some differences. First, the amplitude of the resistivity is higher in the inductive model than the conductive model at the same overburden thickness. This is expected because for the conductive model, there is contact with the overburden but there is no contact with the overburden in the inductive model. The space of no contact is a low conductivity space for the inductive model which in turn increases resistivity. Second, the behaviour of the phase is the reverse of that of the resistivity in that the amplitude of the phase is higher in conductive model (Fig. 3b(i)) than the inductive model (Fig. 4b(i)) for the same overburden thickness. Third, the tilt amplitude in the inductive model is higher than that of the conductive model while the ellipticity values of the two models are about the same. When the width of the conductor is increased to 20 m, the same anomaly patterns of the polarization parameters are obtained with the fact that all the shapes of all the polarization parameters become broader, larger and pushed apart (Fig. 4b) compared to (Figs. 3a and 4a). These results clearly indicate that VLF signatures are influenced by the dimension of the ore-body such that large ore size will produce broad anomaly signature and vice-versa. Table 2 summarizes the polarization parameters for the inductively coupled model. The differences observed in the amplitudes of polarization parameters may be due to VLF screening by the overburden [46].

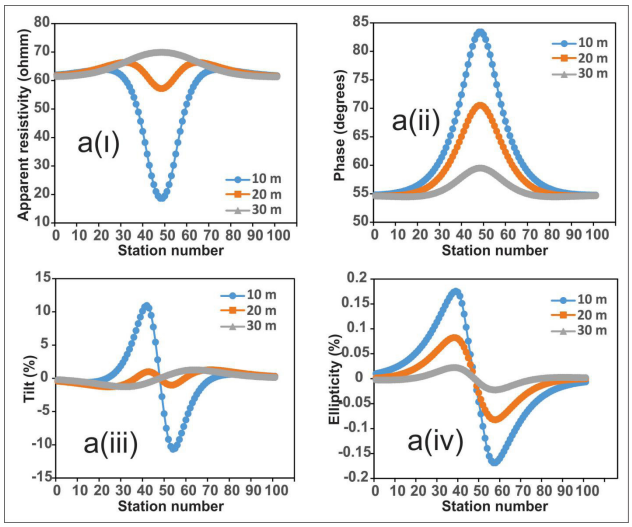

Figure 4a. Computed polarization parameters for a buried conductor model 2 for overburden resistivity of 50 ohm-m, and overburden thicknesses of 10, 20 and 30 m. The upper left panel show resistivity a(i), upper right panel show phase a(ii), lower left panel show the tilt angle a(iii) while the lower right panel show the ellipticity a(iv).

DOI: https://doi.org/10.30564/jgr.v3i1.2809

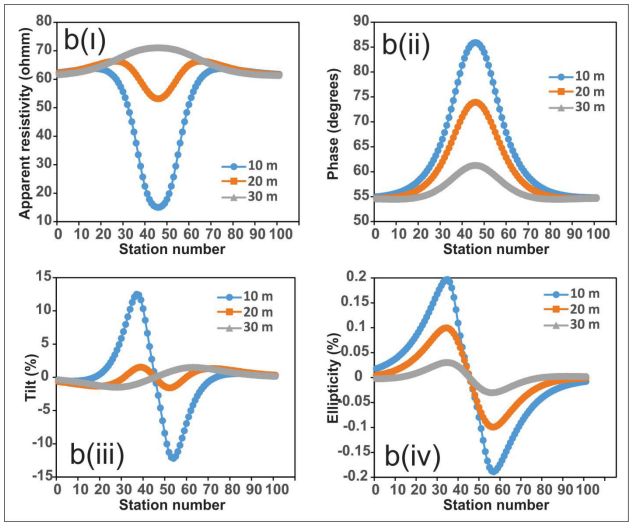

Figure 4b. Computed polarization parameters for a buried conductor model 2 for overburden resistivity of 50 ohm-m, and overburden thicknesses of 10, 20 and 30 m. The upper left panel show resistivity b(i), upper right panel show phase b(ii), lower left panel show the tilt angle b(iii) while the lower right panel show the ellipticity b(iv).

In general, the results indicate that the higher the resistivity of the overburden, the higher and more separated the amplitude of the resistivity (comparing Figs. 3a(i), 3b(i), 3c(i) and 3d(i)) but the lower the amplitude of the phase at various thicknesses of the overburden (comparing Figs. 3a(ii), 3b(ii), 3c(ii) and 3d(ii)). The values of the phase increasingly overlap at increasing resistivity values at increasing depth. The tilt increases with increasing resistivity of the overburden for all depths (comparing Figs. 3a(iii), 3b(iii), 3c(iii) and 3d(iii)) except at 30 m where there is slight decrease. There is a slight decrease in the ellipticity amplitude as the resistivity of overburden is increasing for all depths (comparing Figs. 3a(iv), 3b(iv), 3c(iv) and 3d(iv)). For all polarization parameters, the largest amplitude occurs at overburden thickness of 10 m where the signal is much more enhanced and diagnostic than at deeper depths. This is so because the conductor is closer to the surface. This general decrease in amplitude is possibly due to attenuation of the VLF field by the increasing overburden thickness thus leading to modification and masking of the VLF responses of the underlying conductor. These results show that both the thickness and resistivity of the overburden definitely affect the VLF responses that are obtained in such environment. Tables 1 and 2 summarize the polarization parameters for the conductively coupled model and inductively coupled model respectively.

A noticeable observation is the enhancement of the ellipticity more than tilt angle response which may be due to current channeling [46]. The galvanic contact between the buried ore-body and the overburden allows induced currents flow directly into the buried target. These currents are concentrated mainly in the out-of-phase components from the overburden, whereby the quadrature response exhibits greater enhancement than the in-phase response. Due to sharp attenuation in the surrounding medium and in the overburden, the tilt angle anomaly decays

Table 1. Polarization parameters for Model 1

	Resistivity (Ωm)			Phase (degree)			Tilt (%)			Ellipticity (%)		
Overburden (m)	10 m	20 m	30 m	10 m	20 m	30 m	10 m	20 m	30 m	10 m	20 m	30 m
	Overburden resistivity 50 Ωm											
Minimum	17.6838	49.1637	50.7172	46.9356	46.3086	45.3064	-8.49317	-1.58596	-1.31369	-0.1775	-0.0757	-0.0194
Maximum	48.7902	54.3286	57.9888	77.9628	61.4753	50.2227	8.54294	1.58629	1.31522	0.1839	0.0757	0.0193
Amplitude	31.1064	5.1649	7.2716	31.0272	15.1667	4.9163	17.03611	3.17225	2.62891	0.3615	0.1515	0.0387
	Overburden resistivity 100 Ωm											
Minimum	18.6439	65.41	99.5045	52.5995	52.9348	50.6028	-10.6806	-2.38224	-1.16452	-0.1741	-0.0972	-0.0472
Maximum	64.5836	88.1977	105.946	81.6048	70.7667	59.9395	10.9492	2.34536	1.16487	0.1811	0.0979	0.0472
Amplitude	45.9397	22.7877	6.4415	29.0053	17.8319	9.3367	21.6298	4.7276	2.32939	0.3552	0.1950	0.0944
	Overburden resistivity 200 Ωm											
Minimum	19.0672	74.0256	139.837	56.3922	59.3367	58.2969	-11.7781	-4.0973	-1.0789	-0.1671	-0.1004	-0.0630
Maximum	74.6968	117.179	160.931	83.5608	77.074	69.6217	12.1193	4.0917	1.0689	0.1735	0.1016	0.0632
Amplitude	55.6296	43.1534	21.094	27.1686	17.7373	11.3248	23.8974	8.189	2.1477	0.3406	0.2019	0.1262
	Overburden resistivity 500 Ωm											
Minimum	19.2858	78.5419	163.307	59.0416	64.7409	66.4451	-12.4533	-5.2844	-2.3802	-0.1597	-0.0958	-0.0654
Maximum	81.4968	139.413	211.469	84.7836	81.4337	77.7679	12.8311	5.3098	2.3766	0.1664	0.0972	0.0658
Amplitude	62.211	60.8711	48.162	25.742	16.6928	11.3228	25.2844	10.5942	4.7568	0.3261	0.1929	0.1312

 DOI: https://doi.org/10.30564/jgr.v3i1.2809

Table 2. Polarization parameters for Model 2

	Resistivity (Ωm)			Phase (degree)			Tilt (%)			Ellipticity (%)		
Overburden (m)	10 m	20 m	30 m	10 m	20 m	30 m	10 m	20 m	30 m	10 m	20 m	30 m
	Conductor width is 10 m; Overburden resistivity is 50 Ωm; Conductor is 4 m below the overburden											
Minimum	18.6776	57.1934	61.2898	54.7593	54.6243	54.4717	-10.668	-1.2755	-1.2682	-0.1688	-0.0823	-0.0224
Maximum	63.8797	66.3554	69.8971	83.3909	70.5144	59.5018	10.9484	1.2772	1.2698	0.1756	0.0825	0.0223
Amplitude	45.2021	9.162	8.6073	28.6316	15.8901	5.0301	21.6164	2.5527	2.5381	0.3443	0.1648	0.0448
	Conductor width is 20 m; Overburden resistivity is 50 Ωm; Conductor is 4 m below the overburden											
Minimum	15.0397	53.1639	61.3067	54.7801	54.6371	54.4688	-12.2005	-1.5754	-1.4892	-0.1741	-0.1888	-0.0992
Maximum	63.7606	66.3253	71.0254	85.9187	73.9432	61.2662	12.5054	1.5350	1.4905	0.1811	0.1966	0.0996
Amplitude	48.7209	13.1614	9.7187	31.1386	19.3061	6.7974	24.7059	3.1104	2.9797	0.3552	0.3855	0.1988

more rapidly compared to ellipticity as depth is increased. Moreover, at depth 30 m (representing large depths) for overburden resistivity of 100 Ωm and below (more conductive than 200 and 500 Ωm), the tilt angle changes sign (Figs. 3a(iii), 3b(iii), and 4a(iii)). [45] showed that phase shifts leading to a total reversal of the in-phase response are common with VLF data acquired in a weathered or conductive terrain. The symmetricity of the shapes of the polarization parameters indicates the existence of a vertically dipping structure. The central low resistivity, central high phase values and cross overs of both the tilt and ellipticity curves at station 50 reflect the position and top of the buried ore-body. The buried ore-body that has direct galvanic contact with the overlying overburden would have large anomaly signature due to current channeling than the ore-body having no galvanic contact due to current screening. It is therefore suggested that overburden resistivity information should be obtained using other geophysical methods before ruling out some VLF responses obtained in a mineralized zone such as in the study area as non-promising. This is necessary because of the strong influence of overburden resistivity on the anomaly curves. These results correlate with field results shown by [15, 3, 37].

5.3 Depth dependence nature of polarization parameters

Table 3 shows some specific numerical characteristics of the polarization parameters against depth. This is to throw more light on the relationship between the polarization parameters and the depth of burial (overburden thickness) to further explain the issue of attenuation of VLF fields. It can be seen that as the depth of burial of the conductor increases, the polarization parameters fall off more rapidly in model 2 (non-galvanic) than in model 1 (galvanic). This shows that the induced currents in the overburden are actually channeled to the buried conductor when there is a galvanic contact with the overburden hence the polarization parameters are more enhanced in model 1. It is not so when there is no galvanic contact between the two bodies therefore model 2 seems to have less amplitude. The ellipticity signature exhibits a distinct anomaly signature in this environment because it falls off less rapidly with depth than the tilt angle anomaly for both models. This suggests that ellipticity VLF signature should be used along with the conventional in-phase components when prospecting for conductive mineralization found in such environment as the study area. By doing this, mineral prospects could be better detected, evaluated and quantified. Lastly, it is seen that thick overburden suppresses VLF anomaly and hence affects the detectability of the conductor.

Table 3. Depth dependence of polarization parameters for conductively coupled model

Depth	Model 1		Model 2	
h (m)	Tilt (%)	Ellipticity (%)	**Tilt (%)**	**Ellipticity (%)**
6	19.79	24.47	14.87	20.23
10	12.83	16.64	10.95	17.56
20	5.31	9.72	1.28	8.25
30	2.38	6.58	1.27	2.23

5.4 Current density pseudo-sections

We have shown that overburden thickness and resistivity affect the amplitude of polarization parameter signatures thereby inhibiting the detectability of the buried conductor through masking and/or screening. Figures 5 and 6 show the computed real and imaginary equivalent current density (ECD) showing the conductivity distributions with depth in pseudo-section form for various depths (overburden thickness, z =10, 20 and 30 m). Over the conductor, the real part of the equivalent current distribution has only positive values for the two models while the imaginary part has both negative and positive values and the maxima of the current appear right on top of the conductor. For each mode l, the strength of the current density decreases with increase in depth from 0 to 60 m.

DOI: https://doi.org/10.30564/jgr.v3i1.2809

For model 1, there is higher variation in the range of ECD values at 10 m, 20 m and 30 m compared to model2 due to overburden effect. The overburden effect plays out in both the real and imaginary components of the ECD. For instance at 10 m, the real part ECD varies for model 1 (Figure 5a) and model 2 (Figure 6a) between 0 and 4.7%; but at greater depth due to overburden effect, the range in variation is higher in model1 (Figs. 5b and c) compared to model2 (Figs. 6b and 6c). The concentration of the current density shows that currents are actually induced into the conductor and they only concentrate on top of the conductor. Similar current flow patterns are observed both for the conductive and inductive overburden models where the shape, location and depth of the top of the conductor are well resolved compared to the bottom of the conductor. This means that the closer the conductor is to the surface the more resolving it is for both the galvanic and the non-galvanic contacts. In all cases, the shape of the ECD is symmetrical which indicates the dip of the conductor is 90°. The observed extended dome-shaped pattern of the current density confirms the suggestion of [45] that such body tend to have such shape which would provide the interpreter with information on source discrimination. In addition, there is an observable concaving of the shape of the imaginary component of the ECD of the conductor at all depths of the overburden only in model2. This pattern may help in field situations to separate such inductively coupled conductors from the conductive ones. These results indicate that both the pseudo-sections of the filtered real and imaginary components of the ECD serve as effective complementary views to delineate conductively or inductively coupled buried ore-body [42, 45].

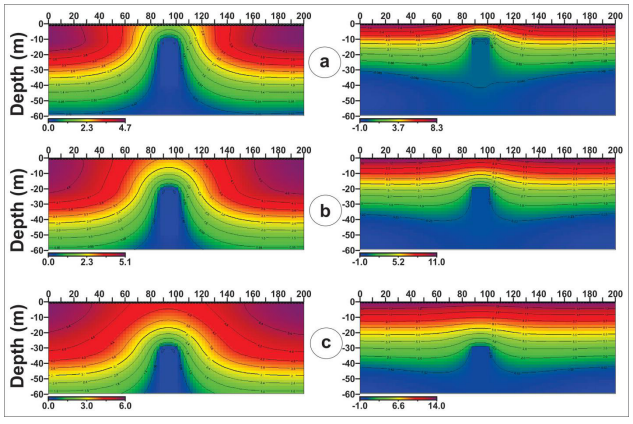

Figure 5. Equivalent current density (ECD) pseudo-section for the conductively coupled overburden model 1 (H-polarization mode). The left panel shows the real component while the left panel shows the imaginary component. The horizontal station spacing is in meters, while ECD is in percentage (%). Overburden thickness is 10 m, 20 m and 30 m in a, b and c respectively.

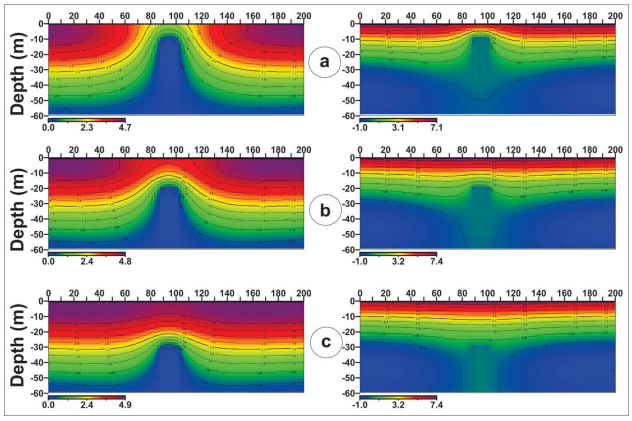

Figure 6. Equivalent current density (ECD) pseudo-section for the inductively coupled overburden synthetic model 2 (H-polarization mode). The left panel shows the real component while the left panel shows the imaginary component. The horizontal station spacing is in meters, while ECD is in percentage (%). Depth to the top of the conductor is 10 m, 20 m and 30 m in a, b and c respectively.

6. Conclusions

On the basis of the numerical VLF modeling studies, the synthetic VLF characteristics of lead-zinc lode found in southeastern Nigeria were computed. The computed model responses are expected to provide mineral explorers with some typical sections to aid in quick identification of the anomaly caused by such deposits found in sedimentary terrain as the study area. The zero crossover point of the tilt angles and ellipticity were shown to indicate the position of the ore-body as the inflection of their signs from positive to negative occurs right on top of the conductor. The minimum of the computed resistivity and maximum of the phase appear directly over the ore body. From this study, we found out that the thickness and resistivity of the overburden medium overlying the mineralized zone coupled with the resistivity of the host rock greatly influence the VLF responses obtained. Combination of these factors was shown to suppress and/or mask the signature of the buried ore target, and hence affect the detectability of the conductor in such terrain. The computed equivalent current distributions for various depths using the Karous-Hjelt linear filtering technique provide good insight about the location, depth extent, dip, size and geometry of the conductor. The numerical modeling studies suggest that VLF-EM can be effectively used to explore lead-zinc mineralization in an environment having similar geology as the study area after due consideration to the aforementioned experimental scenarios.

DOI: https://doi.org/10.30564/jgr.v3i1.2809

References

[1] Eze, C. L., Mamah, L. I., and Israel-Cookey, C., 2004. Very low frequency electromagnetic (VLF-EM) response from a lead sulphide lode in the Abakaliki lead/zinc field, Nigeria. Interational Journal of Applied Earth Observation and Geoinformation, 5, 159-163.

[2] Victor, O. M., Onwuemesi, A. G., and Aniwetalu, E. U. 2015. Exploration of Lead-Zinc (Pb-Zn) mineralization using very low frequency electromanetic (VLF-EM) in Ishiagu, Ebonyi State. Journal of Geol. Geosci. 4: 214. DOI:10.4172/2329-6755.1000214

[3] Phillips, W. J., and Richards, W. E., 1975. A study of effectiveness of the VLF method for the location of narrow-mineralised fault zones: Geoexploration, 13, 215-226.

[4] Warnana, D. D., and Bahri, A. S., 2004. On the use of resistivity and VLF method for profiling underground cave in Ngeposari, Semanu Gunung Kidul. In: Proceedings of the 1st International Seminar of Early Warning System. LPPM-ITS, Surabaya, pp. 33-43.

[5] Monteiro-Santos, F. A., Mateus, A., Figueiras, J., and Gonçalves, M. A. 2006. Mapping groundwater contamination around a landfill facility using the VLF-EM method – a case study. Journal of Applied Geophysics, 60, 115-125.

[6] Kaya, M.A., Özürlan, G., and Şengül, E., 2007. Delineation of soil and groundwater contamination using geophysical methods at a waste disposal site in Çanakkale, Turkey. Environmental Monitoring Assessment, 135, 441-446.

[7] Al-Tarazi, E., Abu Rajab, J., Al-Naqa, A., and El-Waheidi, M., 2008. Detecting leachate plumes and ground water pollution at Ruseifa municipal landfill utilizing the VLF-EM method. Journal of Applied Geophysics, 65, 121-131.

[8] Bahri, A.S., Santoso, D., Kadir, W.G.A., Puradimedja, D. D., Tofan, R. M., and Monteiro-Santos, F. A., 2008. Penerapan metoda Very Low Frequency-vertical Gradient (VLF-EM-vGRAD) untuk memetakan Sungai bawah permukaan di daerah karst. In: Proceedings of the 33rd Pertemuan Ilmiah Tahunan Himpunan Ahli Geofisika Indonesia (PITHAGI), pp. 10 - 20.

[9] Gürer, A., Bayrak, M., and Gürer, Ö. F., 2009. A VLF survey using current gathering phenomena for tracing buried faults of Fethiye–Burdur fault zone, Turkey. Journal of Applied Geophysics, 68, 437-447.

[10] Neumann, T., Berner, Z., Stüben, D., Bahri, A. S., and Jaya, M., 2009. Geowissenschaftliche Bewertung von Karsthöhlen für die asserbewirtschaftung in Gunung Sewu. Wasser Wirtsch. 7-8, 31-36.

[11] Sharma, S. P., Anbarasu, K., Gupta, S., and Sengupta, A., 2010. Integrated very low- frequency EM, electrical resistivity, and geological studies on the Lanta Khola landslide, North Sikkim, India. Landslides, 7, pp. 43-53.

[12] Abbas, A.M., Khalil, M.A., Massoud, U., Monterio-Santos, F., Mesbah, H. A., Lethy, A., Soliman, M., and Ragab, E. S. A., 2012. The implementation of multi-task geophysical survey to locate Cleopatra Tomb at Tap-Osiris Magna, Borg El-Arab, Alexandria, Egypt "Phase II". NRIAG Journal of Astronomy and Geophysics. 1, 1-11.

[13] Adelusi, A. O., Ayuk, M. A., and Kayode, J. S., 2014. VLF-EM and VES: an application to groundwater exploration in a Precambrian basement terrain SW Nigeria. Annals of Geophysics, 57, 1, 2014, S0184; DOI: 10.4401/ag-6291.

[14] Sungkono, A. S., Bahri, D. D. W., Fernando. A.M.S, and Bagus. J.S., 2014: Fast, simultaneous and robust VLF-EM data denoising and reconstruction via multivariate empirical mode decomposition. Computer and Geoscience, 67: 125-138.

[15] Paterson, N. R. and Ronka, V., 1971. Five years of surveying with the very low frequency electromagnetic method. Geoexploration, 9, 7-26.

[16] Saydam. A. S., 1981. Very low frequency electromagnetic interpretation using tilt angle and ellipticity measurements. Geophysics, 46, 1594-1605.

[17] Jeng, Y., Lin, M-J., Chen, C-S., and Wang, Y-H. 2007. Noise reduction and data recovery for a VLF-EM survey using a nonlinear decomposition method. Geophysics, vol. 72, No. 5, September-October, pp. F223-F235.

[18] Bayrak, M., and Şenel, L., 2012. Two-dimensional resistivity imaging in the Kestelek boron area by VLF and DC resistivity methods. Journal of Applied Geophysics, 82, pp. 1-10.

[19] Lowrie, W., and West. G. F., 1965. The effect of conducting overburden on electromagnetic prospecting measurements. Geophysics, 30, 624-632.

[20] Lajoie, J. J., and West. G. F., 1976. The electromagnetic response of a conductive inhomogeneity in a layered earth. Geophysics, 41, 1133-1156.

[21] Joshi, M. S., Gupta, O. P., Negi, J. G., 1984. Scale-model response of a thin vertical conductor below a conductive, inductive, or laterally inhomogeneous over-burden layer. Geophysics, 49, 2159-2165.

[22] Babu, V. R, Ram, S. and Sundararajan, N. 2007. Modeling and inversion of magnetic and VLF-EM data with an application to basement fractures: A case study from Raigarh, India. Geophysics, Vol. 72, No. 5;

DOI: https://doi.org/10.30564/jgr.v3i1.2809

p. B133–b140.10.1190/1.2759921.

[23] Akande, S. O., and Mucke, A., 1989. Mineralogical, textural and paragenetic studies of the Lead-Zinc-Copper mineralization in the lower Benue Trough (Nigeria) and their genetic implications. Journal of African Earth Science, 9, 23-29.

[24] Akande, S. O., and Mucke, A., 1993. Coexisting copper sulphides and sulphosalts in the Abakaliki Pb-Zn deposit, lower Benue Trough (Nigeria) and their genetic significance. Mineralogy and Petrology, Volume 47, Issue 2-4, pp 183-192.

[25] Benkhelil, J. 1987. Cretaceous deformation, magmatism and metamorphism in the lower Benue Trough, Nigeria. Geological Journal, 22, 467-493.

[26] Etim, O.N., Louis, P., and Maurin, J.C., 1988. Interpretation of electrical sounding on the Abakaliki lead–zinc and brine prospects, S.E. Nigeria: Geological and genetic implications. Journal of African Earth Science, 7 (5-6), 743-747.

[27] Orajaka, S., and Nwachukwu, S.O., 1968. Combined electromagnetic and geochemical investigations in Ameri lead-zinc area. Journal of Mining Geology, 3, 49-52.

[28] Olade, M. A and Morton, R. D. 1985. Origin of lead-zinc mineralization in the southern Benue trough, Nigeria. Fluid inclusions and trace element studies. Mineral Deposita, 20, 76-80.

[29] Mamah, L. I., and Eze, L.C., 1988. Electromagnetic and ground magnetic survey over zones of lead-zinc mineralization in Wanakom (Cross River State). Journal of African Earth Science, 7, 749-758.

[30] Coppo, N., Schnegg, P-A., Defago, M., and GSCB. 2006. Mapping a shallow large cave using a high-resolution very low frequency electromagnetic method. Proceedings of the 8th conference on limestone hydrogeology. Neuchatel Switzerland - Web edition, N. Goldscheider, J, Mudry, L. Savoy and F. Zwahlen (Eds), 268 pages.

[31] Sinha, A. K., 1990. Interpretation of ground VLF-EM data in terms of vertical conductor models. Geoexploration, 26, 213-231.

[32] Turberg P., and Müller I., 1992. La méthode inductive VLF-EM pour la prospection hydrogéologique gp" eqpvkpw" fw" oknkgw" Ýuuwtg0" Cppcngu" UekgpvkÝswgu" fg" nÓWpkxgtukvfi" fg Dgucp›qp, Mémoire Hors de Série, nº 11, Cinquième Colloque d´Hydrogéologie en Pays Calcaire et en Milieu Fissuré, Neuchâtel, Suisse, 207-214.

[33] Bosch. F. P., and Muller, I., 2001. Continuous gradient VLF measurements: a new possibility for high resolution mapping of karst structures. First Break, 19, 343-350.

[34] Beamish, D. 1998. "Three-dimensional modelling of VLF data", Journal of Applied Geophysics, vol. 39, pp. 63-76.

[35] Sharma. S. P., Biswas, A., and Baranwal. V. C. 2014. Very Low-Frequency Electromagnetic Method: A Shallow Subsurface Investigation Technique for Geophysical Applications. Recent Trends in Modelling of Environmental Contaminants. DOI: 10.1007/978-81-322-178-1_5. 119-32.

[36] Smith, B. D., and Ward, S. H., 1974. On the computation of polarization ellipse parameters. Geophysics, 39, 867-869.

[37] Adepelumi, A. A., Yi, M. J., Kim, J. H. and Ako, B. D. 2006. Integration of surface geophysical methods for fracture detection in crystalline bedrocks of southwestern Nigeria, Hydrogeology Journal, vol. 14, pp. 1284-1306.

[38] Saydam. A. S. 1981. Very low-frequency electromagnetic interpretation using tilt angle and ellipticity measurements. Geophysics, Vol. 46 (11), 1508-1618

[39] Kayode, J. S., A.O. Adelusi, M.N.M. Nawawi, M. Bawallah, T.S. and Olowolafe 2016. "Geo-electrical investigation of near surface conductive structures suitable for groundwater accumulation in a resistive crystalline basement environment: A case study of Isuada, southwestern Nigeria", Journal of African Earth Sciences, vol. 119, pp. 289-302.

[40] Cagniard, L., 1953. Basic theory of the magnetotelluric method of geophysical prospecting. Geophysics, 18 (3), 605-635.

[41] Kaikkonen, P, 1980. Interpretation nomograms for VLF measurements. Acta. Univ. Ouluensis, A. 92, Phys. 17: 1-48.

[42] Karous, M., and Hjelt, S. E., 1983. Linear filtering of VLF dip-angle measurements. Geophysical Prospecting, 31, 782-794.

[43] Chung, S. H., Lee, S. H and Kim, J. H., 1990. Depth presentation of VLF-EM data using digital filtering. Geophysical exploration method development series KR-89-2D-2 of Korea institute of energy and resources, 97-115.

[44]EM2Dmodel, 2002. EM2Dmodel™ version 1.0, Processing and interpretation software for electrical resistivity data. KIGAM, Daejeon, South Korea.

[45] Ogilvy, R. D., and Lee, A. C., 1991. Interpretation of VLF-EM in-phase data using current density pseudo-sections. Geophysical Prospecting, 39, 567-580.

[46] Poddar, M., 1982. Very low-frequency electromagnetic response of a perfectly conducting half-plane in a layered half-space. Geophysics, 47, 1059-1067.

 DOI: https://doi.org/10.30564/jgr.v3i1.2809

BILINGUAL
PUBLISHING CO.
Pioneer of Global Academics Since 1984

Tel:+65 65881289
E-mail:contact@bilpublishing.com
Website:www.bilpublishing.com